

Single Molecule Sensing

THÈSE N° 5155 (2011)

PRÉSENTÉE LE 7 OCTOBRE 2011

À LA FACULTÉ SCIENCES ET TECHNIQUES DE L'INGÉNIEUR
LABORATOIRE D'OPTIQUE BIOMÉDICALE
PROGRAMME DOCTORAL EN PHOTONIQUE

ÉCOLE POLYTECHNIQUE FÉDÉRALE DE LAUSANNE

POUR L'OBTENTION DU GRADE DE DOCTEUR ÈS SCIENCES

PAR

Claudio DELLAGIACOMA

acceptée sur proposition du jury:

Prof. C. Moser, président du jury
Prof. T. Lasser, directeur de thèse
Prof. J. Enderlein, rapporteur
Dr N. Garin, rapporteur
Dr T. Scharf, rapporteur



ÉCOLE POLYTECHNIQUE
FÉDÉRALE DE LAUSANNE

Suisse
2011

Cominciate col fare ciò che è necessario,
poi ciò che è possibile.
E all'improvviso vi sorprenderete a fare l'impossibile.
— San Francesco d'Assisi

*Start by doing what is necessary;
then do what is possible;
and suddenly you are doing the impossible.*

To Elisabeth, Marlies & Jürg

Abstract

Living organisms consist of cells, the elementary components of which are proteins providing cellular structures and functionality. Nowadays, proteins of the size of one to a few tens of nanometers can be efficiently monitored by fluorescence microscopy and/or spectroscopy reaching the necessary single molecule sensitivity. However, for a more complete understanding of biological processes, the combined investigation of both cellular structures and function at the single molecule level is essential.

This work extends the possibilities of existing single molecule investigation methods. The goal was to conceive a functional super-resolution imaging technique by joining the strong concepts from state-of-the-art microscopy and spectroscopy and was approached in three steps. As a first step, confocal fluorescence correlation spectroscopy (FCS) was applied in nanochannels to create sub-diffraction sampling volumes. The resulting enhanced sensitivity to the surface effects depending on ionic surface layers led to a modified protein diffusion measured with FCS. Triplet state lifetime and population analysis have confirmed the model developed for the protein diffusion as a function of the ionic concentration.

In the second step, stochastic optical reconstruction microscopy (STORM) was implemented and enhanced by merging with a recent labeling technique called SNAP-tag. As a result, the labeling technique for bright and switchable organic fluorescent dyes attached by a short linker of only ≈ 2.5 nm to the target molecule enabled a localization precision down to ≈ 10 nm. To meet the stringent photo-physical requirements imposed by STORM, toxic imaging buffers based on thiols have to be used. It was found that these requirements could be relaxed by super-resolution optical fluctuation imaging (SOFI) making a step forward to live-cell super-resolution investigations, which introduced the third step.

In the third step, SOFI was characterized providing the basis for combining functional and structural super-resolution imaging techniques. The comparison of STORM and SOFI revealed the strengths of each technique. Under ideal blinking conditions with ultra-stable long-lived dark states, STORM outperforms SOFI. However, if the emitters are not well isolated, SOFI achieves a higher effective resolution than STORM and even without mislocalization artifacts. This led onto a novel imaging technique derived from SOFI: Cumulant microscopy merges structural super-resolution with functional imaging. Simulations and measurements showed that photo-physical parameters can be extracted from the emitters serving as nano-sensors. In conclusion, concepts of FCS have been merged with an improved super-resolution technique leading to a novel functional super-resolution imaging technique, which is compatible with living cells.

Keywords: single molecule, functional imaging, fluorescence correlation spectroscopy (FCS), nanochannel, diffusion, triplet state, super-resolution microscopy, stochastic optical reconstruction microscopy (STORM), SNAP-tag, super-resolution optical fluctuation imaging (SOFI), cumulant microscopy

Kurzfassung

Lebewesen bestehen aus Zellen, deren Strukturen und Funktion durch Proteine bestimmt werden. Proteine der Grösse von einem bis hundert Nanometer können mit Mikroskopie und Spektroskopie, welche eine Einzelmolekülempfindlichkeit erreichen, effizient untersucht werden. Die Verbindung von sowohl strukturellen als auch funktionellen Zelluntersuchungen bis hin zu Einzelmolekülen ist wertvoll, um biologische Prozesse ganzheitlicher verstehen zu können.

Die vorliegende Arbeit erweitert so die Möglichkeiten von bestehenden Einzelmolekülanalyseverfahren. Das Ziel war, durch die Verbindung der Stärken modernster Mikroskopie- und Spektroskopiemethoden, ein funktionelles superauflösendes Abbildungsverfahren auszuarbeiten, und wurde in drei Schritten angegangen.

Im ersten Schritt wurde Fluoreszenz-Korrelations-Spektroskopie (FCS) in Nanokanälen angewandt, um Abtastvolumen zu erzeugen, die kleiner sind als beugungsbegrenzte Volumen. Die resultierende erhöhte Empfindlichkeit auf Oberflächeneffekte ermöglichte, die veränderte Proteindiffusion, welche von ionischen Oberflächenschichten abhängt, mit FCS zu messen. Analysen der Triplett-Lebensdauer und des Triplett-Anteils bestätigten das entwickelte Modell für die Proteindiffusion in Abhängigkeit der Ionenkonzentration.

Im zweiten Schritt wurde die stochastische optische Rekonstruktionsmikroskopie umgesetzt und dank der Verbindung mit einer der neuesten Markierungsmethoden namens SNAP-Tag verbessert. Mittels dieser Markierungsmethode, welche die kurze Anbindung (≈ 2.5 nm) von hellen und schaltbaren organischen Farbstoffen an das gewünschte Molekül erlaubt, wurden Lokalisierungsgenauigkeiten von bis zu ≈ 10 nm erzielt. Um die strengen photo-physikalischen Anforderungen von STORM zu erfüllen, mussten hingegen giftige Abbildungspufferlösungen verwendet werden, die Thiole enthalten. Im dritten Schritt stellte sich heraus, dass diese Anforderungen durch superauflösende optische Fluktuationsbildgebung (SOFI) entspannt werden konnten, was einen Fortschritt für superauflösende Beobachtungen an lebenden Zellen bedeutet.

Im dritten Schritt wurde SOFI charakterisiert, was die Grundlage für die Verbindung von funktioneller und superauflösender struktureller Bildgebungsverfahren bietet. Der Vergleich von STORM und SOFI zeigt die Stärken der Methoden auf. Unter idealen Blink-Bedingungen mit ultrastabilen langlebigen Dunkelzuständen übertrifft STORM SOFI. Falls die Farbstoffe jedoch nicht genügend freistehend sind, erreicht SOFI die höhere effektive Auflösung als STORM, ohne dabei Artefakte durch Fehllokalisierungen zu erzeugen. Dies führte zu einem neuen von SOFI abgeleiteten funktionellen Bildgebungsverfahren: Cumulant microscopy verbindet struk-

turelle Super-Auflösung mit funktioneller Bildgebung. Simulationen und Messungen haben gezeigt, dass Farbstoffe als Nanosensoren dienen können, um Parameter photo-physikalischer Eigenschaften zu bestimmen.

Schliesslich hat die Verbindung von FCS-Konzepten mit verbesserter superauflösender Mikroskopie zu einem neuen funktionellen superauflösenden Bildgebungsverfahren geführt, welches kompatibel mit lebenden Zellen ist.

Schlüsselwörter: Einzelmoleküle, funktionelle Bildgebung, Fluoreszenz-Korrelations-Spektroskopie (FCS), Nanokanal, Diffusion, Triplett Zustand, superauflösende Mikroskopie, stochastische optische Rekonstruktionsmikroskopie (STORM), SNAP-Tag, superauflösende optische Fluktuationsbildgebung (SOFI), Kumulant-Mikroskopie

Résumé

Les organismes vivants sont composés de cellules dont les structures et la fonctionnalité proviennent des protéines qui en sont les éléments de base. Aujourd'hui, les protéines d'une taille d'un nanomètre à plusieurs dizaines de nanomètres peuvent être observées efficacement par la microscopie et/ou par la spectroscopie par fluorescence qui atteignent une sensibilité de l'ordre d'une molécule. Cependant, pour mieux comprendre les processus biologiques, il est essentiel d'étudier à la fois la structure et la fonction à l'échelle moléculaire.

Ce travail élargit ainsi les possibilités des techniques d'imagerie moléculaire actuelles. Le but était de concevoir une technique d'imagerie fonctionnelle super-résolue en réunissant les concepts forts de la microscopie et de la spectroscopie modernes. Pour ce faire, les trois étapes suivantes ont été réalisées.

Dans une première étape, la spectroscopie de corrélation de fluorescence (FCS) confocale a été appliquée dans des nanocanaux afin de créer des volumes d'échantillonnage plus petits que la limite de diffraction. Il en résulte une sensibilité augmentée aux effets de surface permettant de mesurer, par FCS, la diffusion des protéines modifiée par les couches surfaciques ioniques. L'analyse de la population et du temps de vie de l'état triplet a confirmé le modèle développé pour la diffusion de protéines en fonction de la concentration ionique.

Dans une seconde étape, la microscopie par reconstruction optique stochastique (STORM) a été réalisée et améliorée en combinaison avec la technique récente de marquage SNAP-tag. Cette technique de marquage permet de lier des fluorophores brillants et commutables à la molécule visée avec une distance très courte (≈ 2.5 nm). Ceci offre une haute précision de localisation jusqu'à ≈ 10 nm. Pour répondre aux fortes exigences photo-physiques imposées par STORM, des tampons toxiques à base de thiols ont dû être utilisés. Les études de l'étape suivante ont montré que l'imagerie super-résolue par fluctuation optique (SOFI) peut assouplir ces exigences et fait ainsi un pas vers l'imagerie de cellules vivantes.

Dans la troisième étape, la caractérisation de SOFI a offert les bases pour combiner les techniques fonctionnelles et structurelles super-résolues. La comparaison entre STORM et SOFI a montré les forces de chaque technique. Sous des conditions de clignotement idéal avec des états d'obscurité ultra-stables et de grande longévité, STORM surpasse SOFI. Cependant, si les émetteurs ne sont pas bien isolés, SOFI offre une plus haute résolution que STORM et ceci, sans artefacts de localisation. Ces résultats ont abouti à une nouvelle technique de mesure dérivée de SOFI : l'imagerie des cumulants qui combine la super-résolution structurelle et l'imagerie fonctionnelle. Les simulations et les mesures ont montré que les émetteurs peuvent faire office de nano-capteurs en utilisant leurs propriétés photo-physiques.

En conclusion, la combinaison de concepts FCS avec une méthode de microscopie à haute résolution améliorée a permis de réaliser une nouvelle technique d'imagerie super-résolue fonctionnelle compatible avec des cellules vivantes.

Mots-clés : molécules individuelles, imagerie fonctionnelle, spectroscopie de corrélation de fluorescence (FCS), nanocanal, diffusion, état triplet, microscopie super-résolue, microscopie par reconstruction optique stochastique (STORM), SNAP-tag, imagerie super-résolue par fluctuation optique (SOFI), microscopie des cumulants

Contents

Abstract (English/Deutsch/Français)	v
1 Introduction	1
2 Fluorescence Sensing	5
2.1 Introduction	5
2.2 Fluorescence	6
2.3 Fluorescence Detection	8
2.3.1 Excitation	8
2.3.2 Detection efficiency	8
2.3.3 Point spread function and emission pattern	10
2.3.4 Photon count estimation	10
2.3.5 Data analysis	12
3 Fluorescence Correlation Spectroscopy in Nanochannels	13
3.1 Introduction	13
3.2 Theory & Method	14
3.2.1 Sampling volume	14
3.2.2 Data processing	15
3.2.3 Diffusion equations	18
3.2.4 Electrical double layer	21
3.3 Experimental Details	21
3.3.1 Materials	21
3.3.2 Nanochannel	22
3.3.3 Optical setup	22
3.4 Results & Discussion	23
3.4.1 Diffusion regimes as a function of ionic concentration	23
3.4.2 Triplet state measurements	30
3.5 Conclusion	32

4	Stochastic Optical Reconstruction Microscopy	33
4.1	Introduction	33
4.2	Theory & Method	35
4.2.1	Resolution, localization and super-resolution	35
4.2.2	Labeling density and its implication on the resolution	37
4.2.3	Photoswitching and blinking of Cy5	39
4.2.4	Localization algorithms	42
4.2.5	Sample drift	42
4.2.6	Image representation	44
4.3	Experimental Details	44
4.3.1	Sample preparation	44
4.3.2	Imaging buffers	46
4.3.3	Optical setup	46
4.3.4	Image acquisition and processing	47
4.4	Results & Discussion	47
4.5	Conclusion	53
5	Super-Resolution Optical Fluctuation Imaging	55
5.1	Introduction	55
5.2	Theory & Method	59
5.2.1	The principle of SOFI	59
5.2.2	The principle of cumulant imaging	61
5.2.3	SOFI-Fourier reweighting	64
5.2.4	Cross-cumulants	65
5.2.5	Signal-to-noise ratio of cumulants	66
5.3	Simulation & Experimental Details	69
5.3.1	Simulation	69
5.3.2	Experiments	71
5.4	Simulation results	71
5.4.1	Resolution enhancement with SOFI	71
5.4.2	Cumulant imaging	76
5.5	Experimental results	81
5.5.1	SOFI	81
5.5.2	Cumulant imaging	82
5.6	Discussion	83
5.7	Conclusion & Outlook	85
6	Conclusion & Outlook	87

A Cumulants and Higher Order Statistics	91
A.1 Definitions	91
A.2 Properties of Cumulants	92
A.3 Determination of Cumulants	93
A.4 Bernoulli Distribution	94
B Photo-Physical Properties of Alexa Fluor 633, Cy3 and Cy5	95
Acknowledgements	97
Bibliography	108
Curriculum Vitae	109

1 Introduction

The basic functional and structural unit of living organisms are cells. Most cell structures and processes rely in turn on proteins of the size of one to a few tens of nanometers [101]. Fluorescence microscopy allows selective access to cellular structures and processes by a careful labeling of the involved proteins. Therefore fluorescence microscopy is one of the most powerful, minimally invasive methods to investigate biological samples at the cellular level [92, 84]. In consequence, many labeling techniques and numerous fluorescent probes have been developed for this purpose [66]. Complementing the imaging, fluorescence spectroscopy makes the investigation of fast biological processes possible [41, 40]. For both, microscopy and spectroscopy, state-of-the-art fluorescence equipment enables the analysis of biological structures and processes down to a single molecule level and thus allows to observe mechanisms otherwise hidden in ensemble-averaged measurements [136, 87].

To maximize the information collected from biological specimens, it is useful to combine spectroscopy and microscopy. The objective of this work is to extend the possibilities of existing single molecule investigation techniques based on fluorescence. Combining elements of both spectroscopy and microscopy techniques opens the way to novel investigation tools providing the means for a more complete understanding of fundamental biological processes.

Single fluorescent molecules are the key element of fluorescence fluctuation spectroscopy. This term regroups techniques analyzing the spatio-temporal intensity fluctuations of single molecules [56, 94, 72, 135, 11, 81]. The origins of the fluctuations are manifold, and so are the physical quantities that are extracted from biomolecules with these techniques: Brownian motion, photo-physical properties and flow to name some applications. The recording of the intensity trace is achieved with photon counting devices such as avalanche photo diodes (APDs) or photonmultiplier tubes providing the required temporal resolution according to the observed process. A prominent technique of this group is Fluorescence Correlation Spectroscopy (FCS). This method has first been introduced in the early seventies by Elson, Magde and Webb [89]. Two decades later it became a powerful tool for the measurement of molecular dynamics and concentrations, photo-physical characteristics and binding kinetics. Due to improvements in laser technology, high numerical aperture objectives, low noise

Chapter 1. Introduction

photon detectors and above all due to the use of a confocal sampling volume, measurements on a single molecule level have been made possible [104].

In FCS, the number of molecules present in the sampling volume is limited. If there are too many molecules, the intensity fluctuation of a single molecule vanishes in the shot noise of the ensemble signal. For high molecular concentrations, as typically found in cells, the sampling volume has to be as small as possible. For instance, the evanescent field of a total internal reflection (TIR) excitation or the near-field of nanoholes can reduce the effective sampling volume by an order of magnitude compared to confocal FCS [39, 81]. In both cases, surface interactions become important and need a better characterization. In this work we realized and characterized FCS with a further reduced sampling volume using nanochannels.

As for fluorescence spectroscopy, the technological advances and the fluorescence concept enable single molecule sensitivity in microscopy. However, a remaining major challenge of far-field fluorescence microscopy is the limitation by diffraction, which causes the resolution of conventional imaging to be limited to 200 - 300 nm in lateral and 500 - 800 nm in axial direction [120]. Many small features and organelles inside cells are thus hidden. Alternative imaging methods are scanning probe microscopy [96] and electron microscopy, both achieving resolutions of a few nanometers and below. However, their use in biology is limited to surface investigations or fixed samples. Hence, there is a strong need for far-field optical imaging tools providing resolutions beyond the diffraction limit for deeper insights into biology and life science.

So far several approaches have led to improved resolutions. The first category, comprising confocal scanning microscopy, extends the resolution to the physical limit using different illumination and detection schemes without any requirement on the fluorescent emitter. While confocal microscopy can improve the resolution laterally and axially up to $\sqrt{2}$ times, structured illumination can go up to a factor of 2 [4] achieving a lateral resolution down to 100 nm [36].

In the second category, even higher resolution improvements are achieved by exploiting the photo-physical properties of the fluorescent emitters to excite and de-excite them with a nonlinear light intensity dependency. This allows the excitation of sub-diffraction areas and thus the reduction of the effective point spread function (PSF). STED (Stimulated Emission Depletion [49]) microscopy falls into this category, but also SSIM (Saturated Structured Illumination [46, 37]) or GSD (Ground State Depletion [48]). The underlying general concept was called RESOLFT (REversible Saturable Optical Fluorescence Transitions [47]).

The third category uses *stochastically and independently* fluctuating light emitters to improve the resolution. For example super-resolution localization microscopy such as STORM (STochastic Optical Reconstruction Microscopy [106]), PALM (Photo-Activated Localization Microscopy [8, 54]) and GSDIM (Ground State Depletion with Individual Molecule return [29]) and their extensions fall into this category. Acquired image series of stochastically blinking fluorescent molecules are analyzed frame by frame using image processing algorithms to

identify and localize isolated single molecules by fitting to a model of the system's PSF. More recently, Dertinger et al. [19] have introduced another technique called SOFI (Super-resolution Optical Fluctuation Imaging) analyzing the stochastic molecular blinking with higher-order statistics [20, 21].

Super-resolution techniques based on the analysis of stochastically fluctuating emitters have the advantage of being compatible with standard fluorescence microscopy equipment. For this reason, we focussed in the following on techniques related to the third category.

The automated localization algorithms used in STORM and PALM rely on the effective isolation and identification of single molecules within a diffraction-limited spot. Densely labeled structures therefore demand sufficiently long and stable molecular dark states such that there is at most one emitting molecule per diffraction-limited spot during a single frame exposure. Otherwise there is a risk for false localizations producing artifacts [126, 114]. The localizations are most accurate at low background if a thin two-dimensional (2D) section of the sample is excited only, for example by the evanescent field of a TIR illumination, temporal focusing [127] or light-sheet illumination [64]. Several approaches have been presented to achieve three-dimensional (3D) localization microscopy, with strong restrictions and requirements, though: very long acquisition times, bright fluorescent labels with ultra-stable long-lived dark states and complex optical setups [63, 62, 102, 119, 115, 88, 16, 68, 1].

Those requirements are greatly relaxed by SOFI [31]. Although this technique is based on the statistical analysis of individual fluorescent molecules, it does not rely on their isolated appearance. SOFI avoids artifacts by processing the complete intensity time trace in parallel. Furthermore, SOFI efficiently suppresses non-fluctuating background and offers inherent optical sectioning and 3D super-resolution.

Chapter 2 explains the basics in molecular fluorescence and the optical instrumentation, which are common to the studies in the subsequent chapters. The first part of this work presents the measurements of diffusing proteins in nanochannels (Chapter 3). After introducing FCS, the theoretical framework of this technique is developed and applied to reduced sampling volumes realized by nanochannels. We investigate the modified diffusion due to surface interactions and ionic concentration inside these nanochannels and confirm the derived surface influenced diffusion model by an additional triplet state analysis. The second part of this work focuses on super-resolution imaging by STORM (Chapter 4). We present the successful implementation of STORM with a custom-designed optical setup. We improved the reachable localization precision by SNAP-tag labeling [98], which reduces the distance between the label and the target molecule. In the third part of this work, SOFI as a further super-resolution technique is described and compared to STORM (Chapter 5). We reveal under which conditions SOFI can outperform STORM. In addition we propose a novel *functional* super-resolution imaging technique derived from SOFI. Simulations and experimental results demonstrate the technique. Conclusions and the outlook are given at the end of the work (Chapter 6).

2 Fluorescence Sensing

2.1 Introduction

Microscopy regroups magnifying *imaging* techniques of objects usually too small to observe by the naked eye. With spectroscopy we consider in this work techniques to analyze the temporal evolution of fast (< 10 ms) processes. In this context, spectroscopy denotes literally the observation of the time-spectrum corresponding to the autocorrelation, which is the inverse Fourier transform of the power-spectrum. For both, microscopy and spectroscopy, we used fluorescence to probe the sample. Fluorescent markers in the sample are illuminated and their emitted fluorescence is imaged on the detector. Although the emission is much weaker than the illumination, a high contrast is achieved because the illumination is separated spectrally from the emitted light. A further strength of fluorescence investigation methods is their specificity to label proteins of interest and the biocompatibility of the small markers. Hence, fluorescence spectroscopy and microscopy are ideal tools for minimally invasive investigations in biology [84]. The physics of fluorescence is explained in the following section.

The basic instrumentation needed is a fluorescence microscope. We are using an inverted epi-illumination microscope, where the excitation and detection is achieved through the same objective placed below the sample. The subsequent data analysis is accomplished with an external personal computer. The instrumentation of fluorescent microscopy or spectroscopy is resumed in a block diagram (Fig. 2.1), the elements of which are outlined in Section 2.3.

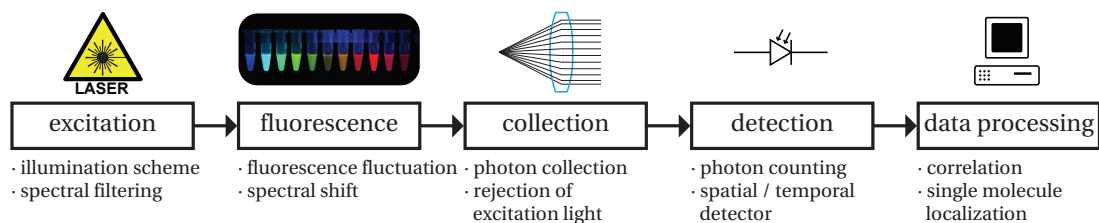


Figure 2.1: Scheme of fluorescence based optical system. A fluorescence microscope incorporates typically those building blocks.

2.2 Fluorescence

A molecule has different energy levels corresponding to its electronic, vibrational and rotational states as conveniently described with the Jablonsky diagram (Fig. 2.2). A more detailed description of fluorescence can be found in [123]. In a simplified view, the molecule is described with a three level model, including the ground state S_0 (usually singlet), the first excited singlet state S_1 and the first triplet state T_1 . These electronic states are refined with additional vibrational and rotational energy levels, illustrated by thin lines. We neglect a number of higher singlet and triplet electronic states S_n and T_n respectively, because the molecule transits very fast to the first excited singlet and triplet state S_1 and T_1 respectively (internal conversion, typically in less than 1 ns, pathway not shown). By thermal dissipation, the molecule then relaxes immediately to the lowest vibrational level (vibrational relaxation, in the order of pico seconds). Since for common fluorescent molecules the required excitation energy $h\nu > 2$ eV is much larger than the thermal energy at room temperature $k_B T \approx 26$ meV, the transition is induced by the absorption of a photon rather than by thermal excitation.

The photon absorption rate is

$$k_{ex} = \tau_{ex}^{-1} = \frac{\sigma(\lambda)}{h\nu} I_{ex}, \quad (2.1)$$

where I_{ex} is the excitation intensity. The wavelength dependent absorption cross section $\sigma(\lambda)$ is specific to a fluorescent molecule in its environment and varies as a function of the molecular orientation, more precisely of the absorption dipole moment orientation [13, 1]. Although the time-resolved rotation of molecules is accessible to optical measurements [86],

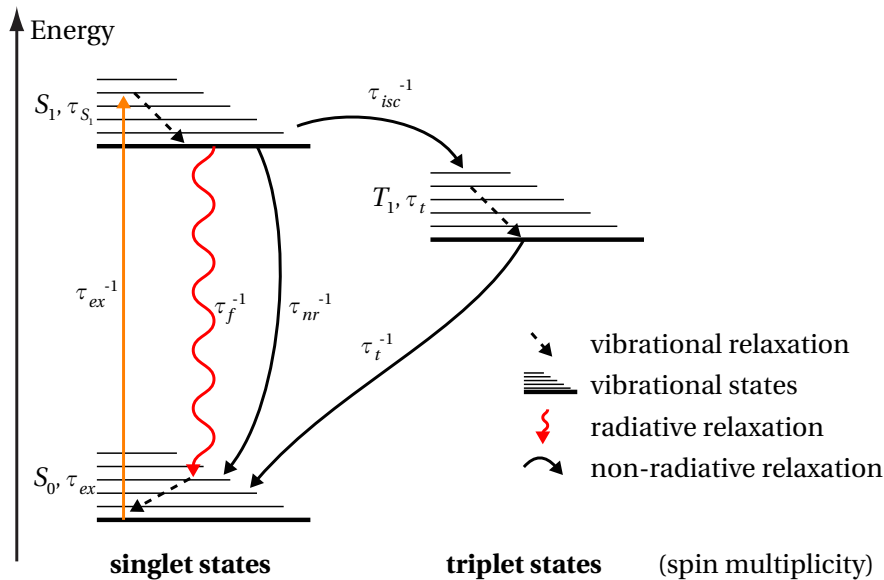


Figure 2.2: Jablonsky Diagram of a three state system with possible pathways and their transition rates.

the rotation is much faster than the acquisition rate used in this work. Hence we consider σ to be isotropic for freely rotating molecules. The following decay to the ground state can occur by a spin-allowed radiative (τ_f) or non-radiative (τ_{nr}) transition or via a spin-forbidden intersystem crossing to the first triplet state (τ_{isc}). Fluorescence is the spin-allowed radiative de-excitation of a molecule. In this case the photon emission is typically $\tau_{S_1} = 0.1 \dots 10$ ns after the absorption. The energy difference between absorbed and emitted light is called Stokes shift and is due to non-radiative decays from higher vibrational states to the lowest one of S_1 and S_0 , respectively. Thanks to this red-shift $\lambda_{ex} < \lambda_{em}$ the excitation wavelength λ_{ex} can be spectrally filtered from the emission wavelength λ_{em} leading to the required contrast enhancement in fluorescence imaging.

Organic fluorescent molecules have optimized fluorescence yields $q_f = \tau_{S_1}/\tau_f$ ranging from 10% to over 90%¹. For bright organic dyes, typically about $q_{isc} \approx 1\%$ of the total decay rate $\tau_{S_1}^{-1}$ corresponds to the spin-forbidden transition to the triplet state [25, 9]. The relaxation from this state to the ground state is in the order of microseconds to seconds due to the imposed spin flip. During this time τ_t , the molecule is not emitting light and therefore in a so-called dark state. The remaining de-excitation pathways are spin-allowed non-radiative transitions with a quantum yield of $q_{nr} = 1 - q_f - q_{isc}$.

The relative populations $p_i(t)$ for each molecular state i can be deduced by solving the rate equations of the considered three level model. The steady state of the populations is reached when their proportion remains constant in time $dp_i(t)/dt = 0$. Solving the corresponding rate equations yields the relative populations p for each state in the steady state. For the first excited singlet state S_1 this is

$$p(S_1) = \frac{\tau_{S_1}}{\tau_c}, \quad (2.2)$$

which corresponds to the mean time $\tau_{S_1} = (\tau_f^{-1} + \tau_{nr}^{-1} + \tau_{isc}^{-1})^{-1}$ spent in S_1 over the mean cycle time $\tau_c = \tau_{ex} + \tau_{S_1} + q_{isc}\tau_t$, where $q_{isc} = \tau_{S_1}/\tau_{isc}$ is the intersystem crossing probability for a molecule in the state S_1 . Analogously the population of the triplet state reads

$$p(T_1) = \frac{q_{isc}\tau_t}{\tau_c}. \quad (2.3)$$

The photon emission rate is given by

$$R_f = \frac{p(S_1)}{\tau_f} = \frac{q_f}{\tau_c} \quad (2.4)$$

with $q_f = \tau_{S_1}/\tau_f$.

¹Data from Invitrogen, California, USA

2.3 Fluorescence Detection

2.3.1 Excitation

The excitation of the fluorescence is the first step in fluorescence microscopy or spectroscopy. In order to be able to separate the fluorescence emission from the excitation, a spectrally well-defined light source is needed. Here we use laser lines of a helium-neon laser and of an argon laser. Depending on the requirements, several illumination schemes are possible. We have used a quasi-uniform wide-field illumination, objective type TIR for an exponentially decaying evanescent field with 100–200 nm penetration depth and confocal illumination [122]. The excitation volume in the confocal illumination is well approximated with a 3D Gaussian distribution (Fig. 2.3) [137].

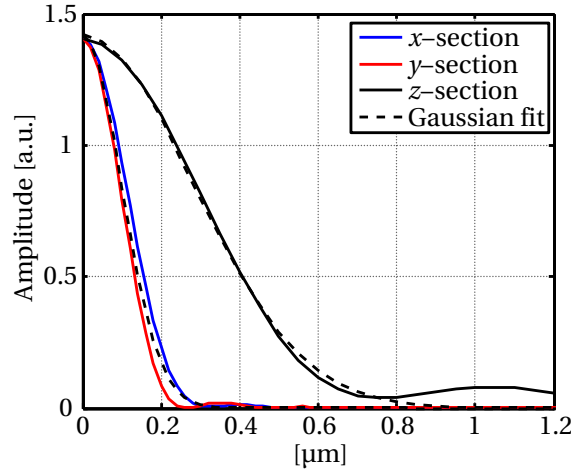


Figure 2.3: Cross sections of the focal volume generated by a water immersion objective ($NA = 1.15$, $f = 4.5$ mm) and a least-square Gaussian approximation. The field profile of the linearly x -polarized Gaussian beam has a waist of 5 mm in the objective aperture. The profiles of the excitation intensity are computed with the fast focus field algorithm published in [83].

2.3.2 Detection efficiency

The detected fluorescence is imaged on the detector. The overall detection efficiency η_{tot} is given by the ratio of detected photons N_{det} per emitted photons in the sample N_{em} :

$$\eta_{tot} = \frac{N_{det}}{N_{em}} = T_S \cdot \eta_{NA} \cdot T_{objective} \cdot T_{DM} \cdot T_L \cdot T_F \cdot \eta_{spectral} \cdot \eta_P \cdot \eta_{QE}, \quad (2.5)$$

where T_S , η_{NA} , $T_{objective}$, T_{DM} , T_L , T_F , $\eta_{spectral}$, η_P and η_{QE} are transmission (T) and efficiency (η) coefficients detailed in the following and resumed in Fig. 2.4. The estimation of the coefficients is deduced from calculations and manufacturer data sheets.

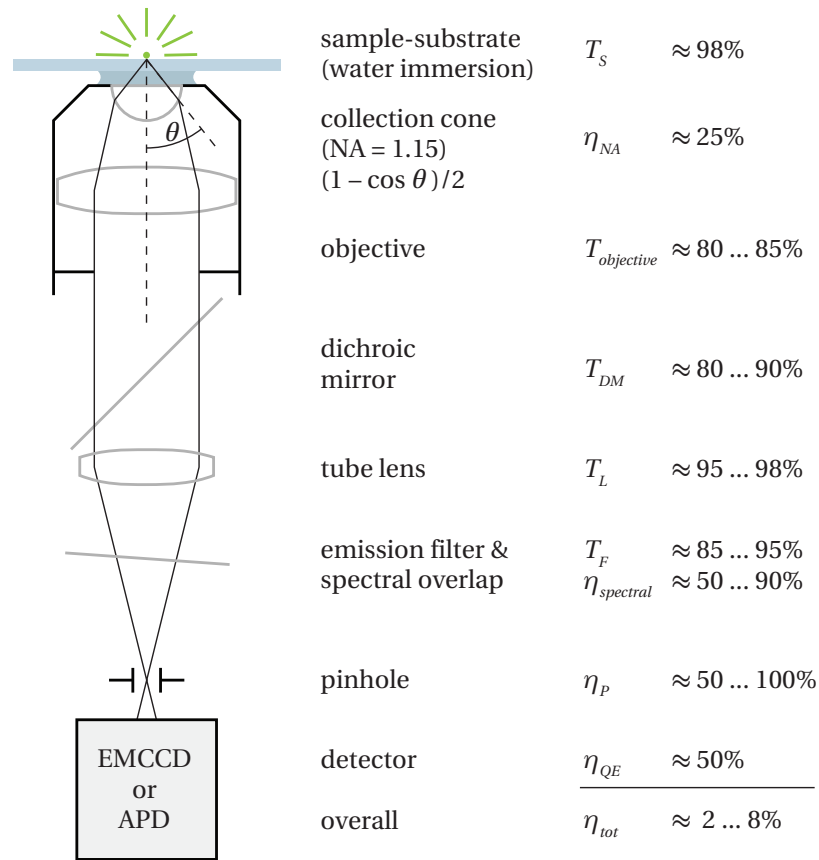


Figure 2.4: Detection path of a fluorescence microscopy or spectroscopy system. The estimation of the transmission efficiencies is given for a confocal microscope with a water immersion objective (NA = 1.15) and APD detector. The values are deduced from calculations and manufacturer data sheets.

The numerical aperture (NA) of the objective defines the geometrical cone of collection:

$$\eta_{NA} = \frac{1 - \cos \theta}{2} \quad \text{with} \quad NA = n \sin(\theta), \quad (2.6)$$

where n is the index of the immersion liquid. For a water immersion objective the cone collects up to $\eta_{NA} \approx 25\%$ of the isotropic emission. Depending on the immersion liquid and the numerical aperture, the sample-glass-liquid-objective interfaces create small additional reflections, which can be calculated by the Fresnel equations. The corresponding mean transmission over the whole collection cone is above $T_s \approx 97\%$ for water-immersion objectives and about 98% for NA = 1.15. In the case of oil immersion objectives with high NA, the collection efficiency is not simply proportional to the collection cone, but depends additionally on the emission characteristics of the emitter in proximity to the surface. The fluorescence radiation of a freely rotating emitter close to the cover slide surface is mainly directed into

the medium of higher index of refraction² and is concentrated around the critical angle of total internal reflection. A high NA oil-immersion objective can collect supercritical angles and reaches $T_S \cdot \eta_{NA} \approx 60\%$ [91, 82]. The subsequent transmission through the objective is reduced considerably due to reflections of numerous lenses in the objective³ ($T_{objective}$). Further, depending on the antireflection coating⁴, the tube lens can transmit more than $T_L \approx 99\%$, decreasing rapidly with deposited dust, though. Another loss arises from the dichroic (T_{DM}) and the detection filter⁵ (T_F). They often block parts of the emission spectrum in order to avoid cross talks between the excitation and emission bands. This reduces additionally the spectral overlap of the emitted and transmitted wavelengths ($\eta_{spectral}$). In the case of confocal detection, the pinhole usually cuts spatially some outer rings of the emission pattern (η_P , see Fig. 2.5). The quantum efficiency of the detector finally measures the ratio of generated photoelectrons per impinging photon. For an APD this is usually $\eta_{QE} \approx 50\%$ while it can reach $\eta_{QE} \approx 95\%$ or more for back-illuminated EMCCD cameras in the visible wavelength range⁶.

This yields an overall detection efficiency for a microscope with a water-immersion objective of $\eta_{tot} \approx 2 \dots 8\%$. For an oil-immersion objective (NA = 1.45) in wide-field $\eta_{tot} \approx 7 \dots 20\%$ is found.

2.3.3 Point spread function and emission pattern

Due to diffraction, the image of a point source is not an infinitely small point but a blurred spot, called point-spread function (PSF). Fluorescent molecules can be modeled as dipole emitter. Assuming freely rotating molecules, however, they can be approximated as isotropically emitting point sources. Figure 2.5 shows the emission profile of such a point source observed on the detector. Similar to the excitation volume, the emission pattern can be approximated by a Gaussian profile [137]. In contrast to the excitation, where the back aperture of the objective is not uniformly filled by the polarized Gaussian beam, the emission is unpolarized and uniform in all directions.

2.3.4 Photon count estimation

The output provided by APDs corresponds to the counts of every detected photon with high time resolution. The displayed value of an EMCCD camera, however, is usually not identical with the number of detected photons [105]. The pixel value N_{ADC} of a CCD camera corresponds to the number of accumulated photoelectrons N_Φ scaled by an analog-digital conversion factor c and the multiplication factor M superimposed with an offset o (overscan) and noise. The

²In addition, the total emission rate of a freely rotating emitter in water increases up to 20% if it is closer than $\approx \lambda/5$ to the glass surface [91, 82].

³Values found in data sheets from Zeiss, Jena, Germany and Olympus, Shinjuku, Japan.

⁴Values from Thorlabs, Newton, USA and Edmund Optics, York, UK.

⁵Values from Chroma Technology Corporation, Bellows Falls, USA and Omega Optical, Inc., Brattleboro, USA

⁶Values extracted from data sheets from Perkin-Elmer, Wellesley, USA and Andor Technology, Belfast, UK.

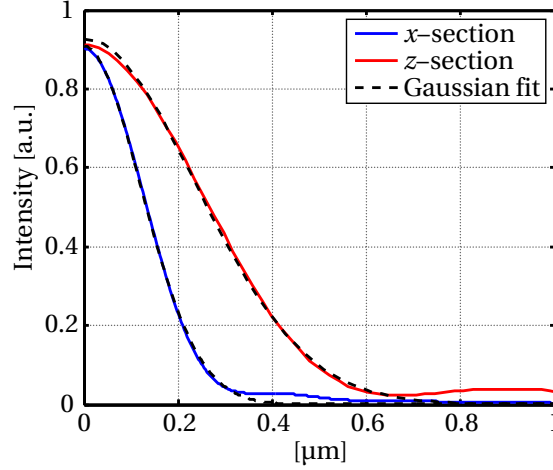


Figure 2.5: Cross sections of the emission pattern of a freely rotating single emitter generated by an oil immersion objective (NA = 1.45 and 100× magnification) and a least-square Gaussian approximation. The dimensions are given with respect to the object space. Computation according to the image formation model published in [1].

acquisition speed is limited by the serial readout rate and the shift speed of the accumulated charges. The mean pixel value, neglecting noise, can be written as

$$\langle N_{ADC} \rangle = c \langle N_{e^-} \rangle + o = cM \langle N_{\Phi} \rangle + o, \quad (2.7)$$

where N_{e^-} is the number of electrons after multiplication.

Noise (shot noise, dark noise, readout noise and multiplication noise) causes the individual pixel values to deviate from the mean value of (2.7). The noise contribution is characterized by the standard deviation $\sigma = \sqrt{\text{var}(N_{ADC})}$ where

$$\text{var}(N_{ADC}) = c^2 \left(\text{var}(N_{e^-}) + \sigma_{readout}^2 \right), \quad (2.8)$$

where $\sigma_{readout}^2$ is the variance of the readout noise, c the analog-digital conversion factor and N_{e^-} the number of electrons after multiplication. Any amplification process is accompanied by an excess noise factor $F = \sigma_{out}/(M\sigma_{in})$ increasing the amplitude of the noise σ . The variance of the electrons after multiplication can thus be written as

$$\text{var}(N_{e^-}) = M^2 F^2 \left(\sigma_{\Phi}^2 + \sigma_{dark}^2 \right), \quad (2.9)$$

where σ_{Φ} and σ_{dark} are the photon shot noise and the dark noise due to thermally created electrons. Introducing (2.9) in (2.8) we find

$$\text{var}(N_{ADC}) = (cMF)^2 \left(\sigma_{\Phi}^2 + \sigma_{dark}^2 + \frac{\sigma_{readout}^2}{(MF)^2} \right). \quad (2.10)$$

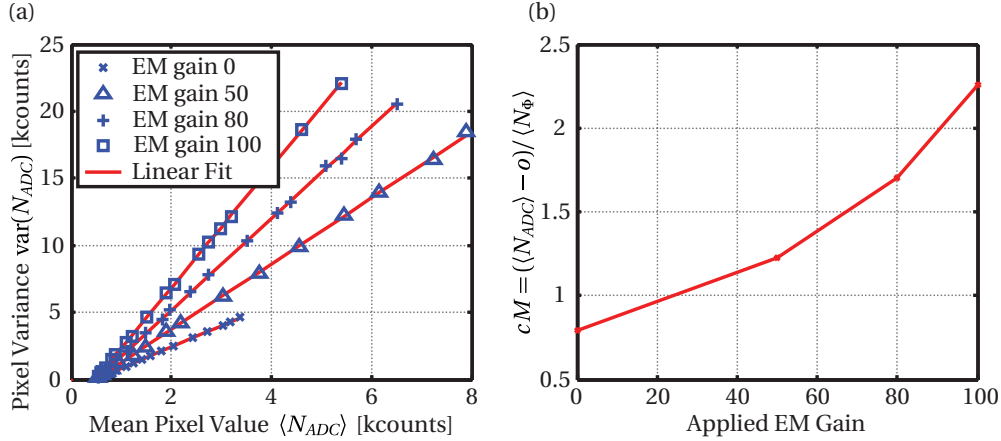


Figure 2.6: (a) Variance versus mean of the pixel value. (b) Conversion/multiplication factor versus the EM-gain value shown in Andor Solis using the Luca S 658 camera from Andor. It appears that the conversion factor c is close to $1/M$. The offset value (overscan) o is around 490 counts.

EMCCD cameras commonly have some 400 multiplication elements. It can be shown that for multiplication factors $M > 10$ (usually at least $M \approx 100$ is used), the excess noise factor F tends towards $\sqrt{2}$ due to the discrete nature of the multiplication process [105]. Neglecting the low dark noise σ_{dark} due to camera cooling and taking into account large multiplication factors $M \gg 1$, equation (2.10) can be simplified to

$$\text{var}(N_{ADC}) \approx 2c^2M^2\sigma_{\Phi}^2 = 2(cM)^2\langle N_{\Phi} \rangle, \quad (2.11)$$

where $\sigma_{\Phi}^2 = \langle N_{\Phi} \rangle$ is given by the Poisson statistics of the photon shot noise. The sensitivity of an EMCCD camera can be estimated by measuring the mean value and the variance of a homogeneously illuminated detector at several non-saturating intensities. The values for cM and o are extracted from the linear dependency shown in Fig. 2.6. The proper fitting confirms the assumption of the negligible readout and dark noise contribution. At the same time the linearity verifies the correct homogeneous illumination as well as the uniform pixel sensitivity as deviations would introduce higher order terms.

2.3.5 Data analysis

The spatio-temporal data acquired by the fluorescence detection is analyzed by a personal computer or an intermediate hardware data processing unit according to the applied technique.

3 Fluorescence Correlation Spectroscopy in Nanochannels

3.1 Introduction

Advances in microfabrication in combination with molecular biology have led to miniaturized devices for biomedical and biological analysis, a step towards lab-on-a-chip systems, which are low priced and yield rapid analysis results. Device miniaturization enhances the surface to volume ratio. This increases considerably the proportion of surface dominated processes, a key element above all in nanofluidic devices [59, 26]. As a consequence, there is a need for deeper understanding of surface interactions and diffusion of biomolecules in confined volumes, such as nanochannels which are fluidic devices with at least one dimension in the order of nanometers. The FCS measurements in nanochannels presented in this chapter show that the diffusion of proteins reveals a strong surface interaction, which can be influenced by the ionic concentration of the liquid.

This study was realized in collaboration with the Microsystems Laboratory of Philippe Renaud [103]. The nanochannels were fabricated in the clean room facilities of EPFL by Nicolas Durand who brought in the knowhow about nanofluidics. The description of the nanochannel fabrication and more details about the microfluidic setup for the liquid injection can be found in his thesis [23].

The nanochannel is a 50 nm high and 10 μm wide slit linking two microchannels over a distance of 30 μm (see Fig. 3.1). For the measurements in the nanochannel, the solutions containing the labeled proteins are injected via the microchannels. Their Brownian motion in function of the ionic concentration of the solution is investigated in the nanochannel with a focused laser beam. The focal volume has a lateral waist of $w_{xy} \approx 400$ nm and an axial extension of $w_z \approx 2.5$ μm . Hence, the lateral extension of the sampling volume is defined by the excitation beam, while the axial depth is given by the nanochannel height. Thus, the sampling volume is quasi 2D and its size is only ≈ 25 al. FCS is an ideal method to investigate the molecular motions of such systems. In FCS, the photon trace of fluorescent molecules that pass through the sampling volume is recorded and correlated with itself. By fitting

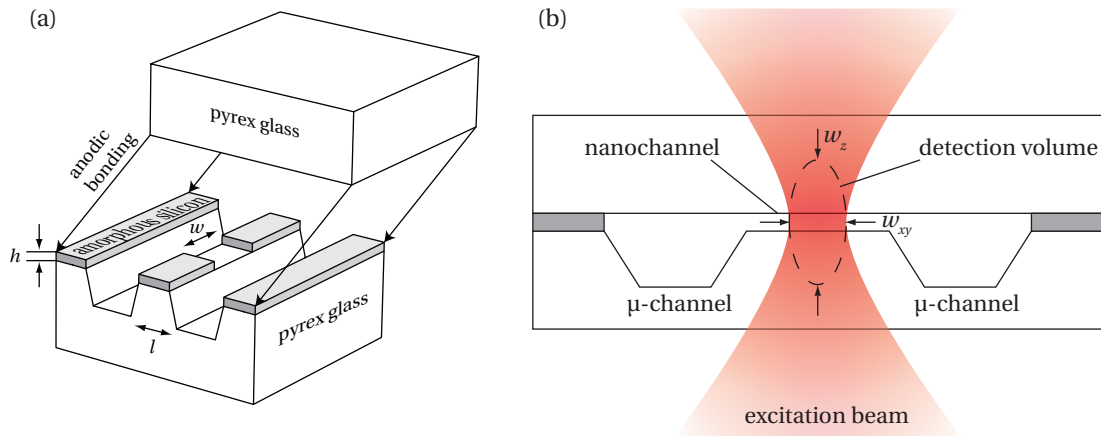


Figure 3.1: Illustration of the investigated nanofluidic device using FCS for the detection of proteins: **(a)** 3D schematic of the nanofluidic system (not to scale), which consists of two microchannels linked by a nanochannel. The nanochannel is produced by anodic bonding of two engraved pyrex glass slides. The dimensions of the nanochannel are $h = 50 \text{ nm}$, $w = 10 \text{ }\mu\text{m}$ and $l = 30 \text{ }\mu\text{m}$. **(b)** The excitation laser beam is focused on the nanochannel. The focal volume has a lateral waist of $w_{xy} \approx 400 \text{ nm}$ and an axial extension of $w_z \approx 2.5 \text{ }\mu\text{m}$.

of an adequate model to this measured autocorrelation, kinetic as well as photo-physical parameters about the molecular dynamic can be extracted [78].

Section 3.2 describes the theoretical background of FCS, which is used as the main characterization tool to measure the modified diffusion characteristics of proteins in nanochannels. A sufficient amount of detail is provided for a solid understanding of different molecular dynamics and photophysical properties and their implication on the characteristic autocorrelation function. Section 3.3 specifies the experimental details on the optical setup, the nanochannel and the materials such as proteins, buffers and fluorescent labels, which are used in this study. In Section 3.4, experimental results of the protein diffusion in the nanochannel are presented and discussed. On the basis of the results, the main conclusions of the study are summarized in Section 3.5.

3.2 Theory & Method

3.2.1 Sampling volume

The size and the distribution of the sampling volume is fundamental for FCS because the extracted parameters such as the diffusion time τ_d and the mean number N of molecules in the volume depend directly thereon. The sampling volume corresponds to the product of the sample distribution with the focal excitation and the collection volume. In free 3D diffusion, the sample distribution is uniform. Additionally in our case, the pinhole and thus the collection volume is large compared to the focal volume. Thus, the sampling volume

corresponds to the excitation field distribution, which fits well to the Gaussian distribution (Fig. 2.3)

$$I(\vec{r}) = I_0 \exp\left(-2\frac{x^2 + y^2}{w_{xy}^2} - \frac{2z^2}{w_z^2}\right) = I_0 \exp\left(-2\frac{x^2 + y^2 + \frac{z^2}{\omega^2}}{w_{xy}^2}\right), \quad (3.1)$$

where w_{xy} and w_z represent the lateral and the axial beam waist respectively. The Gaussian distribution was first proposed by [27] and is commonly used to model the sampling volume. The error introduced by this assumption has been investigated by comparing the analytical autocorrelation model to the numerical calculation of a preciser model [55]. The numerical approach, however, is computationally expensive and does not eliminate effects such as fluorescence saturation, which complicate the exact determination of diffusion parameters. For precise measurements, the two-focus FCS is the method of choice [22]. In our experiment, the relative variation of the diffusion parameters N and τ_d rather than their precise value is investigated. Therefore the used autocorrelation models based on a Gaussian approximation of the sampling volume are sufficient. This simplifies the models and their computation and gives satisfactory results. Errors due to saturation effects are avoided using the same fluorescent molecule at the same excitation intensity for a given experiment [28].

3.2.2 Data processing

In FCS, the data processing is based on the temporal correlation of the intensity trace recorded with photon counting devices such as avalanche photo diodes (APDs). An overview of the data processing is given in Fig. 3.2. The normalized autocorrelation is computed with a hardware correlator as

$$G_m(\tau) = \frac{\langle I(t)I(t+\tau) \rangle_t}{\langle I(t) \rangle_t^2} = \frac{\langle \delta I(t)\delta I(t+\tau) \rangle_t}{\langle I(t) \rangle_t^2} + 1, \quad (3.2)$$

where $I(t) = \langle I(t) \rangle_t + \delta I(t)$.

With an APD about 50% of the photons are detected in red wavelengths and virtually every detected photon is counted. A detected photon creates many electron-hole pairs by an avalanche effect. These charges are detectable and a single photon is attributed. Thereafter the avalanche effect is quenched in order to detect a new photon. Some electrons, however, remain trapped after the avalanche quenching and are released spontaneously after a previous detection event. This yields correlated delayed pulses with an exponentially decaying probability after a true photon detection. This effect is called *afterpulsing* [58]. Thermally generated electrons, on the other hand, can also induce a detection event. These *dark counts* contribute to a stationary stochastic background. This uncorrelated noise has a weak effect only on the correlation amplitude and can easily be taken into account during the diffusion model fitting (see Equation (3.12)). Afterpulsing, however, contributes to a temporally decaying autocorrelation in the order of microseconds which overlays with the triplet state kinetics.

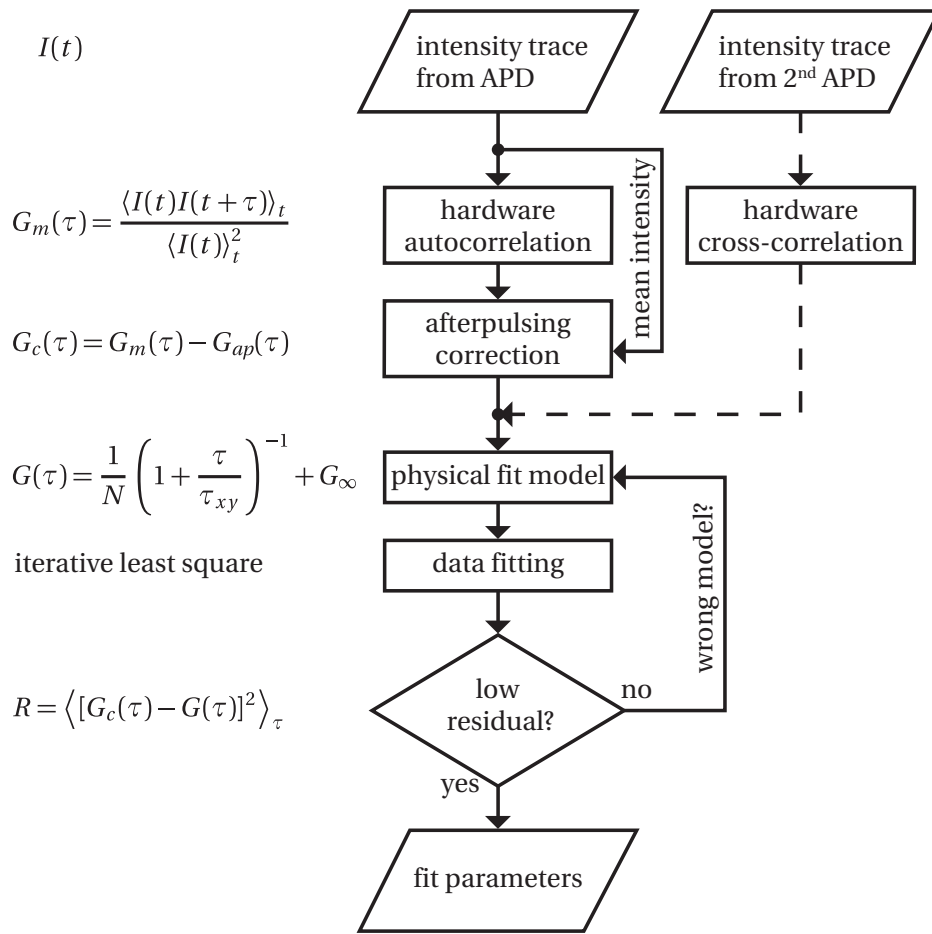


Figure 3.2: Flow chart of the FCS data processing. The autocorrelation $G_m(\tau)$ measured by a single APD is corrected for afterpulsing by subtraction of its autocorrelation $G_{ap}(\tau)$. A physical model $G(\tau)$ is fitted to the corrected autocorrelation $G_c(\tau)$. The residual R is a measure of the fit quality.

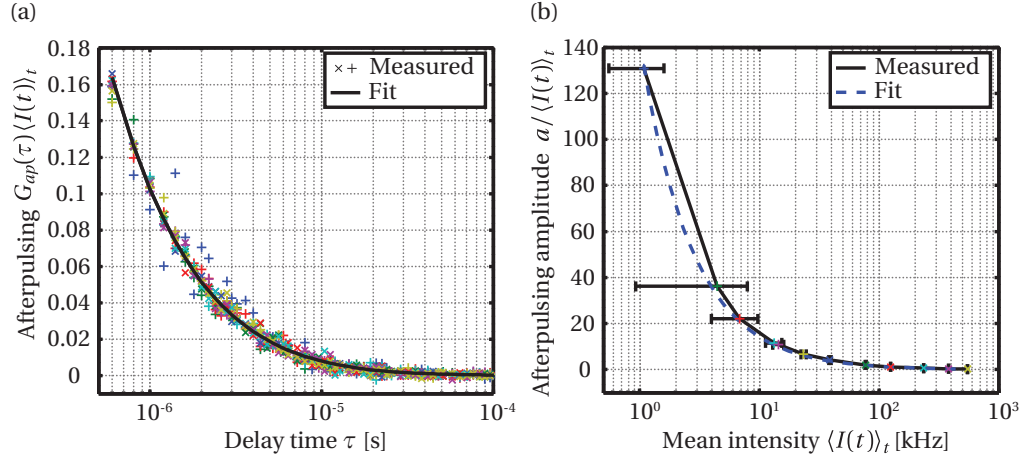


Figure 3.3: (a) Intensity-normalized afterpulsing measured with sunlight for measured intensities from 1 to 500 kcounts. The colors correspond to the mean intensities specified in (b). (b) Fitted afterpulsing amplitude.

This effect can be avoided by cross-correlating two APDs detecting the same signal followed by a 50/50 beam splitter since the afterpulsing of the two APDs is not correlated. The drawback is the decreased intensity on each detecting APD and thus, a lower signal-to-noise ratio (SNR).

Measurements done with a single APD can also be corrected for afterpulsing. The afterpulsing amplitude is inversely proportional to the mean intensity of the photon trace (Fig. 3.3 (a)) and the decay of the afterpulsing probability is nearly identical for intensity-normalized autocorrelation curves (Fig. 3.3 (b)). Therefore the afterpulsing can be removed from the autocorrelation function by subtraction of an afterpulsing contribution corresponding to the mean intensity (see Fig. 3.2) [138]. The afterpulsing contribution fits well to the empirical model

$$G_{ap}(\tau) = \frac{a}{\langle I(t) \rangle_t} \left(1 + \frac{\tau}{b}\right)^{-1} \left(1 + \frac{\tau}{c}\right)^{-1}, \quad (3.3)$$

where $\langle I(t) \rangle_t$ and τ are the mean intensity of the photon trace and the delay time of the autocorrelation, respectively. $a \approx 100$ kHz, $b \approx 10^{-7}$ s and $c \approx 2 \cdot 10^{-5}$ s are fit parameters found for our APD (see Fig. 3.3). They are specific to each device, prone to aging and should therefore be calibrated monthly or at least annually. Otherwise, these parameters are reliable in laboratory conditions and show virtually no wavelength dependency. Afterpulsing contributions have to be corrected carefully because their subtraction changes the autocorrelation $G_c(\tau)$ considerably. An independent verification of the correction is the proper shape of the autocorrelation curve (i.e. no positive slope) avoiding the subtraction of too large afterpulsing amplitudes.

FCS measurements in the nanochannel have been done with a single APD in order to maximize the SNR. The afterpulsing has been corrected numerically.

3.2.3 Diffusion equations

Following the afterpulsing correction, physical parameters of the investigated system are extracted by fitting a model to the autocorrelation function. The diffusion of molecules is driven thermally and described by the Brownian motion. The sampling volume for free 3D diffusion uniform in all directions is approximated by a 3D Gaussian volume (see Fig. 3.4 (a)). Supposing a linear fluorescence response, the autocorrelation function in FCS can then be modeled by the 3D diffusion equation [78]

$$G(\tau) = \frac{1}{N} \left(1 + \frac{\tau}{\tau_{xy}}\right)^{-1} \left(1 + \frac{\tau}{\omega^2 \tau_{xy}}\right)^{-\frac{1}{2}} + G_\infty, \quad (3.4)$$

where $\tau_{xy} = w_{xy}^2/(4D)$ is the lateral diffusion time through the focal volume and D the diffusion constant. $\omega = w_z/w_{xy}$ denotes the aspect ratio of the sampling volume and N is the average number of fluorescent molecules in the sampling volume. $G_\infty \approx 1$ is the correlation at infinite lag times.

For free Brownian motion, the diffusion in x , y and z is uncorrelated [108]. Under this assumption, the diffusion equation can be decoupled along the three spacial dimensions:

$$G(\tau) - G_\infty = \frac{1}{N} g_{xyz}(\tau) = \frac{1}{N} g_x(\tau)g_y(\tau)g_z(\tau), \quad (3.5)$$

where g_{xyz} is the normalized autocorrelation function with

$$g_x(\tau) = g_y(\tau) = \left(1 + \frac{\tau}{\tau_{xy}}\right)^{-\frac{1}{2}} \quad \text{and} \quad g_z(\tau) = \left(1 + \frac{\tau}{\tau_z}\right)^{-\frac{1}{2}}. \quad (3.6)$$

$\tau_z = w_z^2/(4D)$ is the diffusion time in axial direction.

Considering now the measurement in the nanochannel, the sample distribution is confined to a 50 nm thin slice, 500 times smaller than the axial extension of the 3D sampling volume. The excitation field and detection efficiency are virtually constant in this slice. Supposing elastic

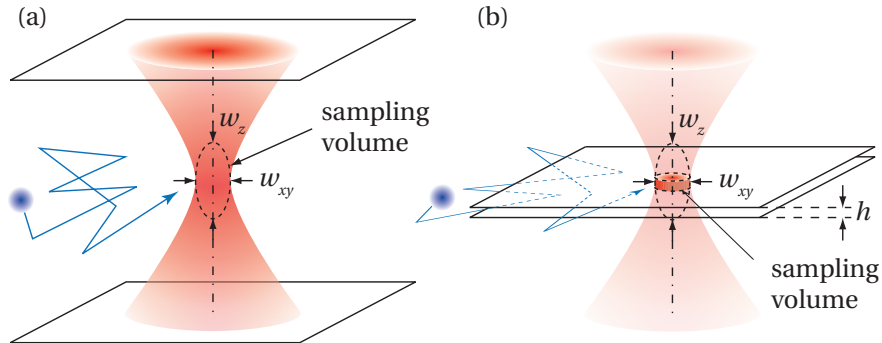


Figure 3.4: A diffusing fluorescent emitter in a (a) 3D and (b) 2D sampling volume.

collisions of the molecules with the nanochannel walls, the trajectory of the molecules is given by a reflection at the interfaces. This is equivalent to the observation of a freely diffusing molecule in a sampling volume redefined by the corresponding reflection of the excitation field and the collection efficiency distribution. The reflection at the nanochannel walls every 50 nm yields an axially virtually constant infinite sampling volume, meaning that the diffusing molecules cannot escape from the sampling volume in axial direction. This corresponds to a model of a pure 2D diffusion (Fig. 3.4 (b)). Mathematically, this means that the aspect ratio ω of the focal volume tends towards infinity and $g_z(\tau)$ towards unity. This model holds when the axially confined geometry is much smaller than the axial length of the focal volume $h \ll w_z$ [32]:

$$G(\tau) - G_\infty = \frac{1}{N} g_{xy}(\tau) = \frac{1}{N} \left(1 + \frac{\tau}{\tau_{xy}} \right)^{-1}. \quad (3.7)$$

Up to this point, ideal Brownian motion and no surface interactions were assumed where the mean square displacement is proportional with time $\langle r^2 \rangle \sim t$. However on a surface or in a cell membrane the diffusion in two dimensions may vary at different timescales because the free diffusion of the molecules is hindered by surface adsorption leading to a long tail of the autocorrelation. On a surface for example, there are binding sites with locally varying dwell times that are long compared to the diffusion. This so-called subdiffusion is commonly modeled with a non-linear time dependency of the mean square displacement $\langle r^2 \rangle \sim t^\alpha$ with $0 < \alpha < 1$ [110]. The corresponding 2D-diffusion equation in FCS then reads [111, 131, 60]

$$G(\tau) = \frac{1}{N} \left(1 + \left(\frac{\tau}{\tau_{xy}} \right)^\alpha \right)^{-1} + G_\infty. \quad (3.8)$$

In the case of multiple independently diffusing species i with an average number of fluorescent molecules N_i and the count rates per molecule ε_i , the diffusion equation is a linear combination of the autocorrelation functions G_i weighted with the square of their fluorescence intensity $\langle I_i \rangle = \varepsilon_i N_i$:

$$G(\tau) = \frac{1}{\left(\sum_i \varepsilon_i N_i \right)^2} \left[\sum_i (\varepsilon_i N_i)^2 G_i(\tau) \right] + G_\infty. \quad (3.9)$$

The modeled signal fluctuation described so far are due to the diffusion kinetics of the fluorescent molecules. The triplet state kinetics presented in Section 2.2, however, are responsible for blinking fluorescent molecules assuming that there is no detected phosphorescence. These fluctuations in the order of microseconds can be resolved with FCS and modeled by [133]

$$G(\tau) = \frac{1}{N} g(\tau) \left[1 + \frac{p(T_1)}{1 - p(T_1)} \exp\left(-\frac{\tau}{\tau_b}\right) \right] + G_\infty. \quad (3.10)$$

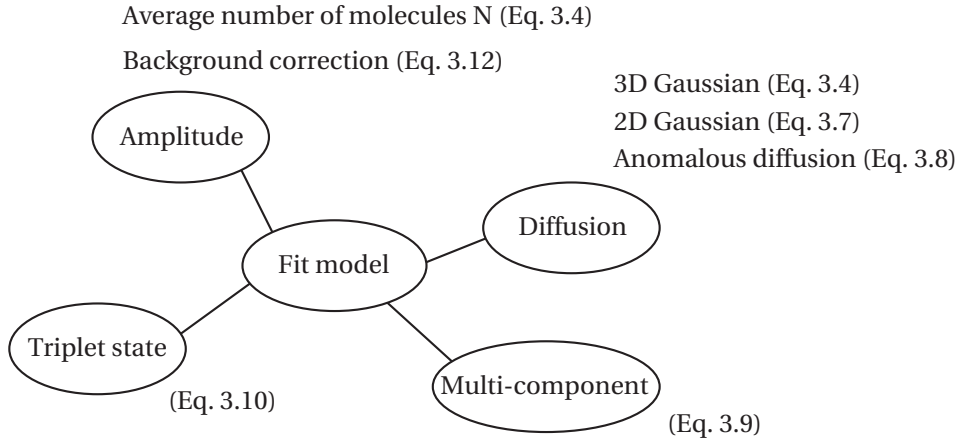


Figure 3.5: Overview of the contributions (factors) of a diffusion model.

From the total average number of molecules N , the fraction $p(T_1)$ are dark molecules assumed to be in the first (or higher) triplet state T_1 . Taking into account that $\tau_{10} \ll \tau_t, \tau_{isc}$, the bunching time τ_b can be expressed with good approximation (error < 1%) by

$$\frac{1}{\tau_b} \approx \frac{1}{\tau_t} + \frac{\tau_{10}}{\tau_{isc}(\tau_{10} + \tau_{ex})} \approx \frac{1}{\tau_t} \frac{1}{1 - p(T_1)}, \quad (3.11)$$

where the latter approximation uses the steady state of the triplet state population (see Section 2.2 and Fig. 2.2). τ_t is the triplet state lifetime and τ_{ex}^{-1} , τ_{10}^{-1} and τ_{isc}^{-1} are the rate of excitation, de-excitation and intersystem crossing, respectively. The de-excitation rate is the sum of the radiative (fluorescent) and the non-radiative decay rate $\tau_{10}^{-1} = \tau_f^{-1} + \tau_{nr}^{-1}$.

The amplitude of the autocorrelation without triplet state contribution is proportional to $1/N$ assuming no background fluorescence, i.e. no photon is collected when there is no molecule in the sampling volume. Practically there is often a considerable uncorrelated background fluorescence originating from autofluorescence of immersion liquid, glass and other sample components. In this case, the amplitude has to be corrected. The autocorrelation model then reads

$$G(\tau) = \frac{1}{N} \left(1 - \frac{I_{bg}}{\langle I(t) \rangle_t} \right)^2 g(\tau) + G_\infty, \quad (3.12)$$

where $\langle I(t) \rangle_t$ is the total average intensity and I_{bg} the uncorrelated background fluorescence and dark counts of the APD [77, 55].

An overview of the diffusion equations and their factors is given in Fig. 3.5.

3.2.4 Electrical double layer

At the interface of a solid or a particle and water, surface charges may be created [99]. Glass for instance presents a negative surface charge in a aqueous solution at neutral pH because of hydroxyl groups formed at the glass surface. In an ionic solution, the charged surface is covered with a thin layer of adsorbed and free counterions. The ions are subsequently rearranged with a net charge near the interface and a transition towards the neutral solution away from the interface. This arrangement of the ions is called electrical double layer (EDL). It applies not only to charged surfaces of a bulk, but also to charged particles or molecules.

The extension of the EDL can be estimated with the Poisson-Boltzmann equation. This equation can be linearized under the Debye-Hückel approximation, i.e. for a low surface potential compared to the thermal energy. This yields an exponentially decaying field potential with a characteristic length λ_D corresponding to the layer thickness [99]

$$\lambda_D = \sqrt{\frac{\epsilon_0 \epsilon_r RT}{2F^2 c_i}} \approx \frac{0.3 \text{ nm}}{\sqrt{c_i}}, \quad (3.13)$$

where R , T and F are the gas constant, the absolute temperature and the Faraday constant, respectively. ϵ_0 and ϵ_r are the vacuum permittivity and the dielectric constant of the medium, respectively. For water at room temperature, the static dielectric constant is $\epsilon_r \approx 80$. The introduction of all constants at room temperature yields the latter approximation, where the ionic concentration c_i is given in M. For an increasing ionic concentration, the EDL gets smaller because more ions are present to shield the surface charges. From molar to millimolar concentrations, the Debye length is from one to some tens of nanometers.

3.3 Experimental Details

3.3.1 Materials

To investigate and characterize the hindered diffusion of proteins in nanochannels, we used wheat germ agglutinin labeled with Alexa Fluor 633 (WGA, from Molecular Probes). WGA has a molecular mass of 38 kDa, an isoelectric point of $pI \approx 4$, and a free diffusion coefficient in water of $D_{bulk} = 76 \pm 3 \mu\text{m}^2/\text{s}$ [95].

These WGA proteins have been added to potassium chloride (KCl) solutions, which have been prepared with different dilutions (10^{-5} M to 10^{-1} M) via the addition of deionized water ($18 \text{ M}\Omega \text{ cm}$). The concentration of the WGA proteins was 200 nM in all prepared solutions, which were adjusted to pH 7 via the addition of a small amount of HCl. For all experiments, no pretreatment was performed on the chip in which the solutions have been directly injected. The prepared solutions were degassed before use at room temperature ($T = 25$).

The ionic concentration and the pH of the solution are subject to degradation within minutes when exposed to air. Therefore the imaging buffer was freshly prepared on the day of the

experiment. The accuracy of the preparation of the ionic concentrations are estimated by comparing the measured and the expected conductivity of the solution.

3.3.2 Nanochannel

Cleanroom microfabrication processes have been used to produce the fluidic chips on which the experiments have been carried out. Microchannels have been wet-etched on a 200 μm thick Pyrex wafer using standard lift-off techniques, and a 50 nm layer of amorphous silicon, used to define the height of the nanochannel, was sputtered and structured by plasma etching. A second Pyrex wafer that contained access holes (drilled by sandblasting) was anodically bonded onto the first wafer. Finally, the wafers were diced into individual chips. The nanochannel had the following dimensions: height, $h = 50$ nm; width, $w = 10$ μm ; and length, $l = 30$ μm . The solutions containing proteins were injected in the microchannels through the inlets. The liquids were driven by air aspiration that was controlled using air-pressure regulators (Bellofram Corp., Newell, WV) from 0 to -800 mbar. For all measurements, flow conditions have been chosen where there is no flow across the nanochannel.

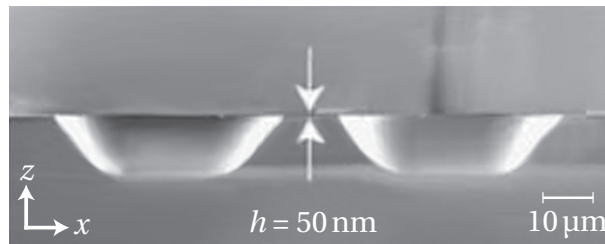


Figure 3.6: SEM image of the two microchannels linked with the nanochannels.

3.3.3 Optical setup

The measurement of the molecular diffusion in the nanochannel were performed on a ConfoCor II FCS microscope (Carl Zeiss, Jena). The fluorescent molecules were excited with about 80 μW at 632.8 nm with a HeNe laser through an Olympus UApo 340 (40 \times 1.15w) objective in epi-illumination (see Fig. 3.7). The fluorescence collected with the same objective and through a pinhole of 50 μm diameter was recorded with an APD (PerkinElmer), hardware-autocorrelated (ALV-5000/E) and analyzed with a customized Matlab code (MathWorks, Inc., Natick, USA).

For the calibration of the FCS system, we measured 25 nM and 50 nM of Cy5 in water. Using the diffusion constant $D_{\text{Cy5}} = 370 \pm 15$ $\mu\text{m}^2/\text{s}$ [85], we estimated the waist of the effective sampling volume to $w_{xy} = 410 \pm 20$ nm laterally and $w_z = 2.3 \pm 0.4$ μm axially. Since the image of the pinhole is much larger than the excitation volume, the confocal sampling volume is mostly defined by the excitation. The saturation intensity of Cy5 is measured to be about at 300 μW . At 80 μW , the sampling volume does not increase considerably. For Alexa 633 however, the saturation intensity is about 8 times lower, which changes the effective sampling

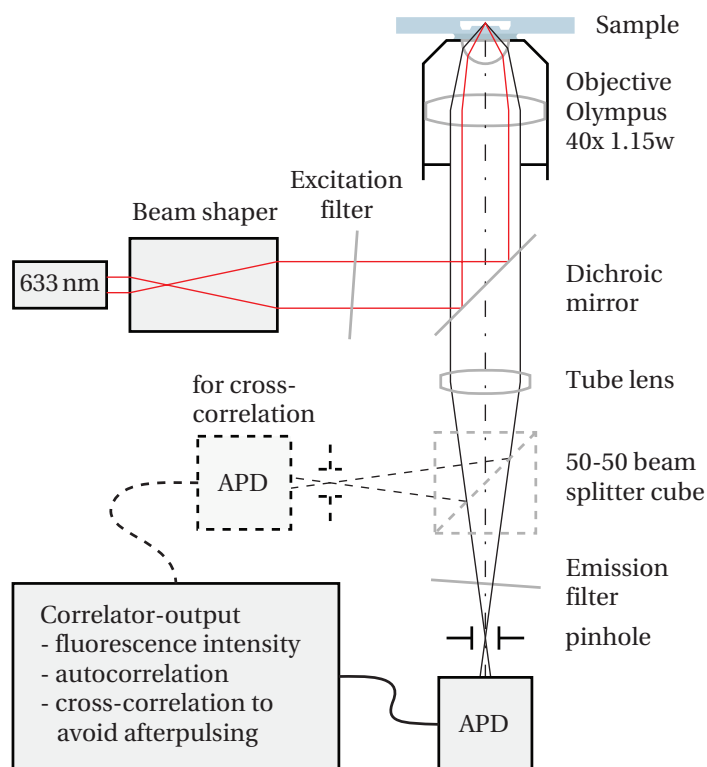


Figure 3.7: Inverted microscope in confocal configuration used for FCS measurements.

volume and the apparent diffusion coefficient (see Appendix B). Nevertheless, the study of diffusion measurements is correct as long as the sample is investigated with the same excitation intensity and compared to measurements with the same fluorescent dye Alexa 633.

The intensity trace was recorded with a single APD in order to maximize the SNR. Subsequently, the afterpulsing was corrected numerically. The measurement of three to nine successive measurements are used to estimate the accuracy of the extracted parameters.

3.4 Results & Discussion

3.4.1 Diffusion regimes as a function of ionic concentration

The diffusion and the protein concentration of labeled WGA in our nanochannel have been measured with FCS for ionic concentrations from $230 \mu\text{M}$ to 370 mM [24]¹. In the case of freely diffusing labeled WGA in water, the 3D-diffusion equation (3.4) is applied. The measurement yields a diffusion time of $\tau_{xy} \approx 0.53 \text{ ms}$ through the focal volume, independent of the ionic concentration. This corresponds to an apparent diffusion constant of $D_{WGA} \approx 78 \mu\text{m}^2/\text{s}$, which is consistent with the value found in literature ($D_{WGA} = 76 \pm 3 \mu\text{m}^2/\text{s}$ [95]). Compared to free

¹Small deviation of measured quantities from the published values [24] are due to additional subsequent measurements and reevaluations without consequences on the conclusion.

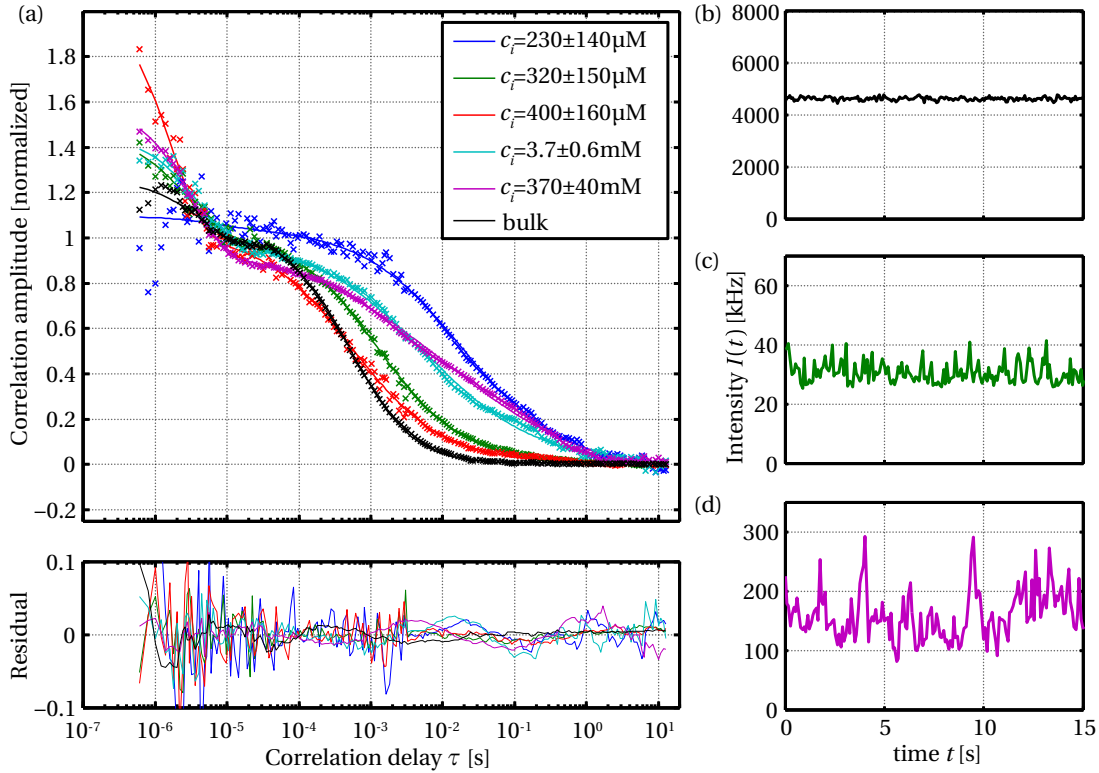


Figure 3.8: Excerpt of FCS raw data of 38 kDa wheat germ agglutinin with Alexa Fluor 633 in a 50-nm-high nanochannel for solutions with different ionic concentrations at pH 7. **(a)** Normalized autocorrelation correlation curves and fits with residuals. The diffusion and the triplet state depend clearly on the ionic concentration. The fitting is according to (3.15). **(b-d)** Photon traces for free diffusion **(b)** and for surface dominated diffusion in the nanochannel at 320 μM **(c)** and at 370 mM **(d)** ionic concentration.

Brownian motion in bulk, the apparent diffusion time observed in our nanochannel is strongly increased. In addition, in the nanochannel this diffusion depends on the ionic concentration of the buffer solution contrary to the virtually independent diffusion in bulk. This trend is directly visible on the autocorrelation curves (Fig. 3.8). At ionic concentrations of around 0.4 mM KCl, the diffusion is close to free diffusion. Above all at higher ionic concentrations, the diffusion is much slower (Table 3.1). The proteins no longer diffuse by Brownian motion only, but their surface interaction is strongly influenced by a reversible adsorption depending on the ionic strength of the solution. This is the underlying physical interpretation of the strong increase of the diffusion time observed in these nano-confinements. The photon trace shows indeed pronounced peaks interpreted as adsorbed molecules with a broad distribution of sticking times (see Fig. 3.8).

As presented in the published work [24], one could think of two populations of the same molecule: freely diffusing molecules with $\tau_{bulk} = 0.53$ ms and molecules interacting with the surface presenting an anomalous diffusion with $\alpha = 0.45$ and $\tau_{surf} = 10$ ms, which corresponds

c_i [mM]	τ_{app} [ms]	τ_{xy} [ms]
370 ± 40	9.9 ± 0.2	
3.7 ± 0.6	8.7 ± 0.9	\vdots
0.41 ± 0.16	2.6 ± 0.4	0.53 ± 0.01
0.32 ± 0.15	3.9 ± 0.5	\vdots
0.23 ± 0.14	> 10	

Table 3.1: Measurement results. Apparent diffusion times τ_{app} in the nanochannel and the diffusion time τ_{xy} of free 3D diffusion as a function of the ionic concentration of the solution. The apparent diffusion time is the weighted average of the bulk diffusion and the surface diffusion (see [24])

to the diffusion at the highest ionic concentration and the strongest surface interaction. The two populations are assumed to have the same count rates ε because these populations consist of the same fluorescent molecules and the collection efficiency is almost independent of the distance to the higher index medium (glass) for a water-immersion objective. However, fluorescent molecules in solution close to the glass interface have an enhanced radiative emission due to the higher local density of states in the high index medium [50, 82]. In addition, the non-radiative decay rate may be different, due to a modified microenvironment. Nevertheless, the assumption of a constant count rate ε is justified since this surface enhancement is comparable to the accuracy of the estimated number of molecules.

The axial confinement $h = 50$ nm given by the nanochannel is small enough compared to the axial extension of the confocal volume $w_z \approx 2$ μm to consider the diffusion as purely 2D [32]. In addition, the lateral confinement is wide enough ($w_{xy} \approx 410$ nm) that the Brownian motion is uncorrelated in x , y and z such that the three space dimensions can be decoupled [108].

Combining the two-component model with 2D diffusion including anomalous diffusion and background correction yields the following diffusion model:

$$G(\tau) = \left(1 - \frac{I_{bg}}{I_{tot}}\right)^2 \frac{1}{N} \left[\frac{N_{bulk}}{N} \frac{1}{1 + \tau/\tau_{bulk}} + \frac{N_{surf}}{N} \frac{1}{1 + (\tau/\tau_{surf})^\alpha} \right] \left[1 + \frac{P_t}{1 - P_t} \exp\left(-\frac{\tau}{\tau_b}\right) \right] + G_\infty, \quad (3.14)$$

where $N = N_{bulk} + N_{surf}$ is the total number of fluorescent molecules.

The extracted values for the number of total molecules N and the total intensity $I_{tot} = \langle I(t) \rangle_t$ show both a decrease for lower ionic concentrations (Fig. 3.9 (a)). At the same time the Debye length of the EDL increases as ionic concentrations decrease and reaches a size comparable to the nanochannel height. This consequently reduces the effective size of the nanochannel and reduces directly the total number of diffusing molecules measured in the observation volume. In other words, the negative surface charges of the glass are less and less shielded repelling

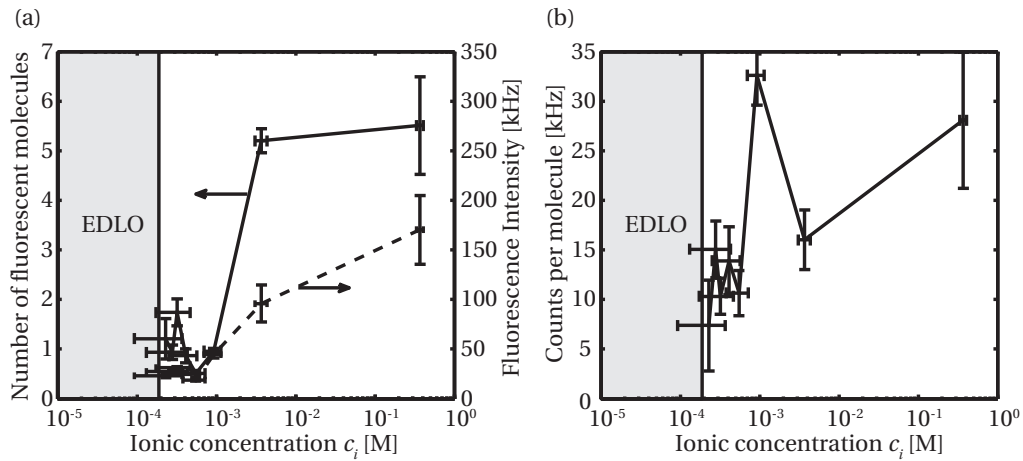


Figure 3.9: (a) The number of fluorescent molecules and the recorded fluorescence intensity in the nanochannel showing a molecular exclusion at low ionic concentrations. (b) Count rate per molecule ε in function of the ionic concentration. EDLO is the regime of low ionic concentration with an electrical double layer overlap. The solid line is with respect to the lefthand scale bar, the dashed line to the righthand scale bar as indicated by the arrows.

and excluding more and more of the negatively charged molecules. As stated before, the the molecular emission rate increases slightly at the surface [50, 82]. This is supported by the counts per molecule $\varepsilon = \langle I(t) \rangle_t / N$, which seem to lower for small ionic concentrations (Fig. 3.9 (b)). The count rate is between 10 and 30 kHz, comparable to bulk measurements with 15 to 20 kHz. Below 0.2 mM, the EDL from both sides of the nanochannel start to overlap (electrical double layer overlap, EDLO). In that case, most of the molecules do not enter the nanochannel anymore. The reduced number of molecules degrades the SNR and consequently results in a lower measurement accuracy indicated with vertical error bars. At the same time, low ionic concentrations (< 1 mM) are less reliable, which introduces another source of error displayed by horizontal error bars. In the region of the EDLO the fluorescence signal and the ionic concentration accuracy are too small for precise measurements.

The number of molecules and the counts per molecule are subject to uncertainties or bias of usually around 10–20% or more. This could arise from an underestimation of the background fluorescence, a slightly misaligned setup or a less saturated excitation if the focus is not optimally placed in the nanochannel. Therefore further parameters have been investigated. The proportions of the populations or the diffusion time constants, for instance, are more robust with respect to these error sources.

For decreasing ionic concentrations, the fraction of free molecules N_{bulk} increases up to a concentration of about 0.4 mM and decreases thereafter (Fig. 3.10). The highest fraction of free molecules corresponds to the fastest diffusion (Fig. 3.8). The fraction of molecules interacting with the surface is complementary to the fraction of free molecules.

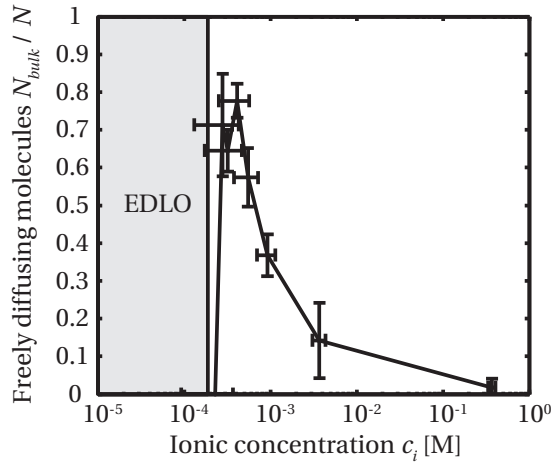


Figure 3.10: Fraction of freely diffusing fluorescent molecules. At 0.4 mM almost 80 % of the molecules behave like in bulk. Fixed parameters: $\tau_{bulk} = 0.53$ ms, $\tau_{surf} = 10$ ms and $\alpha = 0.45$

The observed diffusion behavior can be explained by the EDL which is formed on the negatively charged glass surfaces and around the negatively charged molecules. As a function of the ionic concentration, the EDL shields the electrostatic charges. The higher the concentration is, the thinner the EDL is and the more the molecules interact with the surfaces (see Fig. 3.11). For very low concentrations, only few negatively charged molecules enter the channel because the negatively charged weakly shielded glass surface repels the molecules. If a molecule still enters, then the electrostatic field distribution is almost flat making surface interactions again probable.

The results described above are published [24] and are summarized in Table 3.2.

c_i [mM]	N	N_{bulk}/N	CPM
370 ± 40	5.6 ± 1.0	$2 \pm 2.4\%$	24 ± 6.8
3.7 ± 0.6	5.3 ± 0.2	$14 \pm 10\%$	13 ± 2.3
0.41 ± 0.16	0.93 ± 0.13	$78 \pm 4.5\%$	6.3 ± 1.2
0.32 ± 0.15	1.80 ± 0.28	$65 \pm 5.5\%$	5.8 ± 1.0
0.23 ± 0.14	1.26 ± 0.44	0%	3.1 ± 1.7

Table 3.2: Summary of the measurement results. The assumed fixed parameters of the two populations are: $\tau_{bulk} = 0.53$ ms $\tau_{surf} = 10$ ms and $\alpha = 0.45$.

The previous diffusion model assumed two molecular populations with fixed diffusion parameters τ_i and α_i . These parameters have been chosen iteratively according to the best fits, i.e. the lowest residuals. However, every additional fit parameter decreases the quality of the extracted values. Therefore we tried to reduce the number of fit parameters. The following

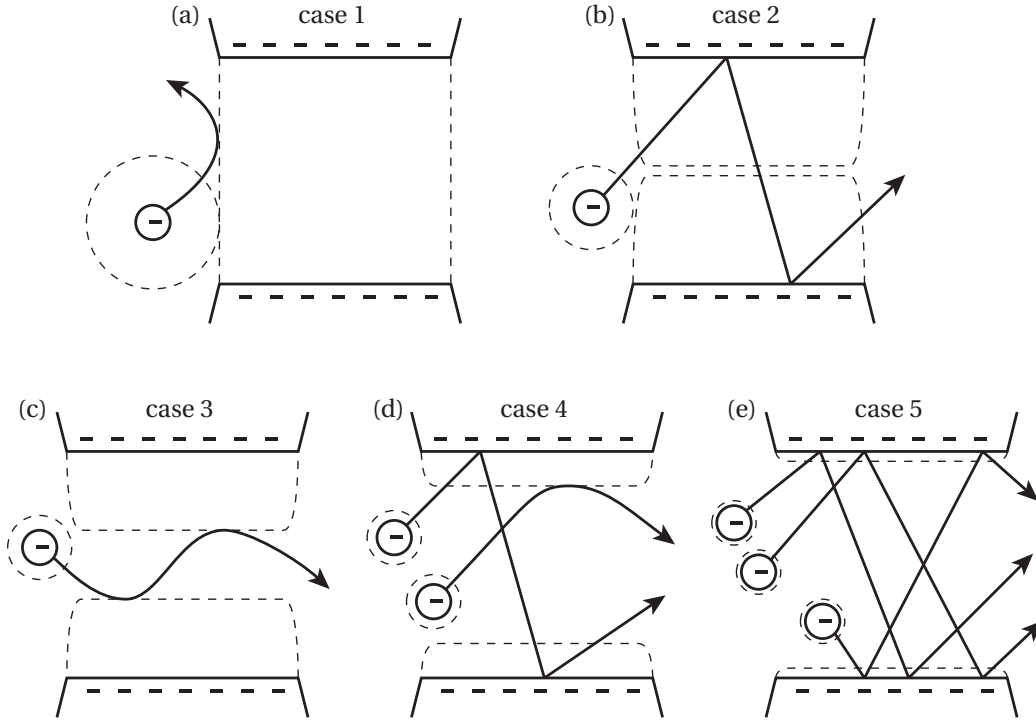


Figure 3.11: Schematics of the typical behavior of negatively charged biomolecules inside a nanochannel with negatively charged surfaces, at different ionic strengths. Our model is based on the diffusion time and the anomalous diffusion factor indicating surface adsorption: **(a)** at very low ionic concentrations, the EDL closes the nanochannel and virtually no molecule enters the sampling volume; **(b)** when increasing the ionic concentration, few molecules enter in the nanochannel interacting strongly with the surfaces; **(c)** most of the molecules do not interact with the surfaces when the EDL has an optimal extension; **(d)** increasing the ionic concentration further, more molecules enter the sampling volume and some molecules interact again with the surfaces; and **(e)** at high ionic concentrations, the EDL is thin and does not prevent most molecules from interacting with the surfaces.

simplified diffusion model goes further than the published work and confirms the previous results. The resulting fit residuals are comparable or smaller than with the original diffusion model. We consider a single-component 2D diffusion model including anomalous diffusion and background correction:

$$G(\tau) = \frac{1}{N} \left(1 - \frac{I_{bg}}{\langle I(t) \rangle_t} \right)^2 \left(1 + \left(\frac{\tau}{\tau_{xy}} \right)^\alpha \right)^{-1} \left[1 + \frac{P_t}{1 - P_t} \exp \left(-\frac{\tau}{\tau_b} \right) \right] + G_\infty. \quad (3.15)$$

The surface interactions are modeled with the anomalous diffusion factor α . Unlike in the previous model, the extracted parameters correspond to an average over the two populations, the freely diffusing and the surface-bound molecules.

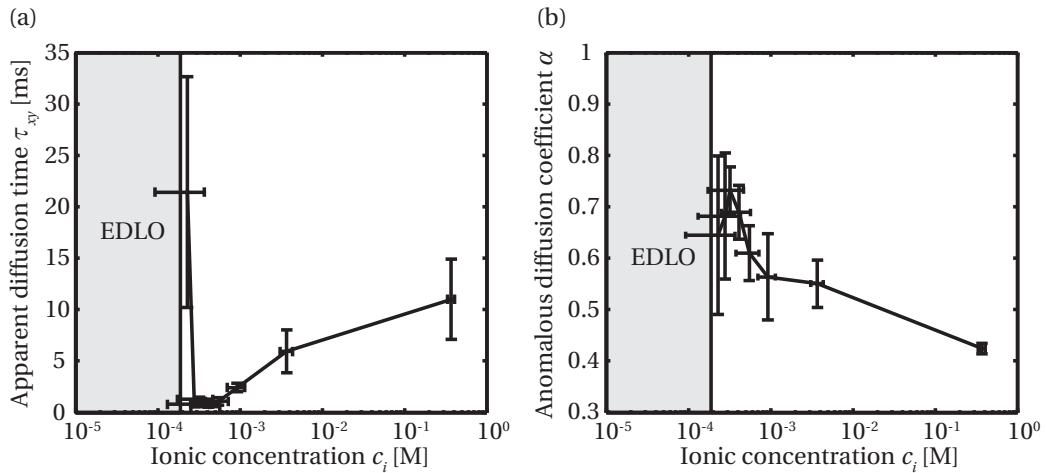


Figure 3.12: (a) Diffusion time τ_{xy} and (b) anomalous diffusion parameter α in the nanochannel in function of the ionic concentration.

The previously observed dependency of the ionic strength is confirmed by the fitted parameters τ_{xy} and α (Fig. 3.12). For decreasing concentrations the diffusion time τ_{xy} diminishes which goes together with an increasing anomalous diffusion parameter α meaning less and less surface interactions. For very low concentrations, the plots indicate again a longer diffusion time and more surface interactions. This data point shows a strong uncertainty, though, which is probably related to the low fluorescence signal, the pronounced molecular sticking (see Fig. 3.8) and the inaccurate low ionic concentration.

At low concentrations around 0.4 mM, the diffusion time reaches almost the one of free diffusion (see also Fig. 3.8). Under these conditions, the anomalous diffusion parameter $\alpha = 0.7$ indicates reduced surface interactions. The molecules seem to be guided smoothly with low surface interactions between the two EDLs.

These results are summarized in Table 3.3 confirming the original model published in [24].

c_i [mM]	τ_{xy} [ms]	N	α	p_n [ns]	τ_t [μ s]
370 ± 40	11 ± 3.9	5.5 ± 1.0	0.43 ± 0.011	14.5 ± 6.1	5.5 ± 0.4
3.7 ± 0.6	5.9 ± 2.1	5.2 ± 0.24	0.55 ± 0.046	20.5 ± 4.4	6.2 ± 1.3
0.41 ± 0.16	0.5 ± 0.05	0.86 ± 0.14	0.69 ± 0.052	35.5 ± 6.6	3.6 ± 0.7
0.32 ± 0.15	1.3 ± 0.23	1.74 ± 0.27	0.73 ± 0.045	26.3 ± 8.2	5.1 ± 1.9
0.23 ± 0.14	21 ± 11	1.21 ± 0.41	0.64 ± 0.154	1.83 ± 2.51	6.7 ± 3.2

Table 3.3: Summary of the measurement results with the one-population anomalous diffusion model (Equation (3.15))

3.4.2 Triplet state measurements

In the published work, the impact of the surface dominated diffusion on the photo-physical properties of the fluorescent molecule, in particular the triplet state, have not been considered. In this section we report additional results in this regard.

Besides the influence of the ionic concentration on the diffusion properties, the autocorrelation reveals effects on the triplet state lifetime and population (see Fig. 3.8 and Fig. 3.13 (a)). In the case of the almost free diffusion around 0.4 mM ionic concentration, a higher triplet population is observed compared to ionic concentrations with surface dominated diffusion. At the same time, the triplet population depends also on the fraction of excited molecules $p(S_1) = \tau_{S_1}/\tau_c$ and thus on the counts per molecule $\varepsilon = \eta_{tot}R_f = \eta_{tot}p(S_1)q_f/\tau_{S_1}$, where η_{tot} is the collection efficiency. Since the used objective collects only the emission of subcritical angles, the collection efficiency can be considered as constant and is estimated to $\eta_{tot} \approx 10^{-3}$ by considering typical values for $q_{isc} \approx 1\%$, $\tau_t \approx 5 \mu\text{s}$ and $q_f \approx 30\%$ corresponding to Alexa Fluor 633 (see Section 2.2 and Appendix B) [53, 76].² Taking this into account, we define an excitation normalized triplet population $p_n(T_1)$ as

$$p_n(T_1) = \frac{p(T_1)}{R_f} = \frac{q_{isc}\tau_t}{\tau_c} \frac{\tau_c}{q_f} = \tau_t \frac{q_{isc}}{q_f} = \tau_t \frac{\tau_f}{\tau_{isc}}. \quad (3.16)$$

This normalized triplet state population is virtually independent of the excitation and reveals the affinity to fall in a triplet state (see Fig. 3.13 (b)). The affinity is more pronounced for the concentration of 0.4 mM with the fewest surface interactions.

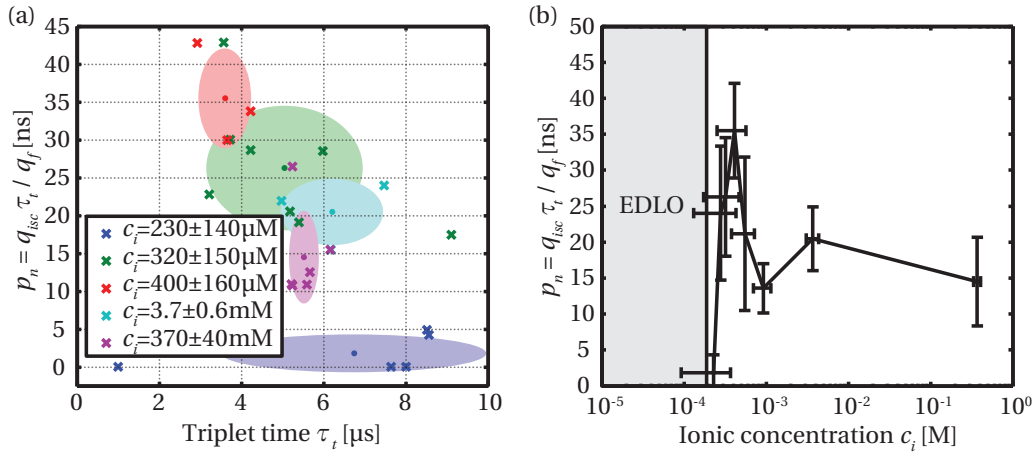


Figure 3.13: (a) Normalized triplet population and lifetime at different ionic concentrations. The crosses are the measurements and the ellipses represent their standard deviation. (b) The excitation normalized triplet population. $p_n = p(T_1)\eta_{tot}/\varepsilon$, where $p(T_1)$ is the measured triplet population, ε are the counts per molecule and $\eta_{tot} \approx 10^{-3}$ is the collection efficiency function. At the free diffusion around 0.4 mM a strong increase of the product $\tau_{isc} \cdot q_{isc}/q_f$ is observed.

²The discrepancy of η_{tot} of one order of magnitude compared to the estimation in Section 2.3.2 is not explained, but has no effect on the qualitative discussion of the results and the conclusions.

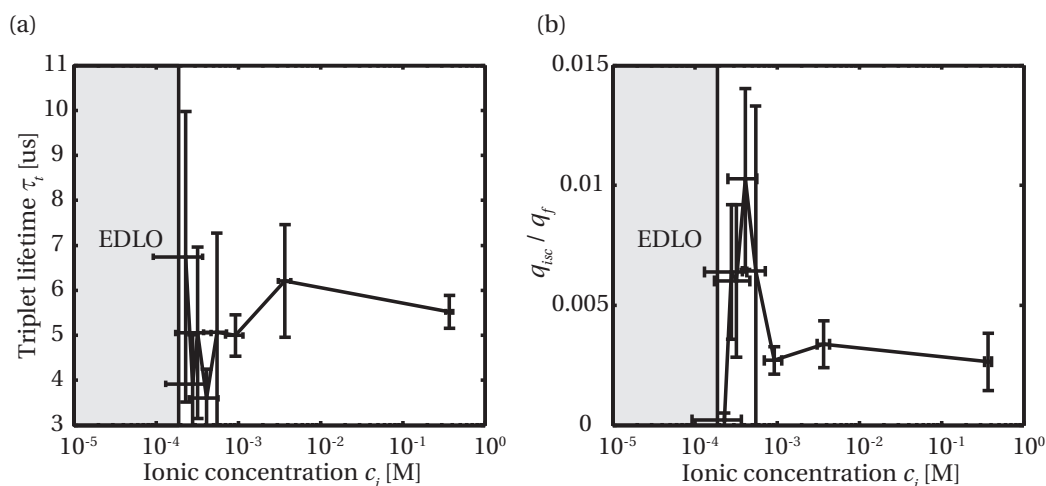


Figure 3.14: (a) Triplet state lifetime is weakly dependent on the ionic concentration and presents a lifetime approaching the one in bulk for the almost free diffusion around 0.4 mM. (b) Dividing the excitation normalized triplet population by the triplet lifetime yields the ratio q_{isc}/q_f .

The triplet state lifetime is extracted according to (3.11). The estimation of the lifetime τ_t is critical because of the poor time resolution and the uncertainty introduced by the afterpulsing removal (see Fig. 3.14 (a)). In contrast to the triplet state population, the triplet lifetime seems to be quite constant around 5-6 μ s with a possible minimum around 0.4 mM approaching 4 μ s. For very low ionic concentrations ($c_i \approx 230 \mu$ M.), the measurement of the triplet lifetime shows a low accuracy (Fig. 3.13 (a)). This is probably due to the low fluorescence signal linked to the molecular exclusion from the nanochannel and the low ionic concentration. The triplet state lifetime in bulk was measured to be independent of the ionic concentration and is about 4-5 μ s, which is comparable to values found in literature [53, 76]. Since the triplet lifetime is rather constant, a strong variation in function of the ionic concentration is found for the ratio $q_{isc}/q_f = \tau_f/\tau_{isc}$ (see Fig. 3.14 (b)). This ratio shows low values for ionic concentrations corresponding to strong surface interaction and high values in the case of almost free diffusion. These data present a strong uncertainty, though, and are shown for completeness only.

We have observed an increased triplet state population and a slightly reduced lifetime for ionic concentrations with the fewest surface interactions according to the slow diffusion and the anomalous diffusion parameter. The triplet state lifetime in the nanochannel is longer compared to bulk measurements. A similar effect has also been observed by Blom et al. [10]: If more cationic Rhodamine Green molecules are attracted to the glass surface, the triplet state lifetime is increased. Longer lifetimes are generated in viscous solvents [133] or solid matrices³. Since the molecules sticking on the glass surface are at the edge of the solid matrix,

³Phosphorescence for example is seen above all in solid matrices, if the non radiative triplet decay rate is small compared to the forbidden radiative decay rate. This is the case if there are fewer or no collisions with solvents.

and collisions are only on one side, the triplet state lifetime could be increased explaining the observed phenomena.

The opposed dependency of triplet population demands a closer look at the ratio $q_{isc}/q_f = \tau_f/\tau_{isc}$. In the case of enhanced surface interactions in the nanochannel, we concluded that q_{isc} should be increased and/or q_f reduced. The latter one can be explained: the higher index medium glass increases the local density of states at the surface and thus the emission channels [50]. Consequently, the fluorescent decay rate increases by about 10% at the surface of the nanochannel [82] as expected already earlier in this chapter. We did not notice a similar increase of the triplet decay, which was observed by Stefani et al. [117]. This is because in solutions, as in our case, the decay is highly non radiative at room temperature and only the small fraction of the radiative decay pathway is influenced and increased [9, 123].

The triplet state properties are also influenced by the heavy atom effect. As part of the fluorescent molecule or of the surrounding medium, atoms with high Z value enhance the spin-orbital coupling contributing to an increased intersystem crossing rate. In the case of non-ionic solvents, the intersystem crossing q_{isc} rather than the triplet relaxation is influenced [14]. The amplitude of this effect is proportional to Z^4 [123]. Since we have rather light elements in our sample, this effect is negligible for the used ionic concentrations of KCl.

The strong observed dependency of τ_f/τ_{isc} is not completely explained, but not further investigated due to the low measurement accuracy.

3.5 Conclusion

In contrast to free unconfined diffusion in bulk, we observed the influence of the ionic concentration on the diffusion of proteins in a nanochannel engraved in glass. Thanks to the EDL formed on the negatively charged glass surfaces and around the negatively charged molecules, the surface interactions are regulated. For an ionic concentration of about 0.4 mM, the fastest diffusion and the lowest surface interaction are observed. Under this condition, the thickness of the EDL is about 15 nm or roughly a third of the nanochannel height. Considering that also the negatively charged proteins feature a smaller spherical EDL around them, this corresponds in the ideal case to a configuration of a monomolecular diffusing layer surrounded by EDLs and the nanochannel walls. Within the measurement accuracy, this physical model has been corroborated with two FCS diffusion models and the interpretation of the photo-physical properties of the fluorescent molecules in the context of surface interactions. The measurement accuracy was limited by the accuracy of the protein and ion concentrations accuracy, fabrication variations of the nanochannel and the setup alignment.

The conclusion for nanofluidic devices is that the pH and the ionic concentration of the solution has a strong influence on the surface interactions and thus on the diffusion or transport of biomolecules. The EDL gives an accurate model on the scale of those interactions.

4 Stochastic Optical Reconstruction Microscopy

4.1 Introduction

An optical system has a certain bandwidth of spatial frequencies, which the optics can transmit from the object to the image. A similarity of super-resolution techniques is that additional higher frequencies have to be transmitted separately over other channels, in the most cases sequentially in time. In localization microscopy such as STORM or PALM this is achieved with thousands of sequential image frames, each one containing a part of the image information. In these methods as well as in SOFI described in Chapter 5, it is taken into account that the fluorescent molecules are *stochastically and independently* blinking light emitters. Assuming a given image formation model and an isolated single point emitter, its position can be estimated with nanometer accuracy from its blurred image. The localization of single molecules is successful as long as their PSFs do not overlap. At higher emitter densities they can still be localized provided that only a resolvable subset is emitting whereas the rest remains dark or is already irreversibly bleached. Recording many image frames and summing up the localizations of various subsets of emitting molecules yield a pointillist image with superior resolution depending on the localization accuracy, the labeling densities and other factors (see Fig. 4.1). There are several methods how the molecules are activated and turned dark.

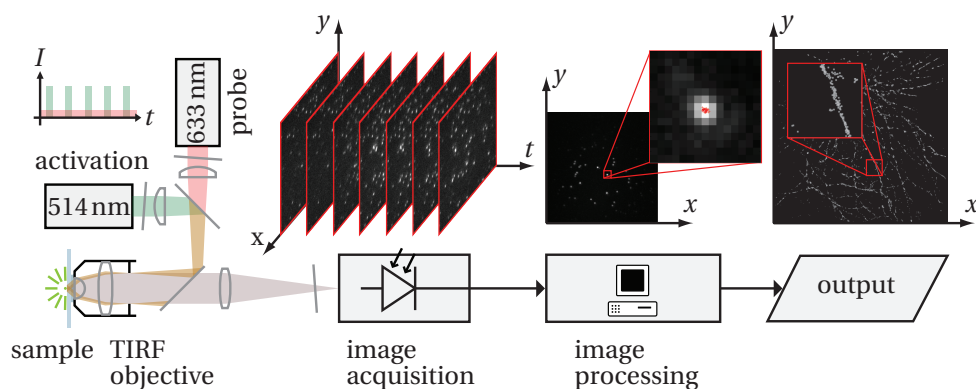


Figure 4.1: Schema of the image acquisition and the processing for the STORM imaging.

The idea of localizing different sparse subsets of molecules over many image frames remains the same, though. In STORM an organic dye is reversibly switched between a bright and a dark state with the help of an activator dye [106]. The activation without additional activator dye is used in direct STORM (dSTORM) [44]. In PALM fluorescent proteins are either irreversibly or reversibly switched between a dark and bright state [54, 8]. GSDIM makes use of long-lived dark states or simply the triplet state. At a sufficiently high excitation intensity, most of the molecules are in the dark state and return spontaneously to the ground state where they are localized by a fluorescence burst before they return to the dark state [29]. Localization by this spontaneous blinking is sometimes also referred to as dSTORM or blink microscopy. Points accumulation for imaging in nanoscale topography (PAINT) is based on fluorescent bursts when freely diffusing molecules bind to the object to be imaged [113]. The dark state is provided by the diffusing molecules, which are in a weakly fluorescent or self-quenched [69] state.

Basically any of those techniques can be extended to a 3D localization provided that isolated emitters can be localized with a sufficient SNR. 3D localization is achieved with PSF engineering [63, 62, 102, 119], interferometric approaches [115, 88], multiplane imaging [16, 68] or 3D PSF fitting [2, 1].

However, the appropriate sampling of a 3D structure requires a higher labeling density than 2D imaging. In order to assure the correct localization of isolated emitters, the molecules need to have a very long dark state compared to the bright state. Already in 2D imaging, this appears to be challenging, unless the photochemistry is perfectly mastered. The right choice of the fluorescent molecule together with the imaging buffer is crucial, if it is not the most important point [51].

Besides a sufficient SNR and a required match of labeling density and photo-physical properties, the accuracy of localization microscopy relies on the specific attachment of the photo-switchable fluorescent molecule to the structure of interest. This has commonly been achieved either by expressing fluorescent proteins (PALM) or by immunostaining (STORM). In the latter method, an organic dye is chemically bound to an antibody, which targets the structure of interest [61, 63, 106]. While fluorescent proteins permit the precise labeling even of living cells, immunostaining is more appropriate for non-living or fixed cells and enables the use of organic dyes emitting about ten times more photons before bleaching [61, 52]. However, antibodies are large proteins. Although the brightness allows to localize the dyes with higher precision, the localization accuracy of the target molecule is limited by the separation distance (10–20 nm) to the localized organic dye given by the size of the antibody [100]. SNAP-tag combines the advantages of the two labeling techniques by using self-labeling proteins to introduce almost any suitable organic dye [98]. The precise labeling with bright photoswitchable dyes is the ideal combination for super-resolution imaging, which is demonstrated by the recent application for the stimulated emission depletion (STED) approach [45]. It has previously been demonstrated that SNAP-tag fusion proteins can be labeled with a wide variety of different benzylguanine (BG) derivatives in cells [30, 66, 73, 75, 74].

Section 4.2 discusses the implication of the localization accuracy and of the labeling density on the achieved resolution enhancement in localization microscopy. After a detailed description of the origin of the switching and blinking behavior of Cy5 used in this study, the localization algorithm is presented. At the end of the theory part the issues of sample drift and image representation are addressed. Section 4.3 gives the experimental details about the preparation of the imaging buffer and the photoswitchable probe used in combination with SNAP-tag. The labeling was elaborated together with Sambashiva Banala and Gražvydas Lukinavičius. The optical setup and the algorithm used for imaging are specified thereafter. In Section 4.4 the achievement of 2D super-resolution imaging of microtubules in U2OS cells with STORM is presented. In addition to the reactivations on purpose, the strong spontaneous blinking was used similar to GSDIM. The use of SNAP-tag revealed a significant reduction of the marker–target distance (≈ 2.5 nm, and improved therefore the localization accuracy, which is detailed at the end of the section. The conclusion of this study is in Section 4.5.

4.2 Theory & Method

4.2.1 Resolution, localization and super-resolution

The resolution of an optical system is commonly related to the minimal distance at which the image of two adjacent points can still be distinguished. This is ambiguous and therefore various definitions exist. In microscopy the Rayleigh criterion is conventionally used and states that two points of equal intensity are resolved when the maximum of each of their Airy pattern is located on the minimum of the other. The resolution ρ then corresponds to the Airy radius $\rho = r_{\text{airy}} \approx 0.61\lambda/\text{NA}$ in the case of an aberration-free imaging. Other definitions are the Abbe limit¹ $\rho = \Lambda_{\text{min}} = 0.5\lambda/\text{NA}$ or the often used full-width at half-maximum $\rho = \text{FWHM} \approx \Lambda_{\text{min}}$ of the Gaussian fitted to the Airy pattern. The latter definition also works if the NA is not defined or the imaging is dominated by aberrations. These definitions of the resolution assume no background and do not take into account the SNR. However, it is important to note that the quality of a microscopy image depends not only on the resolution, but also on the contrast, and thus on the SNR. Chapter 5 provides more into details in this regard.

For about three decades the fact has been used that even though the image of a point like light source is blurred, its position can be determined with a better accuracy than the actual image resolution, provided the point source is well isolated [5, 12, 33]. Assuming the emission pattern (PSF) of the fluorescent molecules to be Gaussian (what is not exact, but a good approximation admitting freely rotating molecules, see Fig. 2.5 in Section 2.3.3), without noise and pixelation, it follows from statistics that the localization precision is simply $\Delta x = \sigma/\sqrt{N}$, where $\sigma \approx 0.2\lambda/\text{NA}$ is the standard deviation of the PSF and N the number of collected photons. This shows in general that the more photons are collected the preciser the localization is. A localization precision of about $\Delta x = 20$ nm can be achieved theoretically by collecting about

¹The Abbe limit corresponds to the spatial cut-off frequency of the optical transfer function of the system and can take into account the SNR.

20 photons only with $NA = 1.45$ and $\lambda = 633$ nm. Practically the PSF is larger due to defocus and other aberrations, and pixelation as well as background noise play an important role. Thompson et al. [120] derived an estimation of the localization precision Δx based on a Gaussian emission pattern taking into account the background, shot noise and the pixelation:

$$(\Delta x)^2 = \frac{\sigma^2 + a^2/12}{N} + \frac{8\pi\sigma^4 b^2}{a^2 N^2}, \quad (4.1)$$

where σ , a , N and b denote the standard deviation of the PSF, the effective pixel size in the object space, the number of collected photons and the uniform background noise (std) without shot noise of the localized molecule, respectively. As long as the ratio a/σ is small, Equation (4.1) is a good estimation. However, for large pixels ($a/\sigma \gg 1$), the localization precision tends to $\Delta x \approx a/\sqrt{12}$ since the molecule is detected only within one pixel and the localization is biased to the center. For small pixels the localization precision is reduced due to a lower SNR.

The optimal ratio of pixel and PSF size can be deduced from (4.1) yielding

$$a/\sigma = \left(\frac{96\pi b^2}{N} \right)^{\frac{1}{4}}. \quad (4.2)$$

For a typical background noise of 2–10 photons (Andor Luca S) and 100–1000 collected photons per molecule at 20 Hz this yields an effective pixel size which should be comparable or even slightly larger than the standard deviation of the PSF ($1 < a/\sigma < 5$) [120]. Using a pixel size of 100 nm, for example, a localization precision of around 20 nm can be reached with $N = 100$ and $b = 2$.

A more rigorous estimation of the localization precision is presented by Ober et al. [97] calculating the Cramér-Rao lower bound based on the Fisher information matrix. The localization precision is estimated not only for a Gaussian emission pattern but rather for an Airy pattern. The estimation shows a similar dependency on the parameters as the simple Gaussian approximation; however, it expects a higher accuracy limit, which can be reached with a maximum likelihood algorithm instead of the non-linear least square fit.

The localization of a single emitter is limited by several factors. As already seen, the ratio of background noise level to the number of collected photons per molecule has a direct influence on the localization precision. Dark molecules in the surrounding of the bright molecule to be localized are generally not completely dark, but contribute to a weak emission to the background. Together with other background sources like autofluorescence of the sample, this limits the localization precision. For a given excitation intensity, the limited number of emitted photons per molecule and time restricts the maximum acquisition frame rate. Furthermore, if the emitting molecule is not freely rotating, the dipole emission pattern may be asymmetric [1]. This can generate a bias of several nanometers on the estimated position. Moreover, the label may have a distance of some tens of nanometers of the labeled structure introducing another bias, particularly for the widely used immunostaining. This issue is addressed in

this chapter partly published in [17]. Finally also the labeling density limits the localization algorithm. If two bright emitters are too close, they cannot be localized or result in a false localization. This limitation is addressed in the next section.

4.2.2 Labeling density and its implication on the resolution

In localization microscopy the labeling density is a fundamental parameter. On the one hand a minimal surface density (in the case of 2D imaging) is required to resolve the structure. On the other hand, a too high density may introduce background by the dark emitters, or overlapping PSFs of molecules in the bright state. There is a surface density limit of bright molecules in the image plane above which their overlapping PSFs prevents their correct localization. The limit of the total labeling density depends additionally on the proportion r of dark and bright molecules. For current localization algorithms estimating one molecule position at once, the molecules have to be separated at least by approximately two Airy distances, i.e. $d = 2r_{airy} = 1.22\lambda/\text{NA}$. The maximum surface density of bright molecules can then roughly be approximated by $(\text{NA}/\lambda)^2$ depending on the used algorithm. Considering also the ratio r of dark to bright molecules, the maximum surface labeling density is

$$c_{max} \approx (r + 1) \left(\frac{\text{NA}}{\lambda} \right)^2. \quad (4.3)$$

At the same time, r should not exceed the ratio of bright to dark state intensity to ensure a sufficient signal to background ratio. For a detection with $\text{NA} = 1.45$ at $\lambda \approx 650 \text{ nm}$ and a ratio $r = 500$, the maximum labeling density is approximately $c_{max} \approx 2600 \mu\text{m}^{-2}$. This approximate estimation gives an idea of the orders of magnitude (see Fig. 4.2). By crossing this limit, the amount of false localization increases drastically or the localization is not possible at all (see also Chapter 5). In objects with fiber structures for instance, this may occur at the crossing of the fibers leading to a broadening of the intersection if the rate r is not sufficiently high [114, 126].

The number of required image frames to detect most of the molecules scales also with the ratio r and has to be at least as big as r . Due to the stochastic behavior in practice, the number of frames should rather be at least ten times bigger than r .

A low labeling density is less problematic for the localization. However, in localization microscopy the resolution is also limited by the sampling density. According to the Nyquist-Shannon sampling theorem, the Niquist limit of the resolution $\rho_{Nyquist}$ is given by the double of the average distance between neighboring labeled molecules [112]. For a 2D distribution of fluorescent molecules, for example under TIR excitation, the relation between resolution and labeling density is $\rho_{Nyquist} = 2 \text{SNR}_{\text{out}} / \sqrt{c_{mol}} > 2 \text{SNR}_{\text{out}} \lambda / (\text{NA} \sqrt{r + 1})$, where r is the ratio of dark to bright molecules and SNR_{out} is the desired SNR in the final STORM image [114]. The influence of the labeling density on the resolution is illustrated in Fig. 4.3.

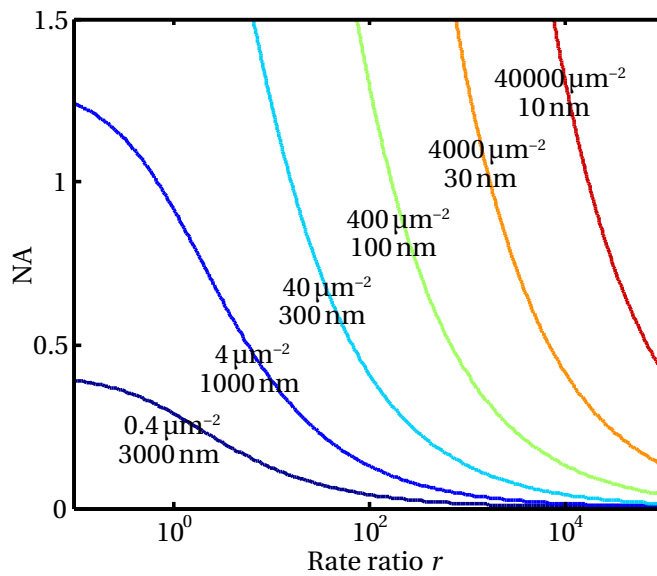


Figure 4.2: Maximal labeling density and resolution as a function of the numerical aperture and the rate ratio r for an emission wavelength $\lambda = 650$ nm. The upper quantity is the highest possible labeling density; the lower quantity is the highest achievable resolution according to the Nyquist-Shannon sampling theorem.

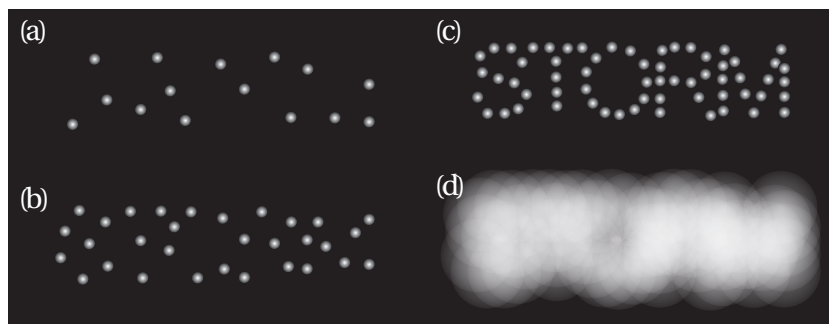


Figure 4.3: Illustration of the resolution limit due to the labeling density and localization accuracy. The 'S' of STORM is well resolved in (c) where the mean distance between the molecules is about half the smallest feature size of this letter. In (b) the labeling density is half and in (a) a fourth of the one of (c). Although the localization accuracy illustrated by the Gaussian is sufficient, the word STORM is not readable in (a) and (b). The labeling density in (d) is the same as in (c), the localization accuracy is not high enough, though.

An estimation of the effective resolution is given by the larger of either the Nyquist limit or the localization accuracy without considering false localizations, which potentially degrade the resolution additionally. The effective or convolved resolution (FWHM) is defined as [34, 67]

$$\rho \approx \sqrt{\rho_{Nyquist}^2 + (\Delta x_{FWHM})^2} \geq \sqrt{\frac{4\text{SNR}_{out}^2 \lambda^2}{\text{NA}^2(r+1)} + (2.35\Delta x)^2}$$

In the case of 20 nm localization precision (≈ 100 photons), the ratio of dark to bright molecules has to be at least $r > 300$ with a molecular density of about $1500 \mu\text{m}^{-2}$ to reach a resolution of around 70 nm (FWHM, $\text{SNR}_{out} = 1$). In addition the dark state needs to be at least 300 times weaker than the bright state. To achieve high resolutions, the fluorescent molecule should emit as many photons as possible in short pulses. This specifies high demands on the photo-physics and the chemistry of the fluorescent molecule.

4.2.3 Photoswitching and blinking of Cy5

For localization based super-resolution, such as STORM, the possibility to alternate between a dark and a bright emitter state is essential. The preceding sections revealed that about 100 photons have to be collected during the bright state, which has to be about 300 times shorter than the dark state.

Many fluorescent emitters feature a dark triplet state. In physiological solutions, the triplet lifetime of organic fluorescent molecules is in the order of microseconds, thus much too short for localization microscopy. By removal of oxygen, the triplet lifetime was reported to be increased up to 14 ms in the case of Cy5 [118]. In the bright state, however, the molecule emits only about 200–1000 photons (see Appendix B), less than about 100 of which can be detected. This is just too restrictive for an accurate localization, though. The blinking of Cy5 originating from its cis-trans isomerization has been investigated by Widengren et al [134]. This blinking has a characteristic time below $100 \mu\text{s}$ [42, 118, 107, 130] depending on the intramolecular mobility, which is influenced by the solvent viscosity [134]. This characteristic blinking time cannot be extended to the millisecond region, limiting the dark to bright state ratio r .

In certain imaging buffer conditions including an oxygen scavenging system to prevent fast bleaching and a reducing agent such as β -mercaptoethanol or other primary thiols, long-lived dark states have been observed with cyanine dyes, notably with a Cy3–Cy5 pair (Fig. 4.4) [6]. Some thousands of photons emitted by Cy5 can be detected before the dye falls to a long-lived dark state with a lifetime reaching up to an hour [42, 18]. The spontaneous reactivation of Cy5 occurs due to thermal energy [18]. In addition, the excitation of Cy3 close to Cy5 favors the reactivation. Alternatively, with a corresponding activation pulse of higher intensity, Cy5 or even other conventional fluorescent dyes can even be reactivated without any other fluorescent activator dye in proximity [44]. The origin of the long-lived dark state is not thought to be linked with the known cis-trans isomerization of Cy5 because it shows no dependency of the solvent viscosity. An ionic solution with increasing iodide concentration however shows

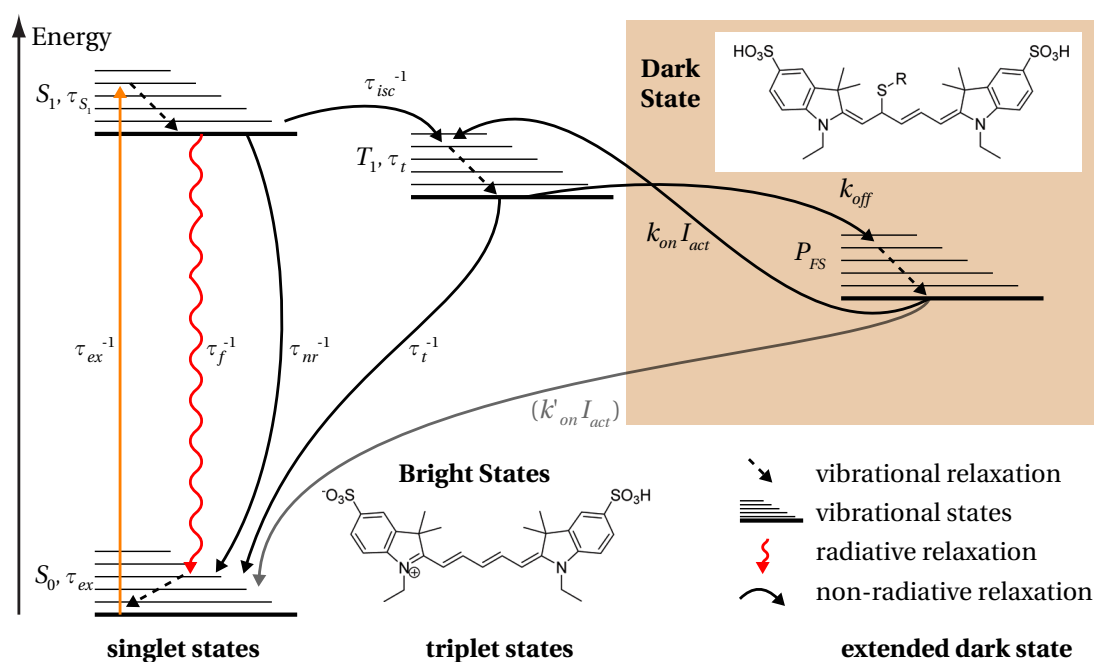


Figure 4.4: Extended Jablonsky diagram with a long-lived dark state originating from the reaction with thiol. The reactivation is possibly via the triplet state T_1 , but the direct fall back into the singlet ground state is not excluded. The vertical axis (ordinate) corresponds to the energy level.

a linear amplification of the switch-off rate indicating a triplet state mediated dark state (heavy atom effect). This explains the enhanced switching by the introduction of an oxygen scavenging system. The extremely long-lived dark states exclude a simple enhanced triplet state lifetime, but indicates the presence of a further dark state. Mass spectrometer analyses have shown that in the case of Cy5, Cy5.5, Cy7 and Alexa647 having a long polymethine bridge, the excited chromophore² reacts with the ionized primary thiol to form a non-fluorescent adduct (see inset in Fig. 4.4) [125, 18, 124]. Cy3 with a shorter polymethine bridge can not be switched in this manner. The carbocyanine dyes are reactivated possibly via the triplet state T_1 [42] by removing the thiol group from the chromophore. The binding energy originates from the absorption of a photon or the thermal energy. This process can be repeated about 100 times under ideal conditions [42] and is called photochromism. The ratio r of dark to bright molecules can be regulated by the reactivation laser intensity, but is limited by the spontaneous thermal reactivation. These long-lived dark states are a prerequisite for STORM imaging.

Another long-lived dark state is generated by ionization of the chromophore (see Fig. 4.5) [118]. This charge transfer at the level of the excited chromophore is initiated by a reducing or an oxidizing agent in the imaging buffer [129]. This process has been observed on most commonly used fluorescent dyes [128, 124]. The switch-off rate depends on the excitation intensity, the

²The chromophore is the fluorescent part of a molecule.

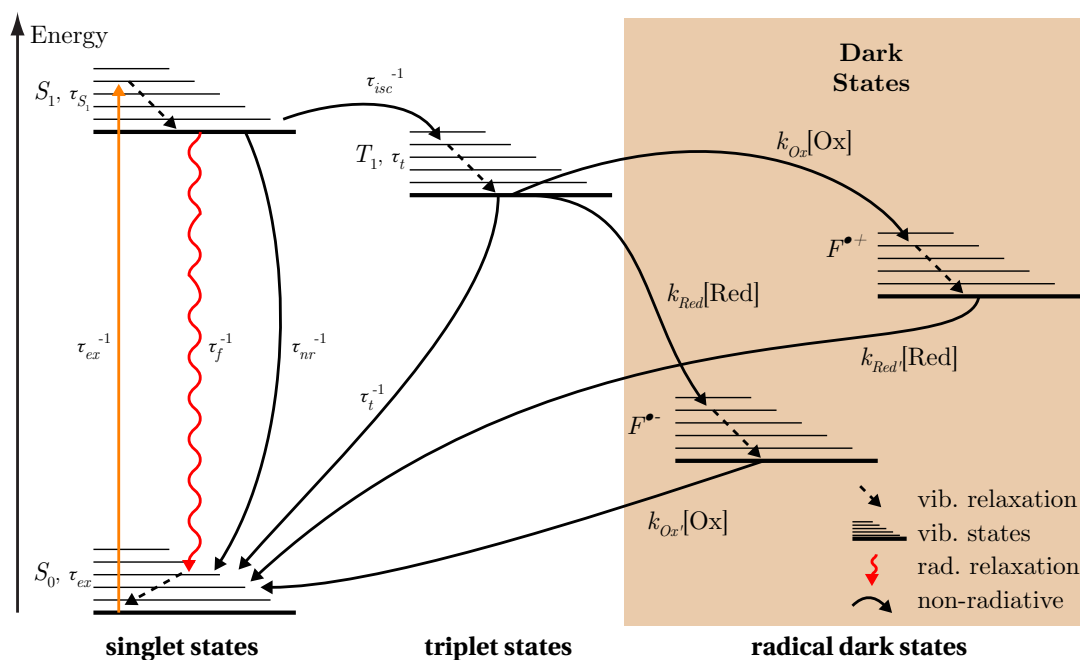


Figure 4.5: Extended Jablonsky diagram of the mechanism of ionization and triplet quenching via radical long-lived dark states. The vertical axis (ordinate) corresponds to the energy level. At higher mM concentrations of reducing or oxidizing agent, a direct electron separating pathway from the singlet state has to be considered (not shown here) [128].

concentration of the agent and the redox potentials of the reactants. The spontaneous return to the bright state is linked with the neutralization of the dye by a corresponding redox agent and can be enhanced by the excitation of the ionized molecule (often at shorter wavelengths). The switch-on rate is also related to the redox potentials and the concentration of the agents in the imaging buffer, but is independent of the excitation intensity. Since the ionization is most efficiently triggered by the chromophore's triplet state, which is quenched by oxygen, a reduced oxygen concentration achieved by a scavenging system is favorable. The rate constants k_{Red} , k_{Ox} , $k_{Red'}$ and $k_{Ox'}$ depend only on the redox potentials and can be estimated using Marcus theory and the Rehm-Weller equation [130]. For Cy5 the radical dark state lifetime is around 60 ms and has been used for dSTORM [118]. We assume that the strong spontaneous reactivation observed in our experiments are linked with the radical dark state.

Another interesting application of this mechanism is the possibility to increase the amount of emitted photons per molecule before bleaching. The oxygen concentration is reduced to weaken the bleaching. At the same time the triplet lifetime is enhanced due to the lack of the triplet quencher oxygen reducing the brightness of the dye. By introducing a reducing and oxidizing system (ROXS), the triplet state is efficiently quenched by charge transfer. For some fluorescent dyes (Cy3B, Cy5, Alexa647, ATTO647N), the number of emitted photons before bleaching can be enhanced by up to three orders of magnitude [130].

4.2.4 Localization algorithms

Once all requirements on the sample and the photo physics are satisfied, an image sequence with blinking or switching molecules can be recorded. Shot-noise, background noise and inhomogenous excitation are inevitably present in the images to be analyzed. Therefore, the images are filtered. Potential isolated molecules are identified by either a local maximum finding or a segmentation algorithm. The molecular positions are then estimated by the emission pattern using the center of gravity, a non-linear least square Gaussian fit or a maximum likelihood estimation assuming either a Gaussian or a more accurate image formation model (dipole emission). The corresponding algorithm is presented in Fig. 4.6.

On the one hand, the filtering has to block unwanted high frequency shot-noise on a pixel level and equalize the inhomogenous excitation. They both interfere with the determination of potential molecule positions. The use of a threshold needed for the segmentation is, for instance, only possible after equalization of the image field. On the other hand, the filter has to retain structures of the size of the emission pattern (PSF) corresponding to the molecules to be localized. A Laplacian of Gaussian filter satisfies the requirements of this bandpass filter and is implemented as a separated Gaussian filter ($\sigma \approx \text{std}(\text{PSF})$) followed by a Laplacian kernel approximation.

The starting points for the localization of potential molecule positions are given either by the local maxima above a certain threshold or by a segmentation algorithm applied to the filtered image. In the latter case, the segments defined by a threshold are selected according to their size and the corresponding amplitude in the original image. The center of gravity of those segments with respect to the original image presents a first estimation of the molecule position. In this approach, the segment properties (size and amplitude) allow to identify false positives. An additional fit to an assumed image formation model, for example a 2D Gaussian or a dipole emission pattern, gives a further approach to estimate the molecule position. The evaluation of the fit quality allows to exclude additional false positives. The fitting can be done for instance with a non-linear least square algorithm (i.e. Levenberg-Marquardt) or a maximum likelihood estimation. Assuming only Poissonian shot-noise it can be shown that the maximum likelihood estimation of the position reaches the Cramér-Rao lower bound which corresponds to the minimal theoretical localization uncertainty [97, 2]. If the emission pattern is a Gaussian, also the center of gravity is a maximum likelihood estimator of the molecule position [97].

4.2.5 Sample drift

During image acquisition a considerable sample drift can be observed. The reasons are manifold: temperature, air convection, mechanical deformation, building vibrations and so forth. Given an aluminum sample holder of 5 cm length, a tenth of a degree in temperature change would generate a sample drift of more than 100 nm. In addition, the piezo stage of the sample holder can introduce a sample drift. It is possible to solve this issue by a closed-loop

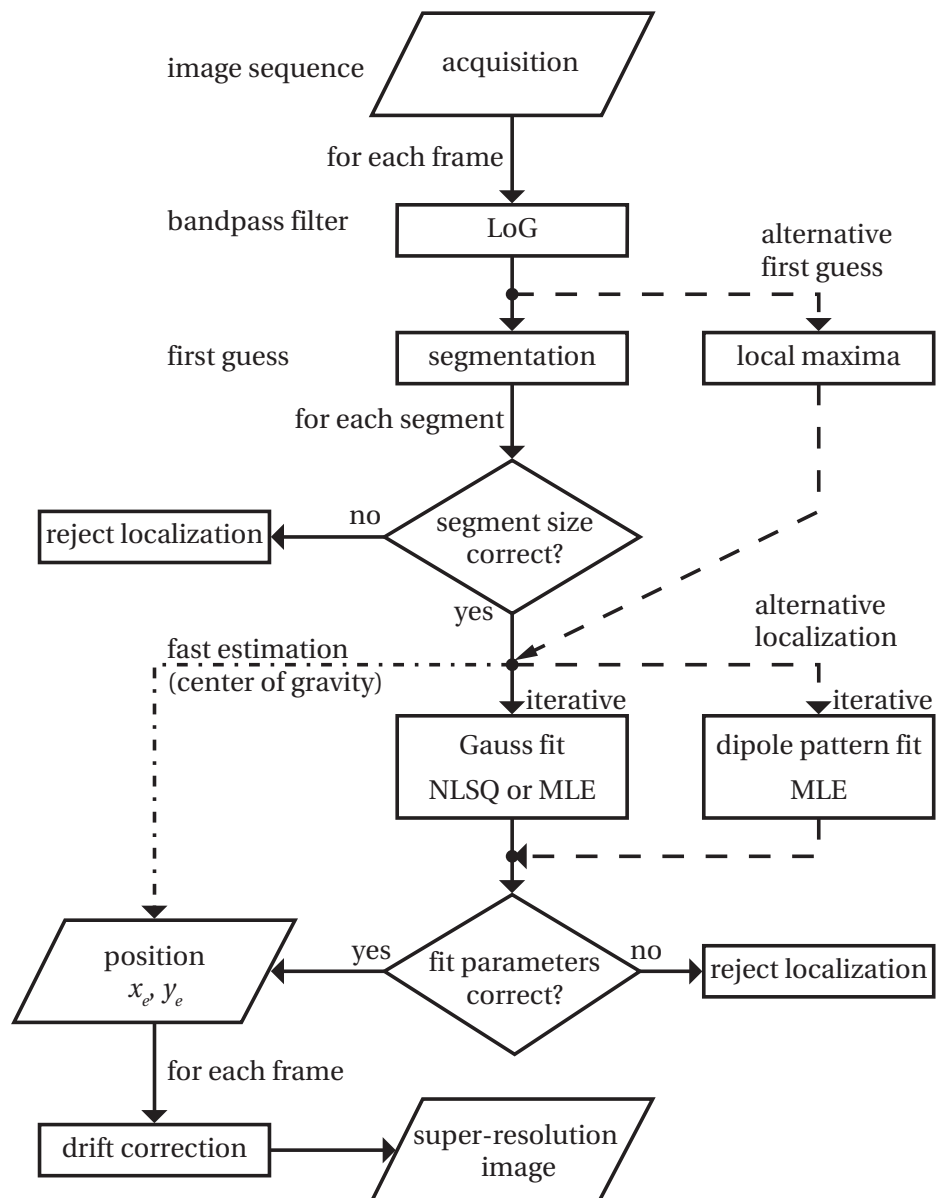


Figure 4.6: Flow chart of the localization algorithm. NLSQ: non-linear least square; MLE: maximum likelihood estimation.

control of the piezo stage with an interferometrically measured sample position feedback. If the sample drift is mainly lateral, it is often easier to correct the recorded image sequence for the sample drift than to avoid all possible causes.

During the measurements, we encountered a significant drift, most probably originating from the open-loop piezo stage. Since the drift was linear in time and mostly lateral, we opted for a linear drift correction during post-processing.

4.2.6 Image representation

The fluorescent molecules show a broad distribution of individual switching and blinking characteristics depending on their local environment. Some may stay in a bright state for many acquisition frames, others bleach very fast or are detected and localized in one frame only. Accordingly, the broad distribution of number of localizations per molecule can lead to a high dynamic range of the corresponding super-resolution image. A better visualization can be achieved by algorithms such as histogram equalization or Delaunay triangulation [3]. We have chosen a simple logarithmic scaling

$$I_{disp}(x, y) = \ln(L(x, y) + p), \quad (4.4)$$

where $L(x, y)$ are the number of localizations per sub-pixel, p an offset and $I_{disp}(x, y)$ the displayed intensity.

4.3 Experimental Details

4.3.1 Sample preparation

The fluorescent probe for the STORM measurements was synthesized by Gražvydas Lukinavičius and Sambashiva Banala in the laboratory of Kai Johnsson [65]. The probe contains Cy3 and Cy5 dye molecules as well as a BG moiety (see Figure 4.7). The BG permits the targeting of the Cy3–Cy5 photoswitch to SNAP-tag fusion proteins. The microtubules in U2OS cells were labeled by expressing β -tubulin as a C-terminal fusion of SNAP-tag (β -tubulin-SNAP, see Fig. 4.7). The fixed cells were incubated with the probe followed by a washing step. As a control, α -tubulin immunostaining of the cells was performed in parallel. Confocal fluorescence imaging has proven the colocalization of the signals from the immunostaining of α -tubulin and the SNAP-tag label demonstrating the highly specific labeling of β -tubulin-SNAP with Cy3–Cy5 (see Fig. 4.8). It should also be noted that SNAP-tag remains active and can be labeled after methanol fixation whereas green fluorescent protein (GFP) is known to lose fluorescence under similar conditions [38].

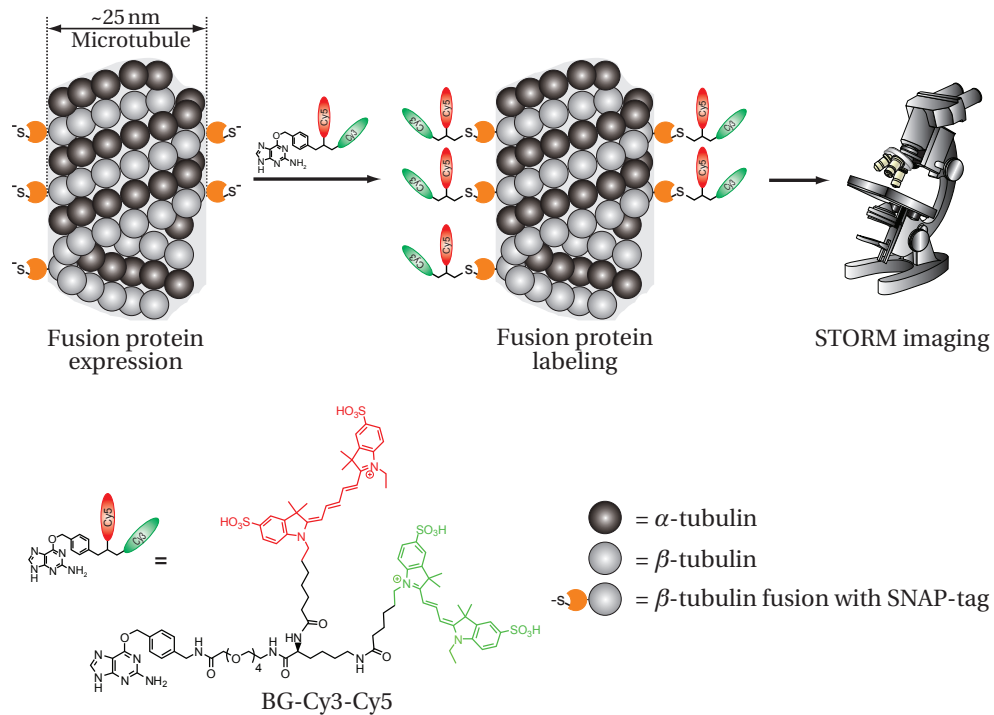


Figure 4.7: Illustration of the BG–Cy3–Cy5 labeling of α - and β -tubulin.

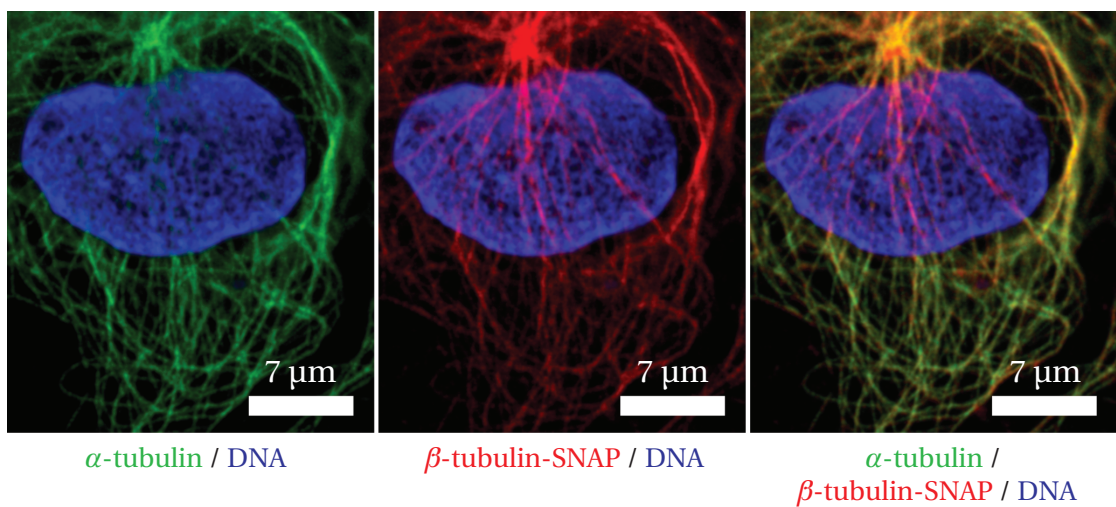


Figure 4.8: Confocal fluorescence images of cells expressing β -tubulin-SNAP fusion protein. Overlapping of the fluorescence resulting from the chemical labeling and immunostaining indicates the correct localization of β -tubulin-SNAP to the microtubules and demonstrates the specificity of the approach. Cellular α -tubulin was stained using mouse anti α -tubulin and Alexa 488 labeled anti-mouse IgG antibody (green). Transiently expressed β -tubulin-SNAP fusion protein was labeled with the SNAP-tag substrate BG–Cy3–Cy5 (red). Nuclear DNA staining with Hoechst 33342 was used as a reference (blue). Cells were fixed with methanol prior to staining. Images taken by Gražvydas Lukinavičius.

4.3.2 Imaging buffers

Prior to imaging, the samples were embedded in an imaging buffer similar to previous works [7]. The buffer was based on 50 HEPES pH 7.4 with 50 mM NaCl and contained 1% (v/v) β -mercaptoethanol and an oxygen scavenging system. The oxygen scavenger was composed of 0.5 mg/ml glucose oxidase, 40 μ g/ml catalase and 10% (w/v) glucose. A thin glass coverslip with the sample was placed on a second glass slide with a drop of imaging buffer and sealed with nail polish.

4.3.3 Optical setup

STORM measurements were performed on a custom-designed inverted TIR fluorescence microscope in epi illumination (Fig. 4.9). The objective was an Olympus 60x1.49oil with oil immersion used with an 300 mm tube lens to yield a 100x magnification. The two laser excitation sources were a red HeNe laser (633 nm, 2.5 mW) for imaging and a green Argon laser

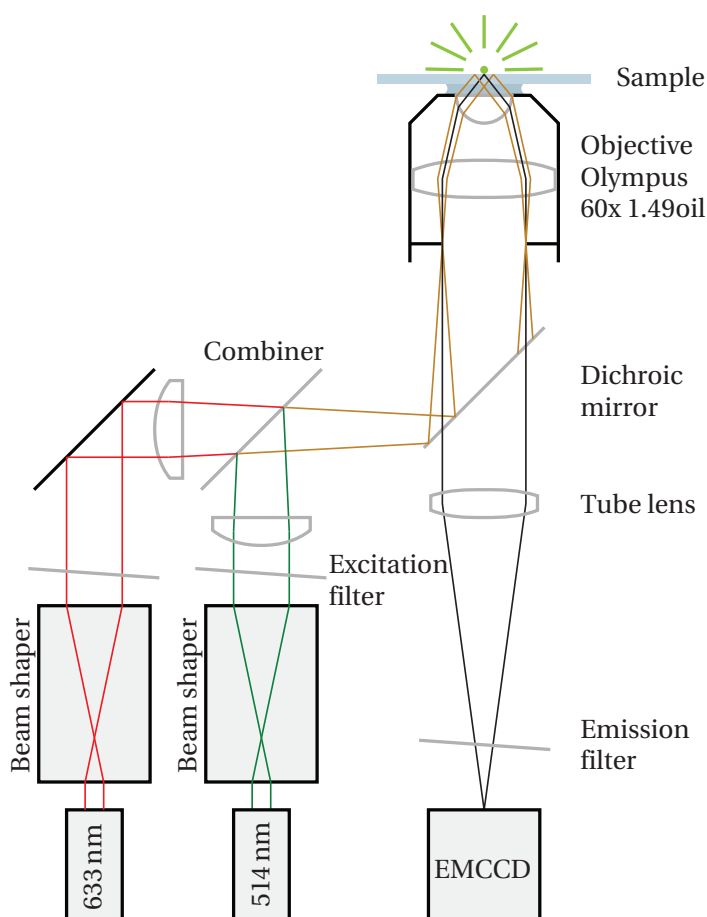


Figure 4.9: Inverted microscope in TIRF configuration used for STORM imaging.

(514 nm, attenuated to 200 μ W, 50 ms pulses every second) for activating the photoswitchable probes (see Fig. 4.1). The illumination area (beam waist)³ was approximately 430 μ m².

4.3.4 Image acquisition and processing

For the STORM image reconstruction, we acquired typically 5000 images at a frame rate of 20 Hz with a Luca S 658 camera from Andor. The electron multiplier gain was set to 100 \times .

The image processing executed frame by frame is driven by a dedicated Matlab platform. The first step involved selecting and isolating spatially resolvable labeled molecules with sufficient intensity. To this end, we applied a Laplacian of Gaussian filter ($\sigma = 2.1$ pixel) in order to enhance the SNR of these single emission patterns and to suppress noise. In the following step, image segmentation with an adaptable threshold was performed. Only segments with a size between 5 and 10 pixels were taken into account. The centre of gravity of the corresponding pixel values in the original image yields a first estimation of the emitter position. An improved accuracy was achieved by a Gaussian fit to the observed diffraction patterns using a non-linear least square algorithm (Levenberg-Marquardt). Outliers with a Gaussian waist larger than 0.5 μ m or an amplitude smaller than 100 or higher than 1000 were rejected. The super-resolution image has a pixel matrix 10 times finer than the original acquired image. The pixel values correspond to the number of localized fluorescent molecules within the enhanced pixel space and are represented in a logarithmic scale. After single molecule localization the reconstructed images were filtered using an image processing freeware to remove the non-structured background without any significant loss of information. Isolated localizations have been removed with the function "remove outliers" of radius 0 and threshold 1 using the freeware "ImageJ".

4.4 Results & Discussion

The imaging buffer used for STORM imaging has been tested for the photoswitching capability of pure BG-Cy3-Cy5 fixed with streptavidin and biotinylated BSA on a glass cover slide (see Fig. 4.10). In agreement with the theory, the addition of a primary thiol to the imaging buffer (HEPES, Tris or PBS) is necessary for the photoswitching mechanism. Other reducing agents such as Trolox⁴ or propyl gallate did not show the same switching efficiency as the primary thiols β -mercaptoethanol (2ME) or β -mercaptoethylamine (MEA). Furthermore, it turned out that the oxygen removal as well as a sufficient sealing is required for the efficient switching of the fluorescent probe. The oxygen scavenger has to be prepared less than one hour before the measurement to avoid degradation manifested by a pronounced reduction of the pH in the buffer solution. A reduction of the pH below 7 prevents the switching mechanism and has

³Without further consequences on the conclusion of the published data [17], this value was corrected after remeasuring.

⁴Trolox stands for 6-hydroxy-2,5,7,8-tetramethylchroman-2-carboxylic acid and is Hoffman-LaRoche's trade name. It is a water-soluble derivative of vitamin E.

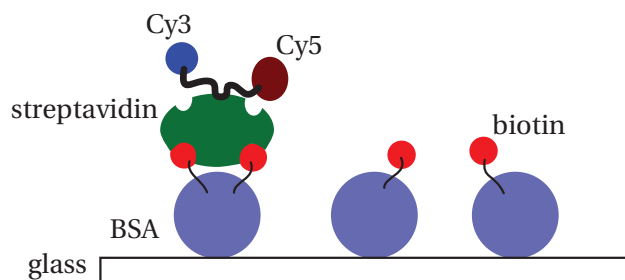


Figure 4.10: Fixation of fluorescent probes on a glass surface.

the effect that some components of the imaging buffer appear to be weakly fluorescent. The reduction of the pH can be explained by formation of gluconic acid [57].

During STORM measurements the center of gravity algorithm was used to produce a fast super-resolution image. Since this algorithm is iteration free, it is extremely fast. However it introduces numerous false localizations because their rejection is only based on the segment properties. Nevertheless, this approach is very convenient to get a rapid impression about the quality of the sample labeling and the photo-physical properties. Once a meaningful image sequence is selected, a non-linear least square Gaussian fit estimates the molecule positions. This iterative algorithm is much slower than the center of gravity, but allows to reject more false localizations with misshaped patterns. The localization accuracy could further be refined by using a physical image formation model instead of a Gaussian as a fit function. In the case of fixed fluorescent molecules for instance, a dipole emission model would be more appropriate and would avoid biased centroid localizations.

Originally, intentionally activated molecules were supposed to be localized after an activation pulse only. Their identification and distinction from spontaneously activated molecules, however, is complicated due to a strong spontaneous activation rate. For that reason, the localization algorithm was performed on all sufficiently isolated single molecules, independent of the green activation pulse. Subsequently, the dose of the activation pulse served to tune the density of the activated molecules (see Fig. 4.14 (a)). The strong spontaneous reactivation could be linked to the ionized dark states with shorter lifetimes (see Section 4.2.3).

The sample drift correction was applied after the localization algorithm. The possibility of post-correction is a strength of localization microscopy. The blue line in Figure 4.11 shows the trace of a photostable isolated molecule in a strongly drifting sample over 250 s. This trace suggests a nearly linear sample drift throughout the acquisition. Therefore, the sample drift was corrected by shifting all localizations linearly as a function of time, which strongly improved the resulting super-resolution image. To estimate the required correction shift, the super-resolution image of the first 500 frames was correlated to the super-resolution image generated from the last 500 frames (red line in Figure 4.11).

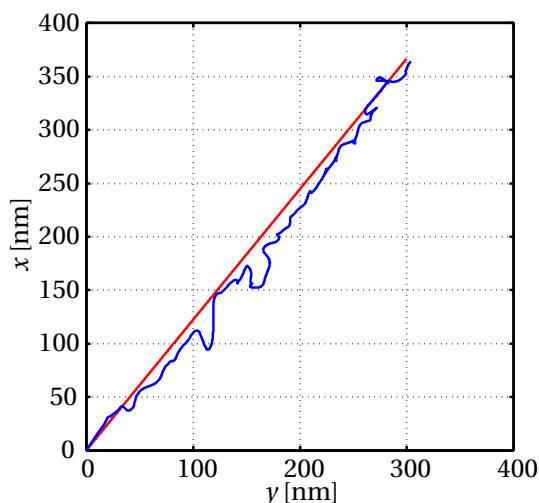


Figure 4.11: Sample drift measured by tracking a single molecule (blue line). Applied linear drift correction (red line).

Based on the SNAP-tag labeling technique, we performed super-resolution microscopy with STORM. The results presented in Figures 4.8 and 4.12 show the applicability of our new photoswitchable probes for the specific labeling of SNAP-tag fusion proteins in cells and the subsequent STORM-based super-resolution microscopy. The improvement due to STORM imaging becomes apparent by comparing microtubule structures imaged with a confocal microscope to the calculated STORM image. The width of the Gaussian fit to each of the cross sections in Figure 4.12 (e) and (f) demonstrates directly the improvement by almost an order of magnitude. This gives an idea of the image quality, although it does not directly correspond to the resolution, since STORM might fail for too high labeling densities due to two close structures for instance. Nevertheless, the cross sections reveal the reduced artificial increase of the observed labeled structures compared to conventional immunostaining [7, 100].

SNAP-tag reveals several advantages over commonly used immunostaining [61, 63, 106]. First, SNAP-tag is applicable to any structure of interest, without the need for a monoclonal antibodies with high specificity and affinity. Second, a precise labeling of the targeted protein is possible, with the potential to label living cells. Third, SNAP-tag is a small and highly soluble protein of 20 kD (≈ 2.5 nm); this results in a minimal artificial increase in size of the imaged structure [15, 44, 132]. Therefore, SNAP-tag is an ideal candidate for the construction of fusion proteins for super-resolution microscopy. The labeling is highly specific, fast, stoichiometric and quantitative. Furthermore, SNAP-tag labeling can be achieved after fixation of cells; this is a prerequisite for its compatibility with STORM.

The localization precision is measured by tracking an isolated single emitter that was in a bright state during almost the whole image acquisition. Since the spot disappeared and showed up in a single step, we assume that we deal with a single emitter. After linear drift

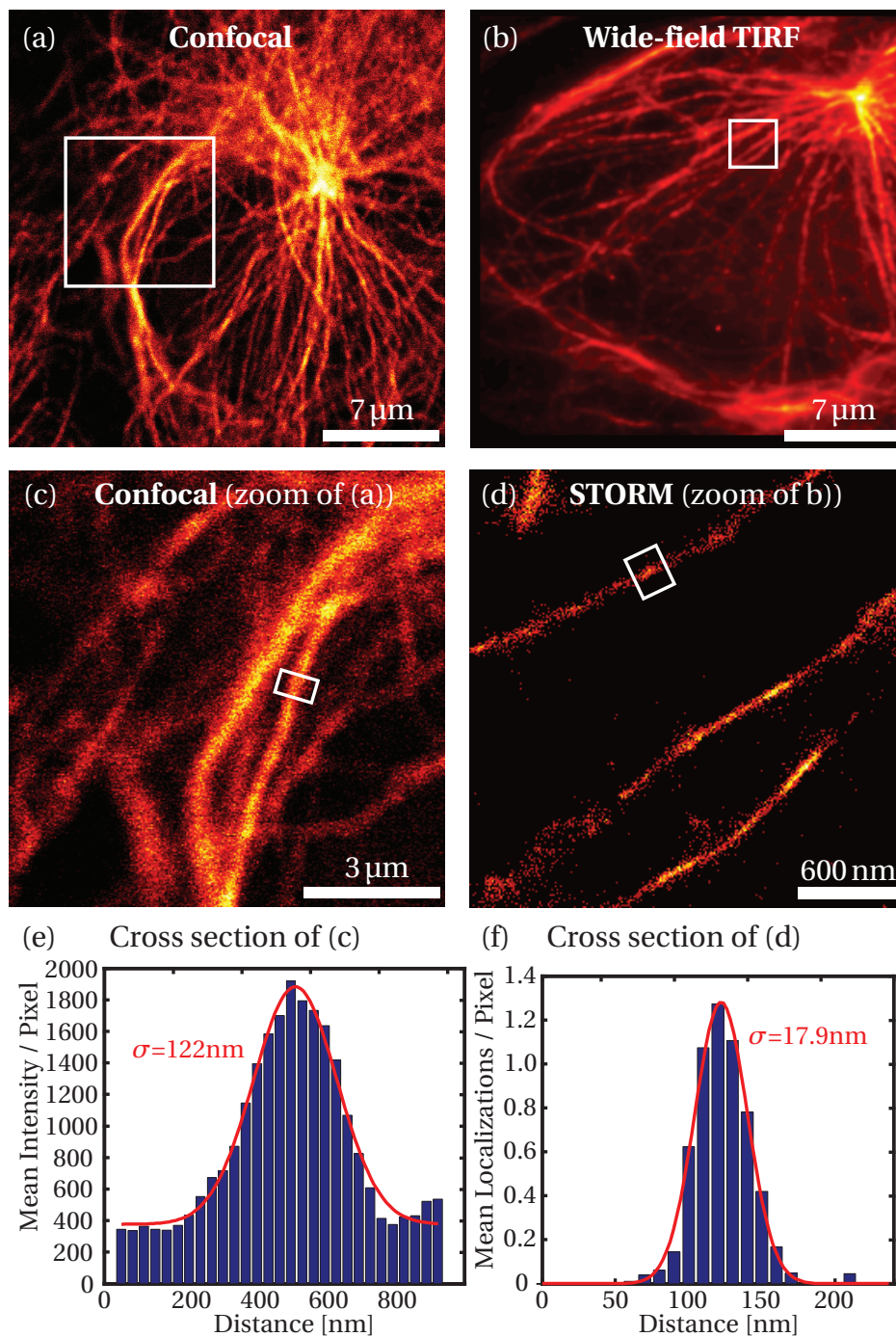


Figure 4.12: Confocal images (left side) and STORM images (lower right side). **(a)** confocal image of two U2OS cells (marker BG–Cy3–Cy5). **(b)** wide field image of a U2OS cell given by the sum of all frames of the STORM acquisition. **(c)** zoom-in to the white square in **(a)**. **(d)** STORM image of the white square in **(b)**. **(e)** transversal cross section of the tubuline structure in the white rectangle in **(c)** along with a Gaussian fit. The cross section is averaged over a 660nm large region along the structure. **(f)** transversal cross section of the tubuline structure in the white rectangle in **(d)** along with a Gaussian fit. The cross section is averaged over a 200nm large region along the structure.

correction, the standard deviation of the localizations is $\sigma = 11.3$ nm. Despite the incompletely compensated drift (see Fig. 4.11), this value is confirmed by evaluation of Equation (4.1) introducing the parameters for the single emitter summarized in Table 4.1. We find $\sigma \approx 7$ nm, which underestimates the measured uncertainty as expected by Thompson et al. [120].

quantity	description
$b \approx 10$ photon counts	background noise (std)
$a = 100$ nm	effective pixel size
$A \approx 340$ photon counts	average Gaussian amplitude of the isolated emitter
$s \approx 100$ nm	average Gaussian width of the isolated emitter (std)
$c \approx 2.5$	pixel–photon count conversion factor (see Section 2.3.4) ⁵
$N \approx 2\pi A(s/a)^2/c \approx 900$ ph.	number of collected photons per molecule
$\sigma \approx 7$ nm	estimated localization precision

Table 4.1: Statistic of the localization procedure. std stands for the standard deviation.

The background noise can be estimated for each localized emitter. The residual r of the Gaussian fit is the sum of the squared differences of the fit to the measured PSE. The residual consists of shot noise and local background noise b . The latter one can be estimated by subtracting the Poisson distributed shot noise corresponding to the measured photon counts N :

$$b = \sqrt{\frac{r/c^2 - N}{n}}, \quad (4.5)$$

where c is the pixel–photon count conversion factor and n is the number of pixels considered in the fitting. In the case of the isolated emitter, we find $b \approx 10$ photon counts, corresponding to the background noise measured on an empty area with no emitters.

These parameters and the corresponding localization precision reflect the ideal imaging conditions with high SNR. In general, these conditions are not found everywhere in the sample. The localization precision depends on the width and the amplitude of the PSE, which are degraded by defocus (Fig. 4.13 (a) and (b)). Moreover, in contrast to the isolated emitter, dark molecules that are not completely dark or the autofluorescence of the labeled structure introduce additional background noise (Fig. 4.13 (c)). This indicates an insufficient dark state or blinking rate (spontaneous reactivation) with respect to the labeling density. In consequence, this leads to a distribution of the localization precision within the sample (Fig. 4.13 (d)), which is degraded compared to the single emitter.

⁵Without further consequences on the conclusion of the published data [17], this value was corrected after revision of Section 2.3.4.

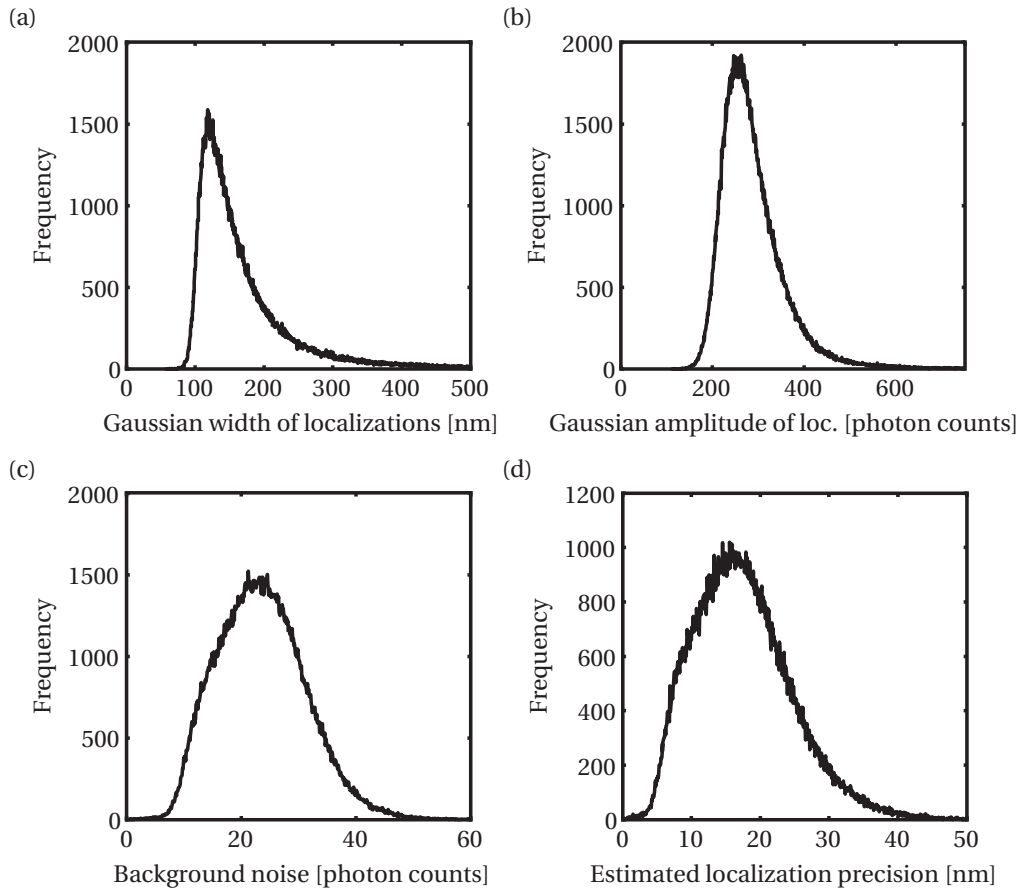


Figure 4.13: Distribution of (a) amplitude and (b) waist of the Gaussian fit. The localizations have a mean Gaussian amplitude of about $A = 250$ pixel counts and a mean waist of about $s = 120$ nm. (c) Subtracting the shot noise from the residual of the Gaussian fit yields the background noise at the considered location. (d) Estimated localization precision according to Equation (4.1) and the data in (a-c).

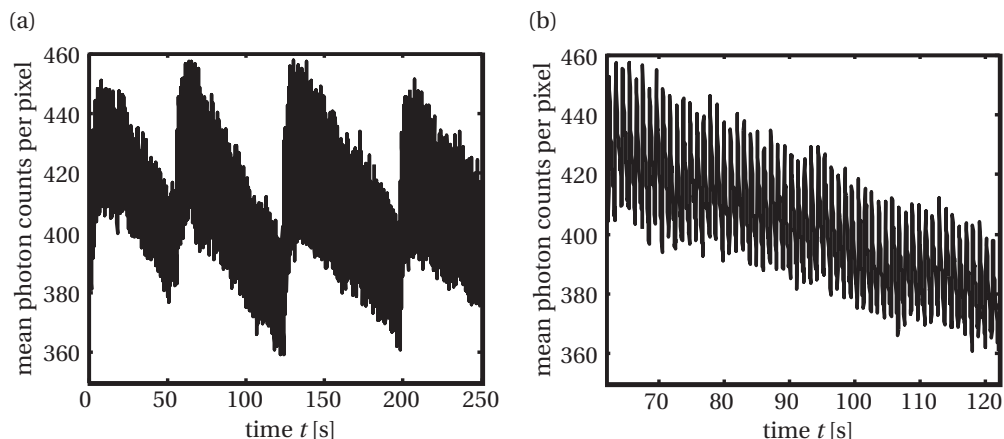


Figure 4.14: Mean photon counts per pixel. **(a)** Mean photon counts of the whole acquisition. In order to keep a more or less constant density of emitting molecules despite of bleaching, the activation laser intensity was increased three times. **(b)** Zoom in (a) showing the activation events and the bleaching.

According to Table 4.1 and Fig. 4.13, about 900 photons are detected in average per frame and molecule. The setup collection efficiency can be estimated thereof by considering the excitation intensity and the corresponding emission rate of Cy5 (see Appendix B). We find a detection efficiency of $\approx 6\%$ corresponding to the lower limit of the estimation in Section 2.3.2.

The proper functioning of the imaging buffer is shown by the reduced bleaching and the reactivation ability. Over 60 reactivation cycles, only 15% of the molecules are bleached (see Fig. 4.14 (b)) whereas without imaging buffer the majority of the molecules bleach (data not shown). Figure 4.14 (a) shows the mean intensity of the whole image sequence. In order to have a more or less constant density of reactivated molecules and thus an optimal localization performance, the activation laser power was increased three times to compensate for bleached molecules.

4.5 Conclusion

Microtubules visualized with β -tubulin-SNAP have been resolved well below the diffraction limit. The characteristic dimensions (FWHM) of these structures measured by this method are 40 ± 10 nm in diameter. This value is close to the theoretical value of 30 nm, which is obtained from a microtubule diameter of ≈ 25 nm, and an estimated distance of ≈ 2.5 nm from the N terminus of the SNAP-tag to its reactive cysteine residue (see Fig. 4.7). It is noteworthy that this measured size of the microtubule is smaller than that measured with STORM based on antibody staining (60 nm [7, 100]).

Chapter 4. Stochastic Optical Reconstruction Microscopy

To achieve STORM imaging, the right imaging buffer with oxygen scavenger, labeling density, excitation intensity and a sufficient sample sealing are crucial. Otherwise single emitters are not well isolated increasing the risk for mislocalization artifacts. Beyond that, the localization accuracy has to be interpreted carefully and should not be mistaken with the resolution. The labeling density was not estimated. Hence the resolution is not defined.

In summary, we have introduced a targeted photoswitchable probe for the labeling of SNAP-tag fusion proteins in cells and have successfully used them for STORM-based imaging. The small size of the SNAP-tag and the simplicity of its labeling with a large variety of fluorescent probes make this labeling technique well-suited for the imaging of biological structures. Furthermore, it should be straightforward to extend the approach described here to multicolor STORM or dSTORM [44], using different “orthogonal” self-labeling tags, such as the CLIP-tag [30]. For our experiments it should be noted, however, that the localized dye (Cy5) rather than the reactivating dye (Cy3) should be used as multicolor label, unless the strong spontaneous reactivation rates can be reduced. We believe that the described approach will significantly broaden the possibilities of performing super-resolution microscopy of biological structures.

5 Super-Resolution Optical Fluctuation Imaging

5.1 Introduction

It is a challenge to prepare a biological sample that fulfills all prerequisites for STORM imaging. A high SNR is needed to accurately localize single molecules and avoid false localizations. At the same time a high resolution is assured by a considerably high labeling density only. This demands that the fluorescent marker is ideally between 1000 to 10000 times longer in the dark state than in the bright state. A cell sample with filaments like microtubules can relax this condition by a lower overall labeling density. However, it remains a strong limitation, for example at intersections of microtubule fibers. If these requirements are not met in specific regions, false localizations cannot be excluded completely. Therefore the resulting super-resolved image is not free of artifacts.

SOFI benefits of the fact that single molecules blink independently. Similar to FCS, single molecules can be detected even with a reduced SNR. Thanks to the independency of different molecules, a single molecule correlates only with itself, but not with the others. The auto-correlation acts like a squaring of the measured signal. If the signal of an isolated emitter is squared, its PSF narrows. Squaring the signal of two closely located emitters is no solution to resolve them because of cross products. However, squaring each emitter independently improves the resolution (see Fig. 5.1). This is achieved by the correlation if the two emitters blink independently. Cumulants generalize this concept to higher orders (see Appendix A). Assuming the PSF to be approximately Gaussian, the n -th order cumulant increases the resolution \sqrt{n} -fold by using the fact of the independency of single molecules and without the use of delicate localizations.

Initially, SOFI consisted of computing higher-order auto-cumulants [19], where the achievable resolution was limited by the effective pixel size of the detector. Recently, it has been shown that this limitation can be circumvented using spatio-temporal cross-cumulants (XC-SOFI) for generating a finer sampling grid [20]. Furthermore, a simple reweighting scheme in the Fourier domain of the n -th order SOFI image has been introduced, which modifies the resulting SOFI PSF to yield the original microscope PSF with an n -fold reduced size, corresponding to a reso-

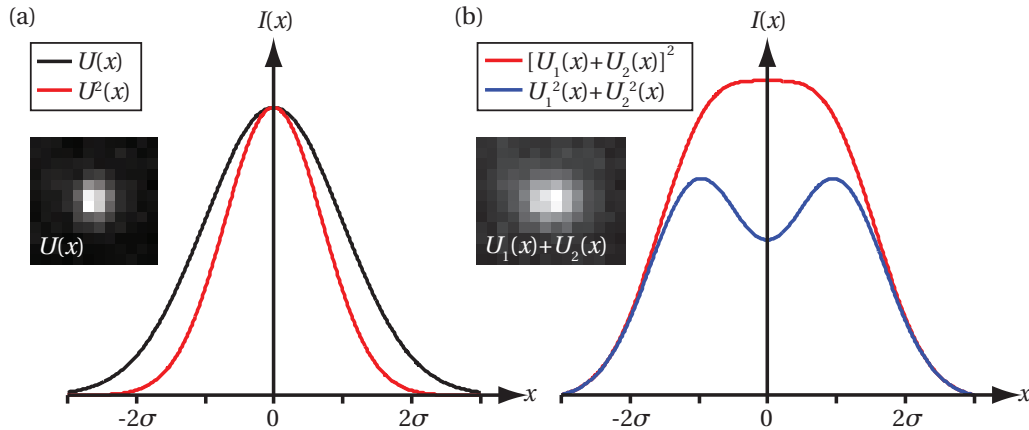


Figure 5.1: Resolution improvement by squaring the PSF. For illustration, the PSF is approximated with the Gaussian: $U(x) = \exp(-x^2/(2\sigma))$ and $U_{1,2}(x) = U(x \pm \sigma)$. **(a)** The Gaussian is narrowed by $\sqrt{2}$ by squaring its intensity. **(b)** Two spots separated by 2σ are resolved only if their Gaussian is individually squared.

lution improvement by a factor of n [20]. Here we implemented those recent developments, calculated spatio-temporal cross-cumulants to generate inter-pixels and estimated the PSF, which is necessary for the subsequent Fourier reweighting (FRW).

A scheme illustrating the different steps of the SOFI algorithm is depicted in Fig. 5.2. The computation of different combinations of spatio-temporal cross-cumulants of each pixel with $n - 1$ of its neighboring pixels enables the construction of an n -fold finer sampling grid in the final image (see Fig. 5.3). Due to the spatial decrease of correlation, the inter-pixels introduced by cross-cumulants are lower in amplitude than the pixels computed by the auto-cumulants and need thus to be corrected by a distance factor (Fig. 5.2, step 3). Using an image formation model (e.g., Gaussian) of the microscope's PSF and varying its parameters, these correction factors can be iteratively optimized until all pixels have similar weights. The resulting estimation of the PSF is used in the Fourier reweighting (Fig. 5.2, step 4).

The computed cumulants contain more information than the super-resolution. Cumulants depend on the blinking characteristics of the observed molecules. By comparing several cumulant orders, parameters such as molecular brightness, density and blink statistics can be extracted simultaneously with an increased resolution and contrast. Applied to biological investigations this cumulant imaging offers the possibility to monitor the microenvironment of a fluorescent molecule, the blink statistics of which is influenced by the concentrations of certain substances. This offers functional imaging similar to imaging FCS [70, 109], but combined with super-resolution capability. Furthermore, the evaluation of the blink statistics informs whether the considered sample region is well-suited for STORM imaging.

Section 5.2 describes the theoretical background of SOFI and cumulant imaging and explains the supplementary tools Fourier reweighting and cross-cumulants used to achieve a further

resolution enhancement and a finer virtual pixel sampling combined with an effective reduction of noise. The SNR provided by these methods is examined at the end of the theory part. Section 5.3 specifies the simulation framework and the experimental details. In Section 5.4 a characterization of SOFI is presented by comparing the performance of SOFI with localization based microscopy (STORM). SOFI turned out to be much less challenging with respect to the photo-physical properties of the sample. Also based on similar simulations, cumulant imaging is tested and characterized for its functional imaging capabilities to extract molecular brightness, density and blinking characteristics. Section 5.5 presents the application of SOFI and cumulant imaging to the measurements of microtubules in U2OS cells labeled with Cy3–Cy5 and SNAP-tag. SOFI and cumulant imaging are discussed in Section 5.6 leading to the conclusion in Section 5.7.

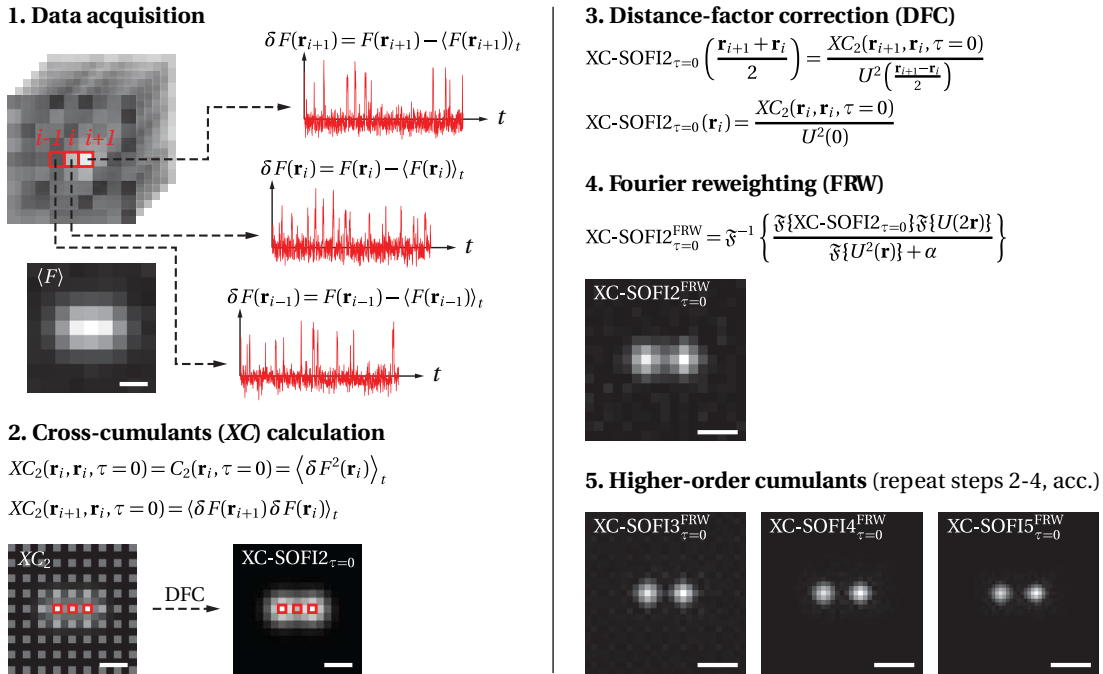


Figure 5.2: The different steps of calculating cross-cumulant SOFI with Fourier reweighting (XC-SOFI-FRW), illustrated for the second order. Before the computation of cross-cumulants, the mean is subtracted from the data **step 1**). Using different combinations of cross-cumulants between pixels gives rise to an inhomogeneous weight distribution (**step 2**), which needs to be corrected by a distance factor (**step 3**). The distance-factor correction also provides an estimation of the system's PSF. Fourier reweighting (FRW) enables the modification of the SOFI equivalent PSF to retrieve the microscope's PSF with an n -fold reduced size (**step 4**). Higher-order cumulants are computed using the exact formulation described in [90]. *Scale bars: 200 nm.*

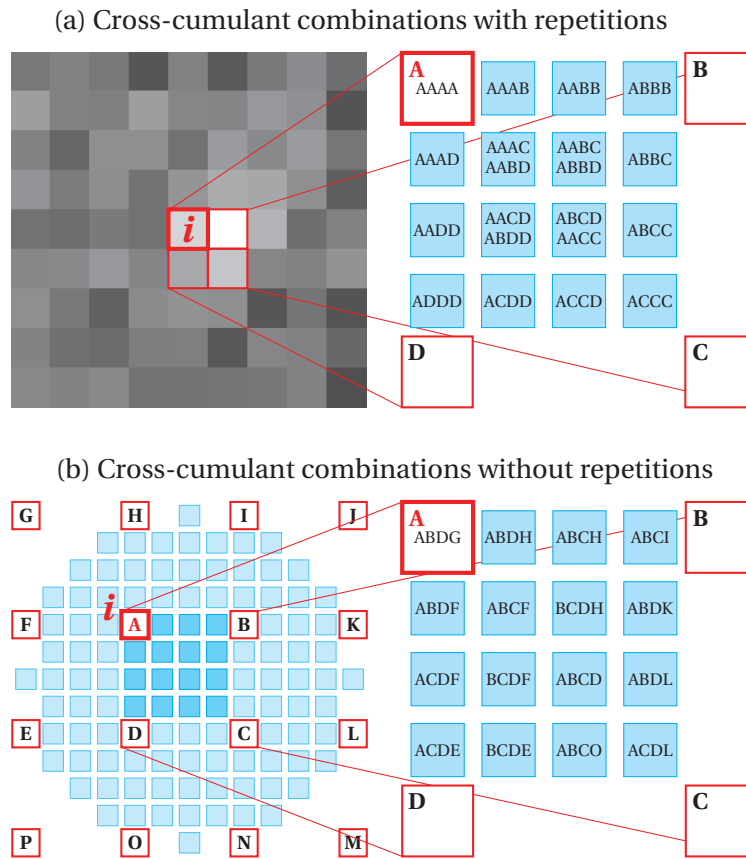


Figure 5.3: Fourth-order cross-cumulant combinations for pixel i with or without repetitions. Different combinations within a neighborhood matrix of i can be used to generate 15 inter-pixels in between the original pixel matrix (ABCD). Combinations leading to the same inter-pixel are averaged. **(a)** All n -combinations within a 2×2 neighborhood (ABCD) starting with A and allowing for repetitions are computed. This scheme can be expanded easily to any order n . Due to the presence of autocumulants, this method does not suppress shot noise very well unless non-zero time lags are used. **(b)** The different combinations within a 4×4 neighborhood of pixel i can be used to generate inter-pixels in a circular arrangement (left). By excluding repetitions (autocumulants), shot noise is suppressed much better. For computational reasons, only combinations featuring the shortest sum of distances with respect to their corresponding inter-pixels are considered. By considering more combinations and averaging over the corresponding cross-cumulants, even more noise could be eliminated. Further simplification can be done by considering only combinations leading to the 15 inter-pixels within ABCD (right). This scheme is expandable until order 10. To go beyond this range, the size of the neighborhood has to be increased.

5.2 Theory & Method

5.2.1 The principle of SOFI

We assume a fixed sample labeled with N independently fluctuating markers. Their position \mathbf{r}_k is fixed during acquisition and their temporal fluctuations are stationary. The principle of the following theory can be applied to any fluctuating signal and is not limited to fluorescence microscopy. In the following we consider the imaging of single fluorescent molecules, though. The image formation of an optical system is described by the convolution of the object $S(\mathbf{r})$ with the PSF $U(\mathbf{r})$

$$F(\mathbf{r}) = U(\mathbf{r}) * S(\mathbf{r}), \quad (5.1)$$

where $F(\mathbf{r})$ is the recorded image. For simplicity the PSF is assumed to be constant over the whole field of view. The object $S(\mathbf{r})$ consists of N single point emitters at the position \mathbf{r}_k with detected intensity A_k and temporal fluctuations $s_k(t) \in [0, 1]$:

$$S(\mathbf{r}, t) = \sum_{k=1}^N A_k \delta(\mathbf{r} - \mathbf{r}_k) s_k(t), \quad (5.2)$$

where the Dirac $\delta(\mathbf{r} - \mathbf{r}_k)$ describes the position \mathbf{r}_k of the molecule. An image sequence $F(\mathbf{r}, t)$ can be represented as

$$F(\mathbf{r}, t) = \sum_{k=1}^N A_k U(\mathbf{r} - \mathbf{r}_k) s_k(t) + b(\mathbf{r}), \quad (5.3)$$

where $b(\mathbf{r})$ is a temporally constant background intensity coming from the sample or the image acquisition. As expected, there is no resolution improvement, if the whole image is squared as illustrated in Fig. 5.1 b). This is because in addition to the individually squared PSFs, all cross products are involved. This can be avoided by time-correlating the image sequence with itself instead of squaring. Assuming stochastically and independently blinking molecules, each emitter correlates only with itself. For a stationary blinking signal, i.e. no bleaching, the cross-correlation of the temporal zero-mean fluctuations $\delta s_k(t) = s_k(t) - \langle s_k(t) \rangle_t$ of two independent emitters tends to zero for sufficiently long sequences ($N_f > 1000$ frames), while it persists in the case of the autocorrelation:

$$\lim_{N_f \rightarrow \infty} \langle s_j(t) s_k(t) \rangle_t = \begin{cases} 0 & \text{if } j \neq k \\ g_{2,k}(\tau) \neq 0 & \text{if } j = k \end{cases} \quad (5.4)$$

The autocorrelation of the corresponding zero-mean image sequence $\delta F(\mathbf{r}, t) = F(\mathbf{r}, t) - \langle F(\mathbf{r}, t) \rangle_t$ is then given by:

$$\begin{aligned}
 G_2(\mathbf{r}, \tau) &= \langle \delta F(\mathbf{r}, t + \tau) \cdot \delta F(\mathbf{r}, t) \rangle_t \\
 &= \sum_{j=1}^N \sum_{k=1}^N A_j A_k U(\mathbf{r} - \mathbf{r}_j) U(\mathbf{r} - \mathbf{r}_k) \langle \delta s_j(t + \tau) \cdot \delta s_k(t) \rangle_t \\
 &= \sum_{k=1}^N A_k^2 U^2(\mathbf{r} - \mathbf{r}_k) \underbrace{\langle \delta s_k(t + \tau) \cdot \delta s_k(t) \rangle_t}_{g_{2,k}(\tau)}.
 \end{aligned} \tag{5.5}$$

The temporally constant background $b(\mathbf{r})$ vanishes in the zero-mean image sequence. For a given delay time τ , the created image is composed of the squared PSFs $U^2(\mathbf{r} - \mathbf{r}_k)$ weighted by the squared intensity A_k^2 and the correlation factor $g_{2,k}(\tau)$. The time lag τ has to be chosen smaller than the characteristic blinking time to ensure the correlation. If the PSF is approximated with a 3D Gaussian (see Fig. 2.5 in Section 2.3.3), the square translates directly in a narrowed Gaussian in all three dimensions by a factor of $\sqrt{2}$ (see Fig. 5.1):

$$U^2(\mathbf{r}) = \exp\left(-2\frac{x^2 + y^2}{2\sigma_{xy}^2} - 2\frac{z^2}{2\sigma_z^2}\right) = \exp\left(-\frac{x^2 + y^2}{2\bar{\sigma}_{xy}^2} - \frac{z^2}{2\bar{\sigma}_z^2}\right), \tag{5.6}$$

with $\bar{\sigma}_{xy} = \sigma_{xy}/\sqrt{2}$ and $\bar{\sigma}_z = \sigma_z/\sqrt{2}$. Laterally and axially, this results in a resolution enhancement and axially it improves additionally the optical sectioning. The autocorrelation $G_2(\tau)$ is a second order moment. Higher order moments μ_n can be calculated, but are generally not additive for independent random variables X and Y at orders higher than three:

$$\mu_n(X + Y) \neq \mu_n(X) + \mu_n(Y) \quad \forall n > 3 \tag{5.7}$$

Consequently the moment of the sum of the blinking emitters (i.e. the moment of the image sequence) is not equal to the sum of the moments of the emitters (i.e. the super-resolution image). Thus, because of cross terms, the resolution improvement is limited. Per definition, cumulants are additive and do not contain those cross terms. Among others, cumulants κ have the following properties (see Appendix A):

1. If β and λ are constants and $\{X_i\}$ random variables, then

$$\kappa(\beta + \lambda X_1, \dots, \beta + \lambda X_n) = \lambda^n \kappa(X_1, \dots, X_n) \quad \forall n > 1. \tag{5.8}$$

2. If the random variables $\{X_i\}$ are independent of the random variables $\{Y_i\}$, then

$$\kappa(X_1 + Y_1, \dots, X_n + Y_n) = \kappa(X_1, \dots, X_n) + \kappa(Y_1, \dots, Y_n) \quad \forall n. \tag{5.9}$$

3. If any subset of $\{X_1, \dots, X_n\}$ consists of independent random variables, then

$$\kappa(X_1, \dots, X_n) = 0 \quad \forall n > 1. \quad (5.10)$$

We can therefore write the n -th order cumulant C_n as

$$\begin{aligned} C_n(\mathbf{r}, \tau_1, \dots, \tau_{n-1}) &= \kappa(\delta F(\mathbf{r}, t), \delta F(\mathbf{r}, t + \tau_1), \dots, \delta F(\mathbf{r}, t + \tau_{n-1})) \\ &= \sum_{k=1}^N A_k^n U^n(\mathbf{r} - \mathbf{r}_k) \underbrace{\kappa(\delta s_k(t), \delta s_k(t + \tau), \dots, \delta s_k(t + \tau_{n-1}))}_{c_{n,k}(\tau_1, \dots, \tau_{n-1})}. \end{aligned} \quad (5.11)$$

The n -th order cumulant C_n of the image sequence is thus equal to the sum of n -th power of the PSFs $U^n(\mathbf{r} - \mathbf{r}_k)$ weighted by the n -th power of the molecular intensities A_k^n and the correlation-based factor $c_{n,k}$. With the narrowed PSF $U^n(\mathbf{r})$, the resulting image $C_n(\mathbf{r})$ offers a \sqrt{n} -fold resolution improvement. This corresponds to the simplest approach to achieve super-resolution, illustrated in Fig. 5.5 (dashed line).

5.2.2 The principle of cumulant imaging

In addition to the resolution enhancement, the different cumulant orders of an image sequence permit to extract the molecular density, their brightness and the blink statistics offering a functional imaging method (Fig. 5.5, dot-dashed line).

In the simplest case of zero time lags, we have $X_1 = \dots = X_n = \delta F(\mathbf{r}, t)$. The computation of the forth order auto-cumulant simplifies for example to (see Appendix A.3)

$$C_4(\mathbf{r}) = \langle \delta F^4(\mathbf{r}, t) \rangle_t - 3 \langle \delta F^2(\mathbf{r}, t) \rangle_t^2. \quad (5.12)$$

In the case of zero time lags, the correlation-based factor $c_{n,k}$ can be expressed by the ratio of dark to bright states $r = \tau_{off}/\tau_{on}$. The blinking of the molecules is modeled with the binary switching function s_k , which is either 0 or 1. This corresponds to a Bernoulli distribution $X \sim P(p_k)$ with a probability

$$p_k = \tau_{k,on}/(\tau_{k,on} + \tau_{k,off}) = 1/(1 + r_k) \quad (5.13)$$

of the fluorescent molecule k to be in the on state. The first four cumulants are (see Appendix A.4)

$$\begin{aligned} c_1(\mathbf{r}_k) &= p_k \\ c_2(\mathbf{r}_k) &= p_k(1 - p_k) \\ c_3(\mathbf{r}_k) &= p_k(1 - p_k)(1 - 2p_k) \\ c_4(\mathbf{r}_k) &= p_k(1 - p_k)(1 - 6p_k(1 - p_k)). \end{aligned} \quad (5.14)$$

In a certain environment of a pixel \mathbf{r} , we assume that the $N(\mathbf{r})$ locally detectable molecules are freely rotating, have the same brightness $A(\mathbf{r})$ and the same bright state probability $p_k \approx p(\mathbf{r})$ for all k because they have the same chemical environment and uniform absorption and emission. The extension of the local region is defined by the radius of detectable molecules, which depends on the system's PSF and the SNR. The detectable intensity per molecule is then $A_k(\mathbf{r}) \approx \gamma(\mathbf{r}_k) A(\mathbf{r})$, where $\gamma(\mathbf{r})$ is the local illumination distribution. Under these assumptions and with zero time lags, the cumulants of the image sequence can be written as

$$C_n(\mathbf{r}) = \sum_{k=1}^{N(\mathbf{r})} A_k^n(\mathbf{r}) U^n(\mathbf{r} - \mathbf{r}_k) c_n(\mathbf{r}) \approx N(\mathbf{r}) A^n(\mathbf{r}) \mathbb{E}\{\gamma^n(\mathbf{r}_k) U^n(\mathbf{r} - \mathbf{r}_k)\} c_n(\mathbf{r}). \quad (5.15)$$

The latter approximation is unbiased and approaches the exact value for $N(\mathbf{r}) \rightarrow \infty$. The expectation value $\mathbb{E}\{\gamma^n(\mathbf{r}_k) U^n(\mathbf{r} - \mathbf{r}_k)\}$ depends on the illumination distribution $\gamma(\mathbf{r})$ and the molecular distribution \mathbf{r}_k . In the case of a locally uniform illumination (constant on the scale of the system's PSF, for instance wide-field illumination), we have $\gamma(\mathbf{r}) \approx 1$. For uniformly distributed molecules in d dimensions, the expectation values (moments) are [71]

$$m_n^{(d)} = \mathbb{E}\{U^n(\mathbf{r} - \mathbf{r}_k)\} = u(\sigma_{xy}, \sigma_z) \cdot n^{-d/2}, \quad (5.16)$$

where u is a constant depending on the PSF shape. Equation (5.16) is for an infinitely large detection radius $R \rightarrow \infty$. Due to background noise and shot noise, only molecules within a limited radius R are detected. For sufficiently large radii $R > 2\sigma$, the relative error of the moments in Equation (5.16) remains below 2%, though.

In the case of an evanescent illumination (for instance TIR illumination), we have to take into account the local illumination distribution $\gamma(\mathbf{r})$ because the illumination intensity varies on the scale of the PSF. For an evanescent field decaying along one dimension, the moments can be expressed as

$$m_n^{(TIR)} = \mathbb{E}\{\gamma(\mathbf{r}_k) U^n(\mathbf{r} - \mathbf{r}_k)\} = u_\gamma(\sigma_{xy}, \sigma_z, d_z) \cdot n^{-2}, \quad (5.17)$$

where u_γ is a constant depending on the PSF and the excitation field shape. The relative error for a limited detection radius $R > 3\sigma$ is below 2%. In confocal imaging with uniformly distributed molecules, the illumination can be assumed to be Gaussian, approximately with the same distribution as the emission PSF. Consequently, the resulting detection PSF is a Gaussian with a smaller width. Thus, the decay of the moments with respect to the order is the same as for uniformly distributed molecules in wide-field illumination.

In all cases, wide-field and TIRF illumination, the cumulants can now be written as

$$\begin{aligned}
 C_1(\mathbf{r}) &\approx N(\mathbf{r})A(\mathbf{r})m_1p(\mathbf{r}) + b(\mathbf{r}) \\
 C_2(\mathbf{r}) &\approx N(\mathbf{r})A^2(\mathbf{r})m_2p(\mathbf{r})(1-p(\mathbf{r})) \\
 C_3(\mathbf{r}) &\approx N(\mathbf{r})A^3(\mathbf{r})m_3p(\mathbf{r})(1-p(\mathbf{r}))(1-2p(\mathbf{r})) \\
 C_4(\mathbf{r}) &\approx N(\mathbf{r})A^4(\mathbf{r})m_4p(\mathbf{r})(1-p(\mathbf{r}))(1-6p(\mathbf{r})(1-p(\mathbf{r}))), \\
 &\vdots
 \end{aligned} \tag{5.18}$$

where $b(\mathbf{r})$ is a constant background. From the last three equations we can extract the estimated values for $A(\mathbf{r})$, $p(\mathbf{r})$ and $N(\mathbf{r})$:

$$\begin{aligned}
 A^2(\mathbf{r}) &\approx 3 \left(k_{32}(\mathbf{r}) \frac{m_2}{m_3} \right)^2 - 2k_{42}(\mathbf{r}) \frac{m_2}{m_4} \\
 p(\mathbf{r}) &\approx \frac{1}{2} - \frac{k_{32}(\mathbf{r})}{2} \left(3k_{32}^2(\mathbf{r}) - 2k_{42}(\mathbf{r}) \frac{m_3^2}{m_2m_4} \right)^{-1/2} \\
 N(\mathbf{r}) &\approx \frac{C_2(\mathbf{r})}{A(\mathbf{r})m_2p(\mathbf{r})(1-p(\mathbf{r}))},
 \end{aligned} \tag{5.19}$$

where $k_{ij}(\mathbf{r}) = C_i(\mathbf{r})/C_j(\mathbf{r})$. The moments m_n depend on the sample and the illumination only and are assumed to be constant over the field of view. For a uniform 3D sample distribution and a wide-field illumination for instance, the moments are $m_n \propto n^{-3/2}$ which yields

$$\begin{aligned}
 A^2(\mathbf{r}) &\approx \frac{81}{8} k_{32}^2(\mathbf{r}) - 4\sqrt{2}k_{42}(\mathbf{r}) \\
 p(\mathbf{r}) &\approx \frac{1}{2} - \frac{k_{32}(\mathbf{r})}{2} \left(3k_{32}^2(\mathbf{r}) - \frac{32\sqrt{2}}{27}k_{42}(\mathbf{r}) \right)^{-1/2}.
 \end{aligned} \tag{5.20}$$

These equations are unbiased for molecular concentrations with more than ≈ 10 molecules per PSF. Below this concentration, there is maximally one dominating molecule detected per pixel only and the sum in Equation (5.15) consists of a single element, which equals to the Equations (5.18) with $m_n = 1 \forall n$. For sparsely distributed single molecules the Equations (5.20) yield therefore biased values (see Fig. 5.17 (b)). This is avoided by putting the moments m_n to unity:

$$\begin{aligned}
 A^2(\mathbf{r}) &\approx 3k_{32}^2(\mathbf{r}) - 2k_{42}(\mathbf{r}) \\
 p(\mathbf{r}) &\approx \frac{1}{2} - \frac{k_{32}(\mathbf{r})}{2} \left(3k_{32}^2(\mathbf{r}) - 2k_{42}(\mathbf{r}) \right)^{-1/2}.
 \end{aligned} \tag{5.21}$$

The choice of either (5.20) or (5.21) could be selected automatically by estimating the molecule number $N(\mathbf{r})$ and correcting iteratively the moments before re-estimating $N(\mathbf{r})$, $A(\mathbf{r})$ and $r(\mathbf{r})$. Otherwise, the bias of the estimation of $p(\mathbf{r})$ can go up to 0.15. The estimation of $A(\mathbf{r})$ is less robust and the error can go up to 100%. This makes sense, since if the molecule is not centered on the pixel, its emission intensity is underestimated in function of the spatial distribution of

its emission pattern. Related to this, also the estimation of $N(\mathbf{r})$ is subject to important errors. Therefore $A(\mathbf{r})$ and $N(\mathbf{r})$ should rather be interpreted qualitatively only.

Besides the dependency on the illumination intensity, $A(\mathbf{r})$ and $r(\mathbf{r})$ give an information about the chemical microenvironment. The blink statistics for example depend on the concentration of reducing and oxidizing agents (see Chapter 4). In addition, it helps to evaluate whether a sample is more adapted either for SOFI or STORM imaging and what resolution improvement can be expected.

5.2.3 SOFI-Fourier reweighting

Regarding the resolution given by the PSF, the optical transfer function (OTF) is an equivalent measure of the performance of an optical system. The OTF $\tilde{U}(\mathbf{k})$ is the Fourier transform of the PSF $U(\mathbf{r})$ and represents the image contrast of given spatial frequencies \mathbf{k} in the object. The OTF has a finite support and the cut-off of the spatial frequencies is proportional to the numerical aperture of the system. The PSF of the n -th order SOFI image is given by the n -th power of the system's PSF $U(\mathbf{k})$ ((5.11)). The corresponding SOFI OTF $O(\mathbf{k})$ is consequently equal to $(n - 1)$ convolutions of the system's OTF $\tilde{U}(\mathbf{k})$ with itself:

$$U^n(\mathbf{r}) \xrightarrow{\text{Fourier}} \underbrace{\tilde{U}(\mathbf{k}) * \dots * \tilde{U}(\mathbf{k})}_{(n-1)\text{-times}} = O(\mathbf{k}). \quad (5.22)$$

The support of the OTF $O(\mathbf{k})$ is thus n -times larger than the inherent OTF of the imaging system (c.f. Titchmarsh convolution theorem [121]). Supposing no noise, this means that n -times higher spatial frequencies can be resolved and an n -fold resolution improvement should physically be possible, which is in contrast to the \sqrt{n} -fold resolution improvement assuming a Gaussian PSF. Based on this idea, Dertinger et al. [20] proposed a reshaping of the n -fold convolution of the OTF $O(\mathbf{k})$ to yield an n -times stretched OTF $\tilde{U}(\mathbf{k}/n)$ by enhancing the contrast of certain frequencies (see Figures 5.4 and 5.5). This reweighting scheme in the Fourier space of the cumulant image is formalized as

$$W(\mathbf{k})O(\mathbf{k}) \approx \tilde{U}(\mathbf{k}/n) \xrightarrow{\text{Fourier}^{-1}} U(n\mathbf{r}) \quad \text{with} \quad W(\mathbf{k}) = \frac{\tilde{U}(\mathbf{k}/n)}{O(\mathbf{k}) + \alpha}, \quad (5.23)$$

where α is a damping factor to avoid the division by zero and reduce the amplification of background noise. This results nearly in a n -times shrunked PSF $U(n\mathbf{r})$ and a resolution improvement of almost the order of the cumulant image (see Fig. 5.4). In contrast to a deconvolution, this method only takes into account spatial frequencies that are physically possible as pointed out by Dertinger et al. [20]. Therefore it introduces less artifacts than the deconvolution.

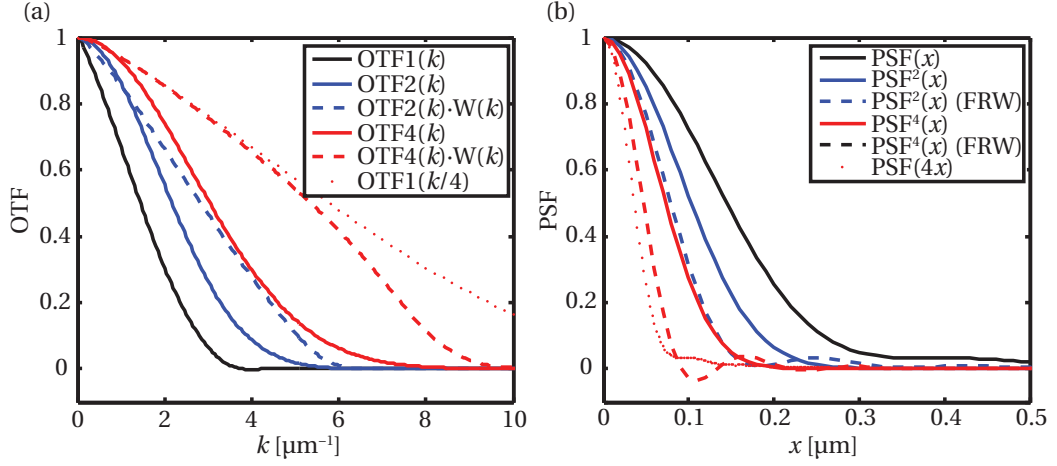


Figure 5.4: Performance of the SOFI imaging system shown by the corresponding PSF and OTF. **(a)** OTF1(k) is the systems's OTF $\tilde{U}(k)$; OTF2(k) and OTF4(k) are the OTFs of PSF put to the power of 2 and 4 respectively (solid lines). The Fourier reweighting (FRW) is achieved with the weighing function $W(k)$ (dashed lines) calculated with a damping factor $\alpha = 0.01$. The four times stretched system's OTF is shown for comparison (dotted line). **(b)** The equivalent PSFs of the OTFs shown in (a).

5.2.4 Cross-cumulants

So far, n -th order temporal auto-cumulants of a pixel with itself have been considered for zero or non-zero time lags. Cumulants can also be calculated *between* different pixels at given time lags (see Fig. 5.3). Assuming a Gaussian PSF $U(\mathbf{r})$ a second order-cross cumulant (cross-correlation) corresponds to [19]:

$$\begin{aligned} XC_2(\mathbf{r}_1, \mathbf{r}_2, \tau) &= \sum_{k=1}^N A_k^2 U(\mathbf{r}_1 - \mathbf{r}_k) U(\mathbf{r}_2 - \mathbf{r}_k) \langle \delta s_k(t + \tau) \cdot \delta s_k(t) \rangle_t \\ &= U\left(\frac{\mathbf{r}_1 - \mathbf{r}_2}{\sqrt{2}}\right) \cdot \sum_{k=1}^N A_k^2 U^2\left(\mathbf{r}_k - \frac{\mathbf{r}_1 + \mathbf{r}_2}{2}\right) c_{n,k}(\tau). \end{aligned} \quad (5.24)$$

Accordingly, spatio-temporal cross-cumulants of the n -th order can be written as:

$$XC_n(\mathbf{r}_1, \dots, \mathbf{r}_n, \tau_1, \dots, \tau_{n-1}) = \underbrace{\prod_{j < l}^n U\left(\frac{\mathbf{r}_j - \mathbf{r}_l}{\sqrt{n}}\right)}_{d(\mathbf{r}_1, \dots, \mathbf{r}_n)} \cdot \sum_{k=1}^N A_k^n U^n\left(\mathbf{r}_k - \frac{\sum_{i=1}^n \mathbf{r}_i}{n}\right) c_{n,k}(\tau_1, \dots, \tau_{n-1}) \quad (5.25)$$

The cross-cumulant XC_n is very similar to an auto-cumulant C_n that would be evaluated at the center of gravity $\langle \mathbf{r}_i \rangle_i$ and weighted by a factor $d(\mathbf{r}_1, \dots, \mathbf{r}_n)$ depending on the inter-pixel

distances and the system's PSF $U(\mathbf{r})$ (see Fig. 5.5). If the auto-cumulant C_n is defined at $\langle \mathbf{r}_i \rangle_i$ and in the case without noise, we can write:

$$XC_n(\mathbf{r}_1, \dots, \mathbf{r}_n, \tau_1, \dots, \tau_{n-1}) = d(\mathbf{r}_1, \dots, \mathbf{r}_n) C_n(\langle \mathbf{r}_i \rangle_i, \tau_1, \dots, \tau_{n-1}). \quad (5.26)$$

By considering several cross-cumulant combinations or by comparing to the corresponding auto-cumulants if they exist, the distance factor $d(\mathbf{r}_1, \dots, \mathbf{r}_n)$ can be used to estimate the PSF $U(\mathbf{r})$ (see Fig. 5.5). The parameters of the PSF are found by optimizing them iteratively until all pixels have similar weights. We have used the 2D Laplacian as a cost-function of the optimization algorithm, which turned out to be robust. The distance factors can also be calculated by assuming a given image formation model with corresponding PSF. In the case of a shot noise limited acquisition, however, the auto-cumulant $C(\mathbf{r})$ has a positive bias equal to the mean intensity because the cumulant of a Poisson noise corresponds to its mean for all orders.

Cross-cumulants offer two main advantages: First, even for zero time lags non-correlated noise (for instance shot noise) is efficiently suppressed for cross-cumulants while auto-cumulants of zero time lag suffer from a bias. Compared to non-zero time lags, the requirements on sample and hardware for zero time lags are more relaxed and the acquisition rate has only to be in the same order as the blinking rate. While auto-cumulants of zero time lag suffer from a bias, cross-cumulants can efficiently reject non-correlated noise and offer a higher SNR (see Section 5.2.5). Second, cumulant values between the physical pixels (inter pixels) can be generated resulting in a subsampling, i.e. a finer pixel grid. This way the SOFI-image resolution can exceed the resolution limit given by the physical pixel sampling. This is necessary to compete with STORM imaging, where the localization accuracy is better than the resolution limit of the physical pixel sampling. An example of how a finer pixel grid can be computed was shown in Fig. 5.3.

Figure 5.5 summarizes the SOFI algorithms for super-resolution imaging as well as the functional approach of the cumulant imaging. An overview of the SOFI-algorithms with their advantages and disadvantages is presented in Table 5.1.

5.2.5 Signal-to-noise ratio of cumulants

The SNR of a data set can be modified by any post-processing. It is therefore interesting and important to know, how the SNR evolves for increasing SOFI orders and how it depends on the molecule amplitude A , the on rate p , the molecule number N and a constant background b .

The signal corresponding to a single molecule is $S = Ap$ on a floor of background including the N blinking molecules $NAp + b$. This background floor is subject to shot noise. The SNR of a cumulant of the order n can then be written as

$$\text{SNR}(C_n) = \frac{C_n(S)}{\sigma\{C_n(NAp + b)\}}, \quad (5.27)$$

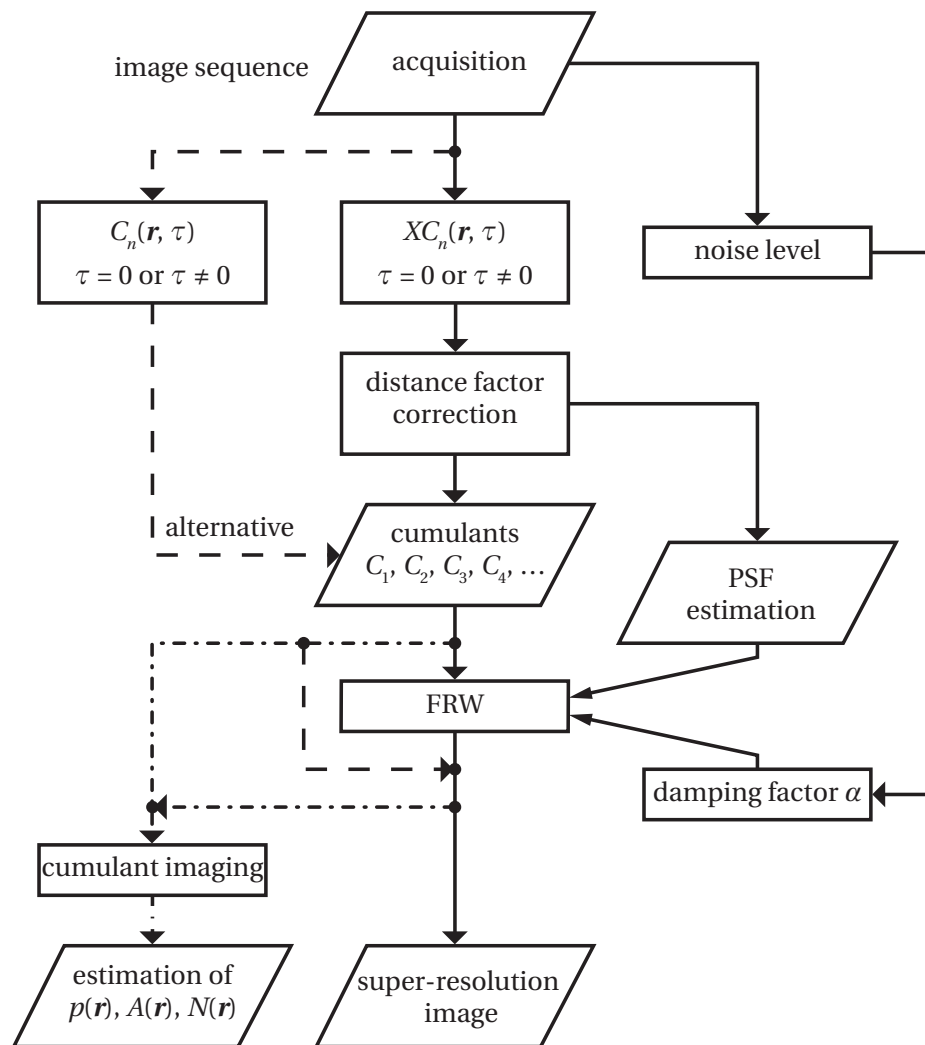


Figure 5.5: Overview of SOFI algorithms.

	auto-cumulants	cross-cumulants	
		with repetitions	without repetitions
zero time lag	+ fast computation + unlimited order – no refined pixel grid – biased	+ unlimited order + improved SNR – repetitions decrease SNR – estimation of PSF needed	+ highest SNR + no bias – limited order – slow computation – estimation of PSF needed
non-zero time lag	+ no bias + good SNR + additional absolute time information	– slow blinking required with respect to the acquisition rate otherwise low SNR	
Fourier reweighting	+ enhanced resolution + risk of artifact generation	– estimation of PSF needed	

Table 5.1: Overview of SOFI methods presented in this work with their advantages and disadvantages.

where $\sigma\{\}$ gives the standard deviation generated by the shot noise of $NAp + b$. For cross-cumulants, which are preferably used in the following, the derivation is particularly simple. Up to the third order, the cumulants correspond to the centered moments. Since, in the case of independent random variables with zero mean X_i , the variance of a product is equal to the product of the variances, we have for $n \leq 3$

$$\sigma\{XC_n(X_1, \dots, X_n)\} = \sigma\{\langle X_1 \dots X_n \rangle_t\} = \frac{1}{\sqrt{N_f}} \sigma\{X_1 \dots X_n\} = \frac{1}{\sqrt{N_f}} \sigma\{X_1\} \dots \sigma\{X_n\}, \quad (5.28)$$

where N_f is the number of acquired frames. For $n > 3$, the additional partition terms (see Appendix A.3) are negligible if a sufficient number of frames are acquired. This is verified by simulation (Fig. 5.6 (a)). Those terms are weakened because of the division by additional $\sqrt{N_f}$ coming from averaging over the acquired frames. Thus, the number of acquired frames has to be increased at higher orders to counteract the noise from an increasing number of partition terms. The number of two-partition ($|\Pi| = 2$) terms are the first to become significant. Therefore we get the following condition on the number of frames N_f for the order n (c.f. Stirling numbers of the second kind [35]):

$$N_f > \left(\left\{ \begin{matrix} n \\ 2 \end{matrix} \right\} - n \right)^2 = (2^{n-1} - 1 - n)^2. \quad (5.29)$$

Auto-cumulants are more sensitive to noise (see Fig. 5.6 (a)) and are biased. For cross-cumulants though, the signal is weakened by an additional distance factor scaling in our algorithm with $\approx \exp(-n^2/(12\sigma_{\text{PSF}}^2))$ (see Fig. 5.6 (b)) and depending on the system's PSF σ_{PSF} measured in pixels. For very high orders or larger pixels with respect to the PSE, this term becomes predominant and auto-cumulants may become favorable.

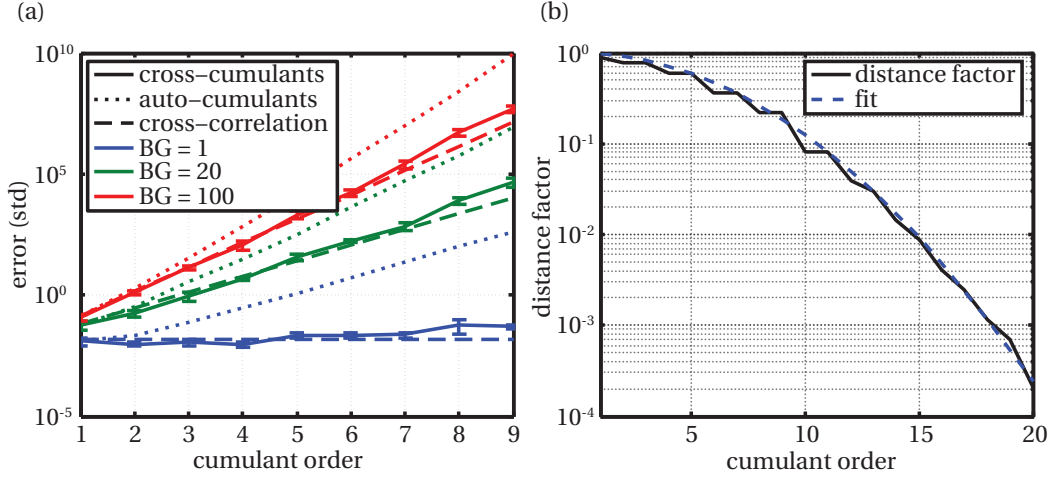


Figure 5.6: (a) Sensitivity of cross-cumulants and auto-cumulants on shot noise of a background BG in function of the order. The cross-cumulants are comparable to cross-correlations, whereas auto-cumulants are more sensitive to noise. (b) Decay of the distance factor for $\sigma_{\text{PSF}} = 2$ with an empirical fit: $\exp(-n^2/(12\sigma_{\text{PSF}}^2))$.

For Poisson distributed noise, we have $\sigma\{X_i\} = \sqrt{\mathbb{E}\{X_i\}}$ and as long as the condition (5.29) is complied the expected SNR of cross-cumulants can be written as

$$\begin{aligned}
 \text{SNR}(XC_2) &\approx \sqrt{N_f} \frac{A^2 p(1-p)}{NAp+b} \cdot \exp\left(-\frac{1}{\sigma_{\text{PSF}}^2}\right) \\
 \text{SNR}(XC_3) &\approx \sqrt{N_f} \frac{A^3 p(1-p)(1-2p)}{(NAp+b)^{\frac{3}{2}}} \cdot \exp\left(-\frac{1}{\sigma_{\text{PSF}}^2}\right) \\
 &\vdots \\
 \text{SNR}(XC_n) &\approx \sqrt{N_f} \left(\frac{A}{\sqrt{NAp+b}}\right)^n \cdot \exp\left(-\frac{n^2}{12\sigma_{\text{PSF}}^2}\right) \kappa_n(X \sim P(p)).
 \end{aligned} \tag{5.30}$$

These equations show that like in FCS, the SNR decreases for an increasing number of molecules. The optimal on rate p is lower than 0.5 and approaches zero for higher orders.

5.3 Simulation & Experimental Details

5.3.1 Simulation

Based on a simulation, we investigated the performance of the SOFI and STORM algorithms under the aspects of photo-switching kinetics, labeling density and SNR. This work is published in [31]. The simulation generates image sequences of randomly blinking fluorescent molecules that are placed arbitrarily on two parallel bands, each 0.04 Airy units wide, at different separation distances. The molecular blinking behavior was simulated as a time-

continuous Markov process between on and off states using a 100-fold temporal oversampling. The average blinking rate is then given by

$$k = \frac{k_{on}k_{off}}{k_{on} + k_{off}}, \quad (5.31)$$

where $k_{on} = \tau_{off}^{-1}$ denotes the rate at which the fluorescent molecule is transferred from the off state back to the on state and vice versa for $k_{off} = \tau_{on}^{-1}$. k was fixed to half the sampling rate (f) but was not synchronized with the acquisition time intervals. The number of emitted photons per molecule followed a Poisson probability-density distribution with an average photon count rate of 9 kHz in the on state. Similar to measurements, a constant background of 40% of the average molecular amplitude and shot noise was added. For simplicity, we used a Gaussian PSF model with a full-width at half-maximum (FWHM) equal to one Airy unit (237 nm; corresponding to a numerical aperture (NA) of 1.49 and an emission wavelength of 580 nm). The pixel size was 100 nm. For computational ease and to limit the length of the image sequences, we applied generally low labeling densities (5-20/ μm), which allow longer fluorescence on-times with respect to their off-times, i.e., a low rate ratio

$$r = \frac{k_{off}}{k_{on}} = \frac{\tau_{off}}{\tau_{on}}. \quad (5.32)$$

However, we expect the effect to be similar at higher labeling densities if accordingly higher rate ratios and sequence lengths are used.

We compared the *relative visibility* v (in the following referred to as visibility) of the projected line profiles, defined as

$$v_0 = 0.5 \frac{I_{max,1} - I_{min}}{I_{max,1} + I_{min}} + 0.5 \frac{I_{max,2} - I_{min}}{I_{max,2} + I_{min}} \quad (5.33)$$

$$v = v_0 \left(\frac{\min\left\{\frac{I_{max,1}}{I_1}, \frac{I_{max,2}}{I_2}\right\}}{\max\left\{\frac{I_{max,1}}{I_1}, \frac{I_{max,2}}{I_2}\right\}} \right)^{\text{sign}\{v_0\}}, \quad (5.34)$$

where $I_{max,1}$, $I_{max,2}$, I_{min} , I_1 and I_2 are defined according to Fig. 5.7.

In addition to the comparison between SOFI and STORM, we investigated the characteristics of cumulant imaging based on the same Monte Carlo simulation. Parameter maps have been attributed to ordered or random distribution of molecules with the goal to visualize the performance of cumulant imaging computed by cross cumulants without Fourier reweighting. For the quantitative characterization, longer sequences of one or more molecules were generated on a single pixel. In this case auto-cumulants were computed and corrected for their bias due to shot noise by subtraction of the square root of the mean intensity.

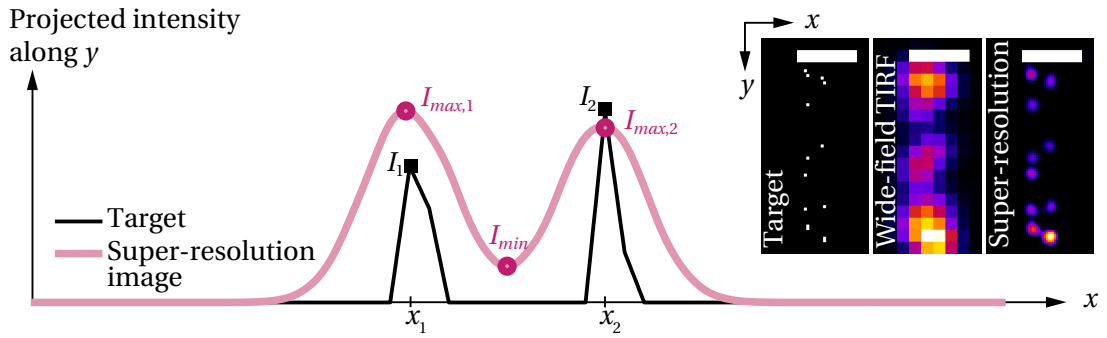


Figure 5.7: The visibility defined in eq. (5.34) serves as a benchmark for comparing the different algorithms. The line profiles are obtained by projecting the images along the y direction. $I_{max,1}$ and $I_{max,2}$ are obtained by taking the mean intensity at the known positions of the lines (x_1 and x_2) and I_{min} is the mean intensity between $0.4(x_1 + x_2)$ and $0.6(x_1 + x_2)$. Scale bars: 500 nm.

5.3.2 Experiments

We used a custom-designed total-internal-reflection fluorescence (TIRF) microscope in epi-illumination with an oil-immersion objective (Olympus 60x1.49) and two laser excitation sources. Fixed human osteosarcoma cells (U2OS) expressing a β -tubulin-SNAP tag [98] have been labeled with a photo-switchable probe (BG-Cy3-Cy5) and an imaging buffer containing mercaptoethanol, and an oxygen-scavenging system was used to increase the dark state lifetime of Cy5. All experimental details can be found in Chapter 4 and in [17].

Regarding the cumulant imaging, quantum dots are perfectly adapted to demonstrate the extraction of various blinking rates. A broad distribution of blinking rates in many timescale can be observed since their blinking rates follow a power law distribution [79]. In addition they show virtually no bleaching even in air. They have been dried on a microscopy cover slide, excited at 490 nm and imaged using the same microscope as for STORM imaging.

5.4 Simulation results

5.4.1 Resolution enhancement with SOFI

Effect of photo-switching kinetics

In Figures 5.8 and 5.9, we compare the effects of varying the rate ratio on the visibility of the two lines in STORM and the different SOFI orders. Van de Linde et al. [126] have already shown that a high rate ratio is crucial for successful STORM imaging, as is confirmed by Figures 5.8(a), 5.9(d) and 5.9(f). Due to the stochastic nature of the photo-switching dyes, it is always possible to have multiple emitters in a diffraction-limited spot. If they are too close to be identified as an agglomeration, the Gaussian fit results in a false localization. The number

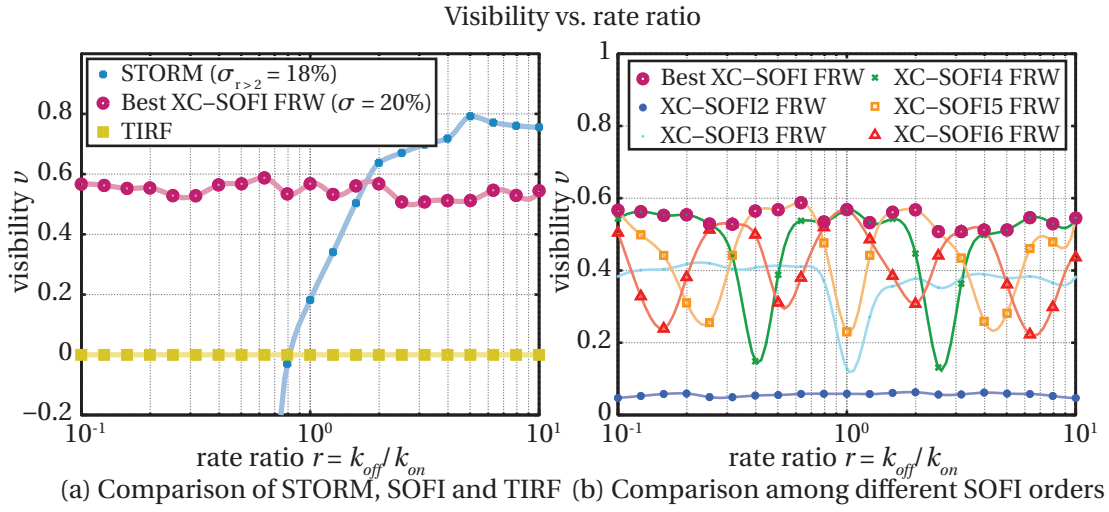


Figure 5.8: Comparison of the visibility versus rate ratio. The best XC-SOFI is obtained by the SOFI order yielding the highest average relative visibility for a specific set of simulation parameters. σ denotes the average relative standard deviation. *Fixed simulation parameters:* $k/f = 0.5$, line separation: 0.6 Airy units, labeling density: $5/\mu\text{m}$, 1000 frames, 50 realizations per point.

of false localizations increases with lower rate ratios. At a specific cut-off rate ratio, where multiple emitters are always present in a diffraction-limited spot, STORM fails completely (Fig. 5.8(a) at $r < 1$ and Fig. 5.9(d)).

SOFI, on the other hand, is more robust. Considering different SOFI orders, the visibility is almost independent of the rate ratio (see Fig. 5.8(a)), which therefore relaxes the photo-physical constraints of the emitter. Figure 5.8(b) illustrates how different SOFI orders can be used to characterize the blinking nature and statistics. For example, if the blinking is symmetric ($k_{on} = k_{off}$), the skewness or third-order is zero, leading to a visibility $\nu = 0$. This result is similar to other odd higher-order cumulants, where an asymmetry must be present.

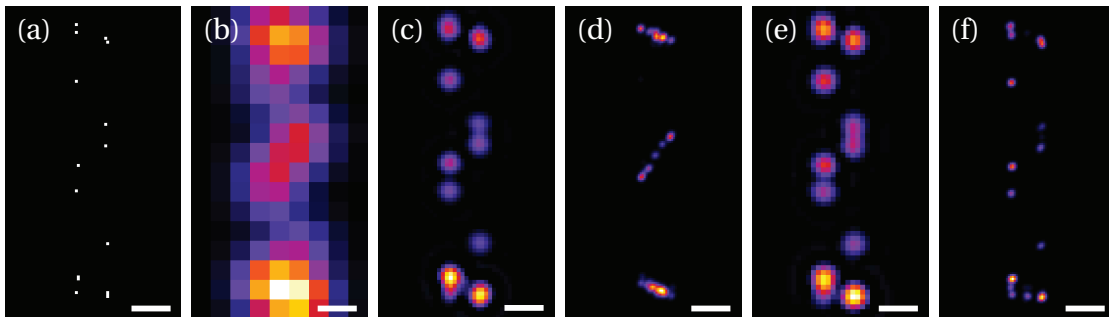


Figure 5.9: Visual comparison of SOFI and STORM reconstructions at different rate-ratios. (a) Target structure. (b) Summed TIRF. (c) XC-SOFI5 FRW, $r = 0.6$. (d) STORM, $r = 0.6$. (e) XC-SOFI4 FRW, $r = 10$. (f) STORM, $r = 10$. Scale bars: 200 nm.

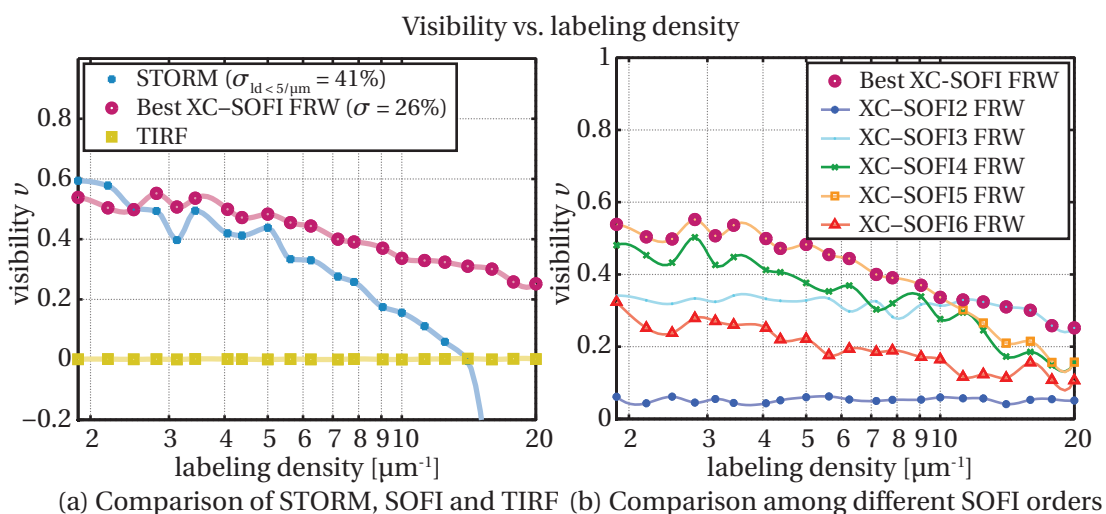


Figure 5.10: Comparison of the visibility versus labeling density. The best XC-SOFI is obtained by the SOFI order yielding the highest average relative visibility for a specific set of simulation parameters. σ denotes the average relative standard deviation. *Fixed simulation parameters: $k/f = 0.5$, $r = 2$, line separation: 0.6 Airy units, 1000 frames, 25 realizations per point.*

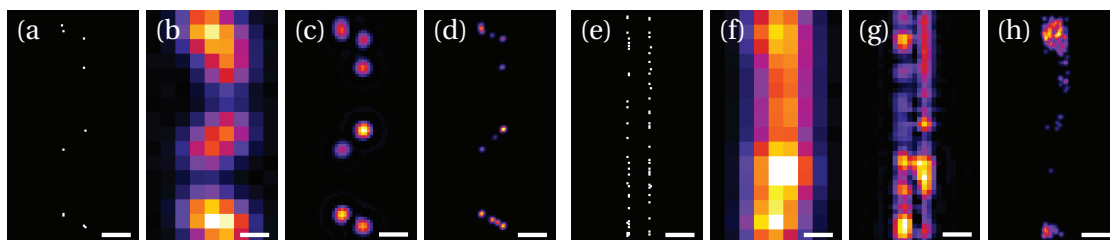


Figure 5.11: Visual comparison of SOFI and STORM reconstructions at different labeling densities. Labeling density: (a-d) $3/\mu\text{m}$, (e-h) $20/\mu\text{m}$. (a,e) Target structure. (b,f) Summed TIRF. (c) XC-SOFI5 FRW. (g) XC-SOFI3 FRW. (d,h) STORM. *Scale bars: 200 nm.*

For the second-order, the rate ratio does not have any effect on the visibility as long as it is the same for all molecules because the variance of the blinking is the measured quantity.

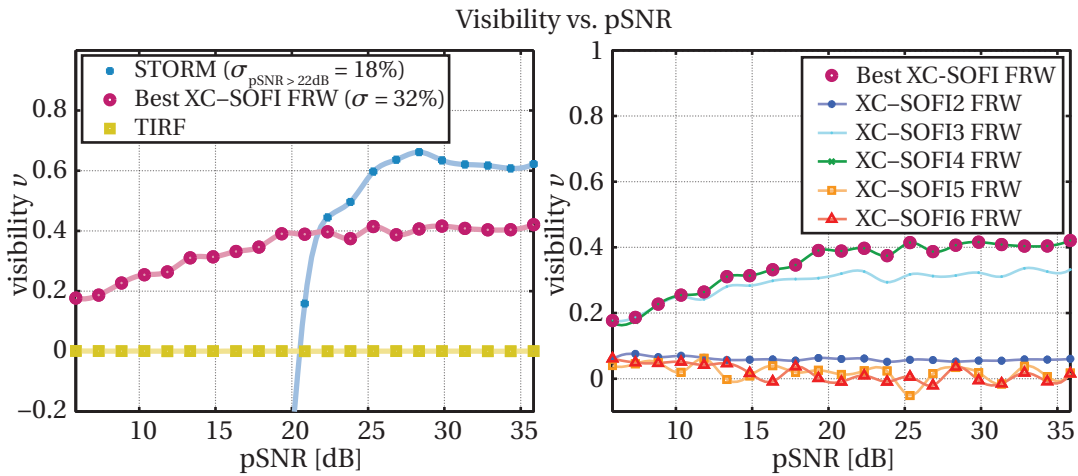
Effect of labeling density

The effect of the labeling density is depicted in Figures 5.10 and 5.11. In STORM imaging, the labeling density is directly linked to the cut-off rate ratio [126]. Higher labeling densities require higher rate ratios to ensure the occurrence of isolated single-emitter diffraction patterns. In the example in Fig. 5.10(a), with a rate ratio of 2, the labeling density should not exceed $10 \mu\text{m}$, otherwise false localizations predominate (Fig. 5.11(h)).

In SOFI, the decrease in visibility with increasing labeling density is less pronounced and is due to the decreased relative intensity fluctuations. Figure 5.10(b) reveals a stronger decrease for higher orders.

Effect of the signal-to-noise ratio

In single-molecule localization, the accuracy essentially scales inversely with the number of collected photons [120]. A sufficiently high SNR per frame has to be guaranteed to estimate the position with high precision. Similar to FCS analyzing fast fluorescence intensity fluctuations, SOFI can be expected to work with a much lower SNR than localization microscopy. Figure 5.12 illustrates the effect of the peak signal-to-noise ratio (pSNR) on the visibility for STORM and the different SOFI orders. Figure 5.12(b) shows that SOFI orders 2 to 4 can be used to generate super-resolution images until 10 to 20 dB below the minimum pSNR needed for STORM. This implies that when using a fast camera, SOFI could have a significant speed advantage over localization microscopy. For example, a drop of 50% in visibility for SOFI order 3 occurs only at about 5 dB, whereas for STORM this already occurs at 22 dB. Assuming a constant detector sensitivity and a shot-noise-limited system with a square-root dependence of SNR on time, the acquisition rate could then be about 45 times higher. In this simulation, we used the cross-cumulant approach without repetitions to efficiently eliminate shot noise. The low visibilities for SOFI orders 5 and 6 are due to cross-cumulant combinations between pixels further apart than the FWHM of the PSF (here, 2.3 px). This issue might be addressed using non-zero time lags and using the combination scheme with repetitions.

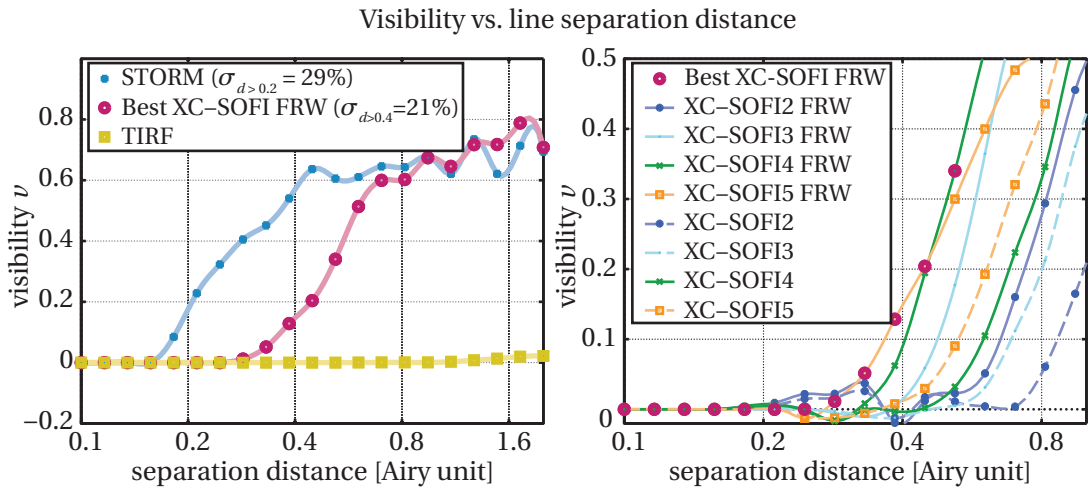


(a) Comparison of STORM, SOFI and TIRF (b) Comparison among different SOFI orders

Figure 5.12: Comparison of the visibility versus pSNR. XC-SOFI has been computed using cross-cumulant combinations without repetitions. The best XC-SOFI is obtained by the SOFI order yielding the highest average relative visibility for a specific set of simulation parameters. σ denotes the average relative standard deviation. *Fixed simulation parameters:* $k/f = 0.5$, $r = 6.7$, *line separation:* 0.6 Airy units, *labeling density:* $5/\mu\text{m}$, 2000 frames, 50 realizations per point.

Effect of the line separation distance

In localization-based super-resolution microscopy, the resolution is often estimated from the accuracy of single-molecule localization. This estimation assumes that the dark time is sufficiently high such that single emitters still appear isolated in time in the regions of highest labeling densities. The localization accuracy cannot be linked to the minimum distance between two objects that are still distinguishable as long as the labeling densities and photo-switching kinetics are unknown. Using our simulation to compare the visibility versus the line separation distance enables the analysis of the effective resolutions of STORM and SOFI for given on- and off-rates, frame rate, labeling density, sequence length and SNR. Figure 5.13 shows an example in which the rate ratio is sufficiently high for STORM to resolve the structures of a given labeling density until the separation distance gets close to the FWHM localization accuracy limit. Table 5.2 lists the corresponding limits of resolution in Airy units. The values correspond to the separation distances, where the visibility grows larger than 10^{-3} . In the case of SOFI, small oscillations around zero visibility can be seen when approaching the resolution limit (see Fig. 5.13b). These oscillations are due to numerical effects arising from sampling close to the Nyquist limit, which corresponds to twice the resolving power. Increasing the magnification of the microscope would reduce these oscillations. The resolution limits of the different Fourier-reweighted SOFI orders were estimated by the points of deflection of the Fourier reweighted (XC-SOFI FRW) from the untreated SOFI (XC-SOFI) visibility curves.



(a) Comparison of STORM, SOFI and TIRF (b) Comparison among different SOFI orders

Figure 5.13: Comparison of the visibility versus line separation distance. The best XC-SOFI is obtained by the SOFI order yielding the highest average relative visibility for a specific set of simulation parameters. σ denotes the average relative standard deviation. *Fixed simulation parameters:* $k/f = 0.5$, $r = 6.7$, labeling density: $5/\mu\text{m}$, 2000 frames, 50 realizations per point.

Table 5.2: Limits of resolution in Airy units and the corresponding improvement factors with regards to wide-field TIRF

	TIRF	XC-SOFI-FRW				STORM
		2	3	4	5	
resolution limit	1.00	0.47	0.33	0.28	0.24	0.16
improvement	-	2.1x	3.0x	3.6x	4.2x	6.4x

5.4.2 Cumulant imaging

The cumulant imaging is not part of the published work [31]. This novel technique is subject of a patent and will be published shortly.

Rate ratio estimation

In this section, we present simulations to characterize the functional imaging with cumulants. The most interesting and accurate parameter that can be extracted by cumulant imaging is the rate ratio r . The performance is visualized in Fig. 5.14. In the first simulation, an individual rate ratio is attributed to each one of sparsely distributed molecules (Fig. 5.15 (a)). A constant background and shot noise is added to the simulated image sequence. The cumulant imaging retrieves the rate ratios with a resolution given by the second order cumulant (Fig. 5.14 (b)).

Like SOFI, cumulant imaging removes temporally constant background and suppresses shot noise efficiently. The estimation of the on ratio works perfectly for all $p \in (0, 1)$ down to

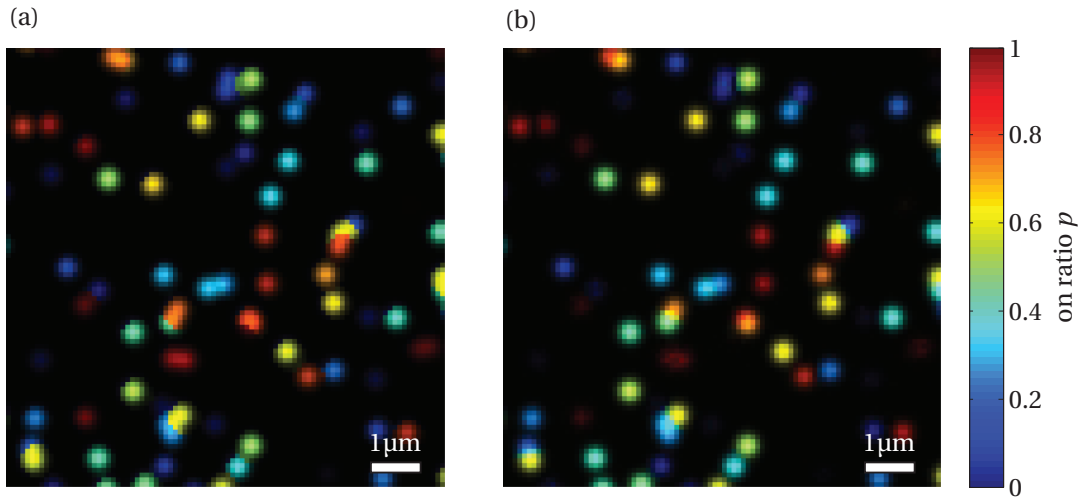


Figure 5.14: (a) Simulated distribution of molecules with different rate ratios. (b) Cumulant imaging of the on ratio p weighted by the second order cumulant computed from the simulated image sequence with background (SNR = 27dB). The brightness of the second order cumulant is overlaid by a color code visualizing the on ratio. Acquisition length: 1000 frames, SNR = 27dB.

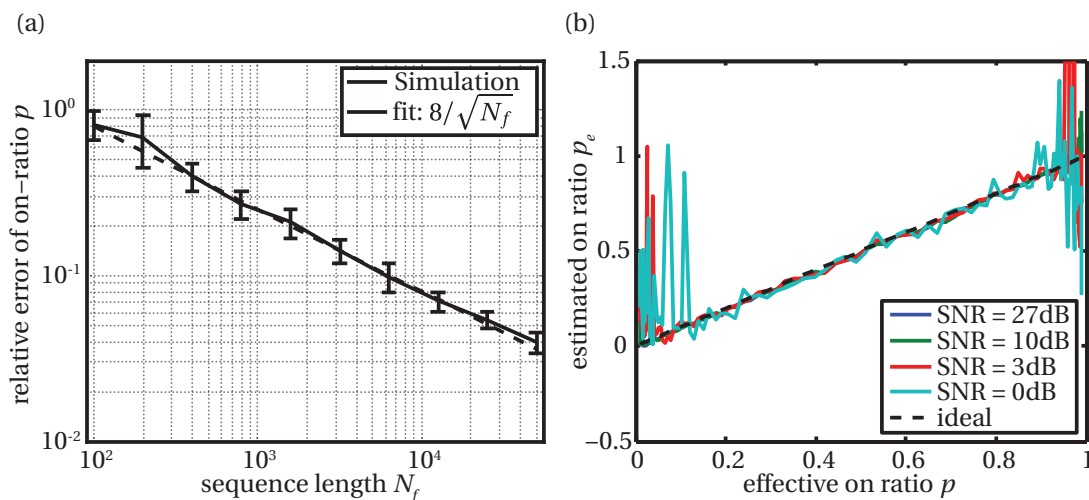


Figure 5.15: (a) Estimated on ratio p_e of a single molecule in function of the simulated on ratio p for several SNRs. Since it is a single molecule, the moments for the molecular distribution are put to unity (zero-dimensional case according to Equation (5.21)). Acquisition length: 10000 frames. (b) Relative error of the on ratio p for $0.1 < p < 0.9$ in function of the sequence length for a single molecule (according to Equation (5.21)). SNR = 27dB.

a SNR of 10dB. At very low SNR down to 0dB, the estimation still works accurately in the range $0.1 < p < 0.9$ (Fig. 5.15 (a)). The relative error of the on rate estimation is inversely proportional to the square root of the sequence length (Fig. 5.15 (b)) corresponding to the standard deviation of cumulants (see Section 5.2.5).

In FCS, the bin time of the sampling has to be at least one order of magnitude shorter than the characteristic time of the process to resolve. In contrast to FCS, the estimation of the rate ratio is successful down to an acquisition rate which is comparable to characteristic blink rate of the molecules (Fig. 5.16). Although the on- or off-*time* is not estimated with this method, their ratio is sufficient to extract microenvironmental information, since the on- and the off-rate are often triggered separately by specific agents (see Section 4.2.3). In addition, it can be imagined, however, that the time constants could be extracted by using cumulants with non-zero time lags.

In the preceding simulation (Figures 5.15 and 5.16), only one molecule has been considered with respect to the background. This corresponds to a zero-dimensional case ($d=0$) without any molecular distribution. The moments correcting for the molecular distribution are therefore put to unity, which yields the correct estimation (see Section 5.2.2).

In Fig. 5.17 (a) N molecules of equal intensity are hypothetically superposed at the same point. The accuracy of the estimation decreases for higher number of superposed molecules and improves for low rate ratios corresponding to Section 5.2.5. The rate ratio is estimated according to Equation (5.20) for a 3D molecular distribution. However, the molecules are on a

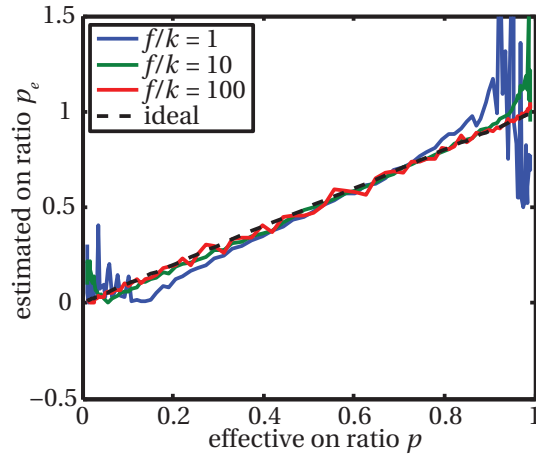


Figure 5.16: Estimated on ratio p_e in function of the simulated on ratio p of a single molecule for different acquisition oversampling factors f/k , where f is the frame rate and k the mean blinking rate. Acquisition length: 100000 frames; SNR = 27dB; extraction according to Equation (5.21)).

single point, which is a zero-dimensional distribution. As a result, there is a small bias barely visible in Fig. 5.17 (a) for the on ratios $p < 0.1$ and $p > 0.9$. This bias is more visible in Fig. 5.17 (b) for a single molecule ($N = 1$).

In the Fig. 5.17 (b), the additional molecules are uniformly distributed in three dimensions. For more than 10 molecules, the bias vanishes confirming the correcting moments for three dimensions ($d = 3$). After all, the bias remains small ($\Delta p < 0.05$).

Estimation of molecular brightness and density

Besides the rate ratio, also the molecular brightness and density is estimated by Equation (5.19). Figure 5.18 (a) shows the estimation of the brightness of two molecules of different intensity. The simulation demonstrates that rather the intensity of the brightest molecule is estimated, and the others are ignored if the rate ratio is the same. The same holds for the rate ratio: the molecule closer to a rate ratio $r = 1$ gets more weight (data not shown). This effect is the reason why the estimation of the number of molecules works well only when the intensities of the molecules are equal at the point of interest. In this case, the estimation up to about five molecules is possible (Fig. 5.18 (b)). The molecules are counted as long as they are within the detection range with respect to their SNR. In general, the estimation of the molecular brightness and the density is much less accurate than the rate ratio estimation.

The estimation of the three parameters is summarized on a simulated grid of molecules with different brightness, rate ratio and density (Fig. 5.19). While on the mean intensity image already the limited resolution even hinders the recognition of a denser structure, the three cumulant imaging parameters reveal more information encoded temporally in the image

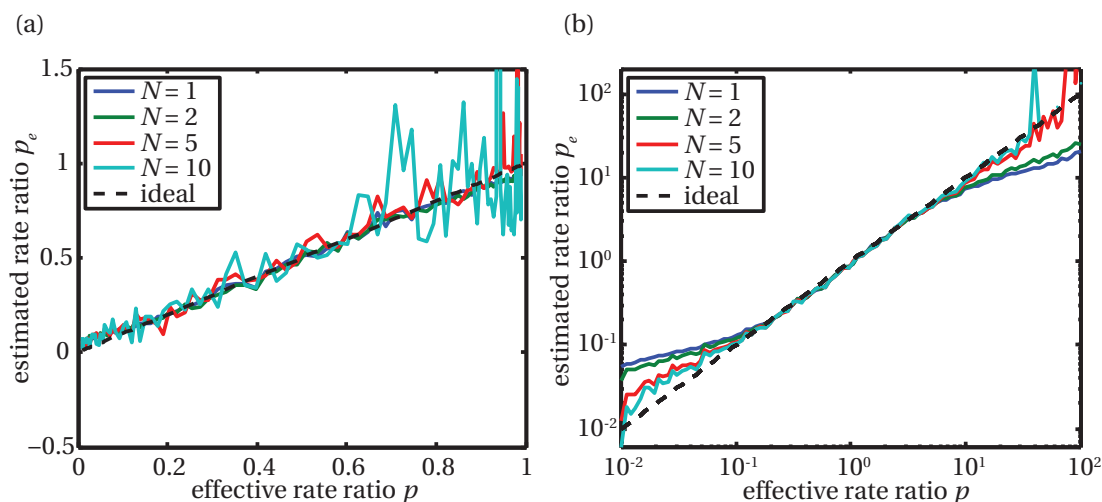


Figure 5.17: Influence of several superposed molecules on the estimation of the rate ratio (a) without and (b) with spatial distribution. The rate ratio is estimated according to the 3D case (Equation (5.21)). (b) In the three dimensional molecular distribution the bias vanishes for more than ≈ 10 molecules (see Section 5.2.2).

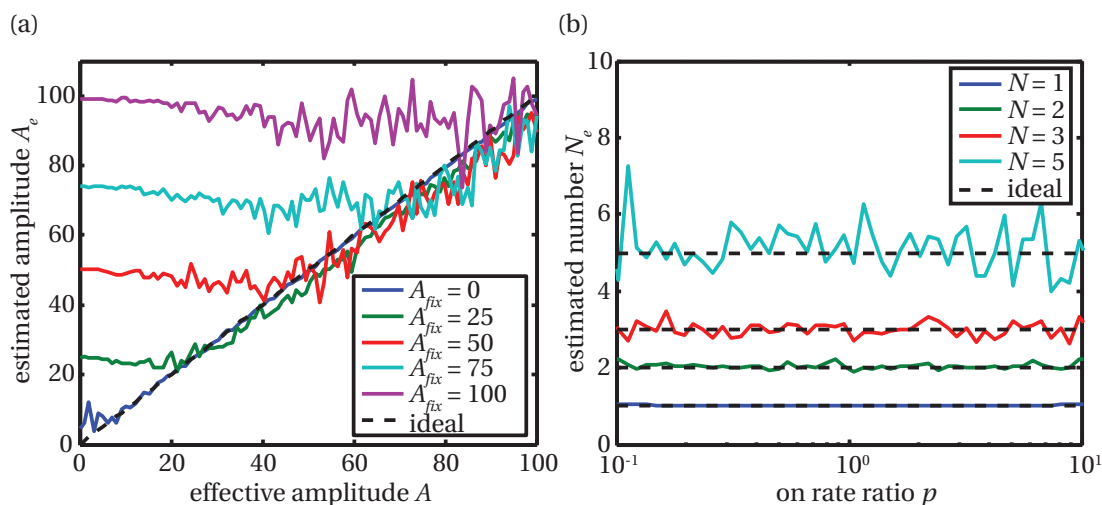


Figure 5.18: (a) Estimation of the molecular brightness A_e for two superposed molecules with the same rate ratio $r = 1$ and different intensity A and A_{fix} . The molecule with the higher intensity is predominant. Acquisition length: 10000 frames. (b) The estimation of the number of molecules N_e of N superposed molecules with equal brightness as a function of their on rate p . Acquisition length: 100000 frames; background: 20 counts; extraction according to Equation (5.21)).

sequence. The brightness decreases from the left to the right while the density of the grid increases. At the same time the rate ratio is decreased from the top to the bottom.

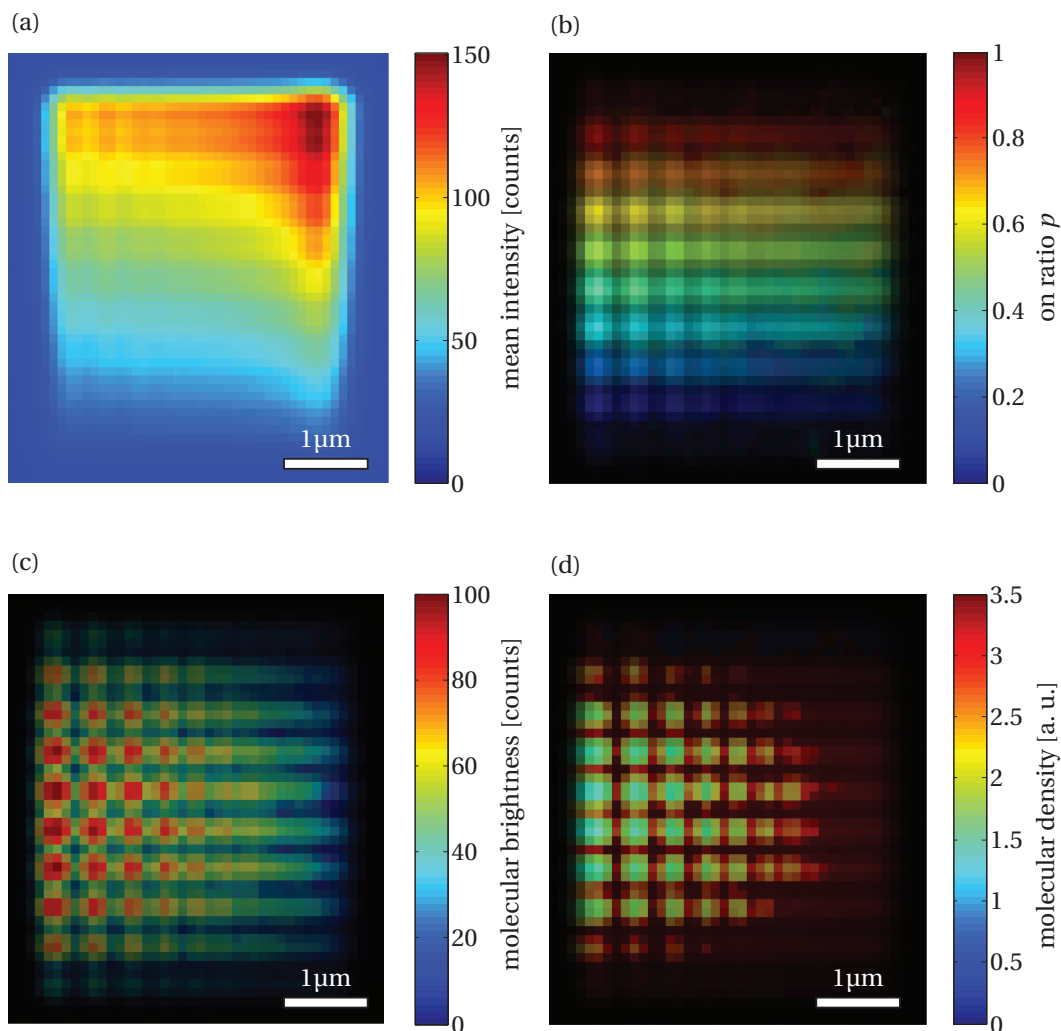


Figure 5.19: A simulated grid of molecules with different rate ratios and intensities. **(a)** the mean image of the image sequence. **(b)** The on ratio p increases from the bottom to the top. **(c)** The molecular brightness decreases from the left to the right. **(d)** The spacing decreases from the left to the right and thus the density (number of molecules) increases. In **(b-d)** the brightness of the second order cumulant is overlaid by a color code visualizing the on ratio, the molecular brightness and density. Acquisition length: 1000 frames, SNR = 27dB.

5.5 Experimental results

5.5.1 SOFI

The experiments with microtubule structures of human osteosarcoma cells (U2OS) showed significant resolution and contrast enhancements for both STORM and SOFI in comparison to the wide-field image (Fig. 5.20). Regions of low microtubule density led to well resolved STORM images (e3), whereas the imaging of crossing structures, or regions of high labeling densities, was more problematic due to rarely isolated single emitter patterns (e2). Apparently, the rate ratio was not sufficiently high in these regions. The third order SOFI image reveals the presence of two closely spaced microtubuli at the pointing arrow in (c2). SOFI worked consistently all over the image up to order three. At higher orders, dimmer and/or weakly

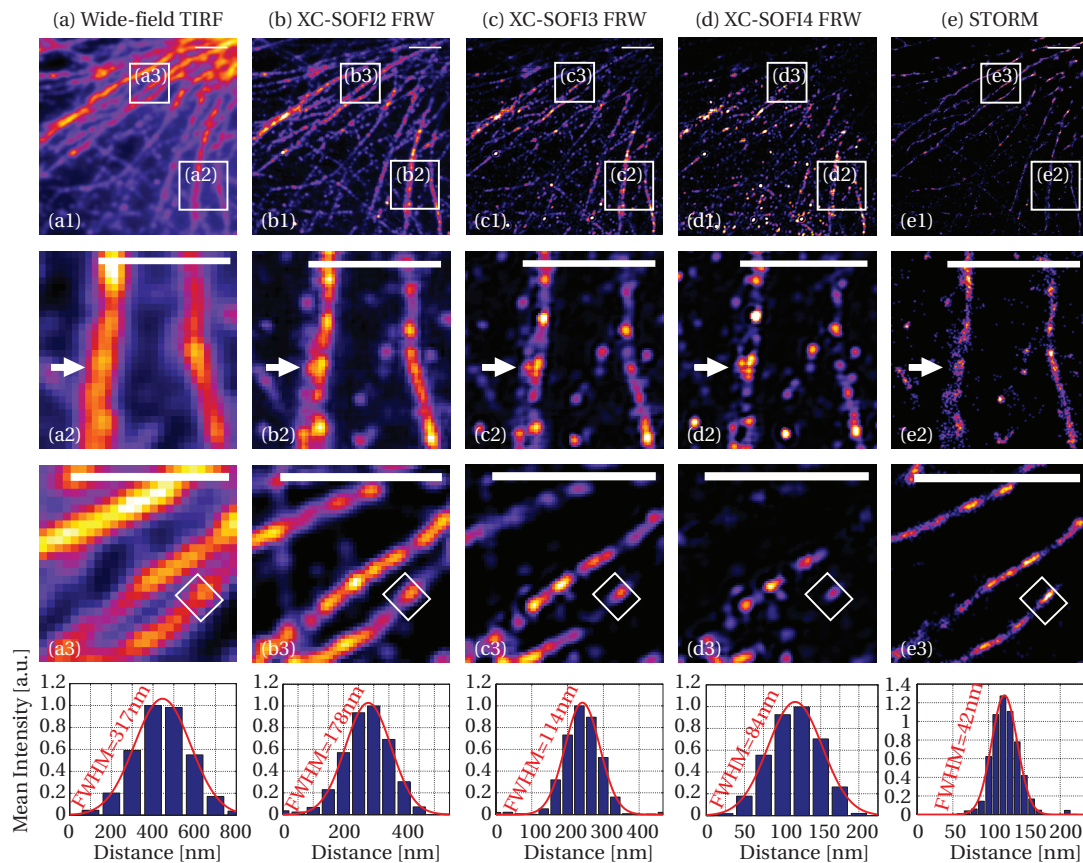


Figure 5.20: Microtubule structures in human osteosarcoma cells: Experimental demonstration of resolution improvements for SOFI and STORM. **Row 2** illustrates the effect of insufficient rate ratios at high labeling densities, which makes it impossible for STORM to resolve the two closely spaced microtubuli at the pointing arrow. Regions of well-separated structures are less problematic (**row 3**). **Row 4** shows the transversal intensity distribution of a microtubule (white box in row 3) fitted to a Gaussian. The intensity distribution is averaged over a length of 400 nm along the structure. *Scale bars: 2 μ m*

fluctuating molecules get lost in the background, and the imaged structures lose connection (see Fig. 5.20(b-d)). This is mainly due to the fact that SOFI order n raises the heterogeneities in molecular brightness to the power of n , which makes it increasingly difficult to display continuous structures for higher orders without compromising the apparent resolution.

The last row in Fig. 5.20 shows the transversal intensity distributions and FWHMs of a single microtubule, averaged over 400 nm along the structure.

5.5.2 Cumulant imaging

The application of cumulant imaging to quantum dots demonstrate the efficient extraction of a broad distribution of blinking rates. Interestingly, some quantum dots appear to change their rate ratio in subsequent image sequences (see Fig. 5.21).

The application of cumulant imaging on the image sequences of microtubule structures in human osteosarcoma cells reveals a spatial distribution of the rate ratio (Fig. 5.22). In contrast to quantum dots, organic dyes show bleaching. In cumulant imaging this modifies the rate ratio because the bleaching is interpreted as a blinking with a very long cycle time pulling the overall rate ratio down. To reduce the influence of bleaching, cumulant imaging was applied to short image sequences (500 frames) only and averaged over 10 subsequent image series to get a final image. For a sequence length shorter than 500 frames (25 s), the reactivation intensity variations are larger than the overall bleaching (see Fig. 4.14). Therefore we assume that the switching prevails over bleaching. This is confirmed by the fact that even shorter

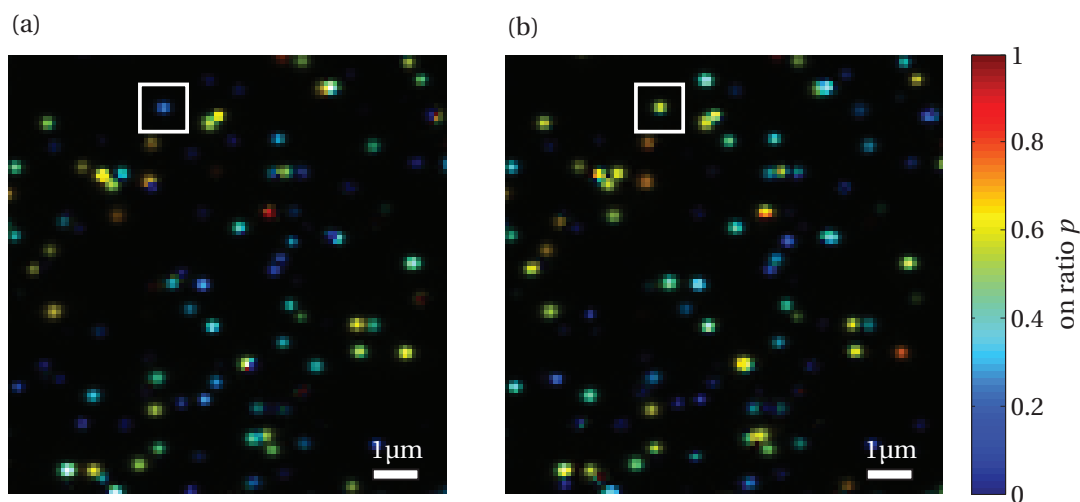


Figure 5.21: Cumulant imaging of quantum dots in air dried on a microscopy cover slip. (a) and (b) are subsequently acquired on the same region. The white square shows a quantum dot changing the rate ratio, what appeared to be a typical behavior for quantum dots. The brightness of the second order cumulant is overlaid by a color code visualizing the on ratio. Excitation wavelength at 490 nm.

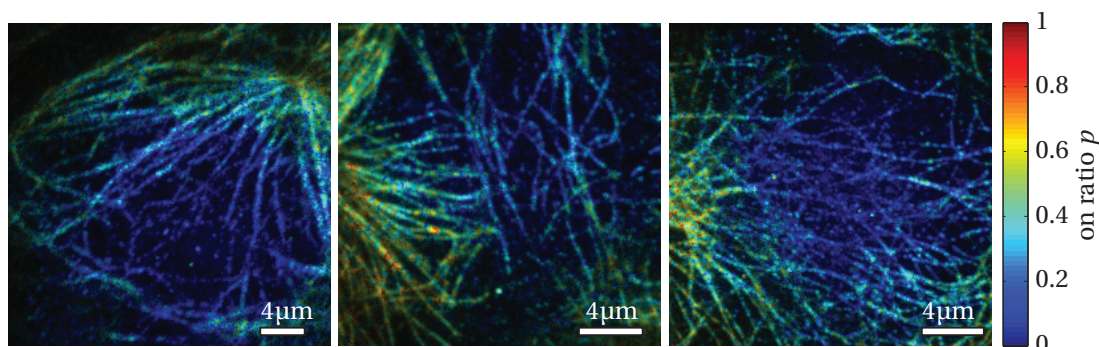


Figure 5.22: Cumulant imaging of microtubule structures in human osteosarcoma cells shows the distribution of on ratios. The non-uniform illumination explains probably this distribution. For each image, the best STORM images resulted from the center of the field of view, where a low on ratio is observed along with a high excitation intensity. A similar effect could be expected by a variation of the oxygen concentration. The brightness of the second order cumulant is overlaid by a color code visualizing the on ratio.

image sequences yield the same rate ratio distribution. Processing short image sequences, however, results in a reduced resolution improvement. This could be addressed by including non-zero time lags in the algorithm to reduce the effect of bleaching.

The cumulant images of the on rate p (see Equation (5.13)) in Fig. 5.22 show a low rate ratio in the middle of the imaged region. At the same time, we found that the localization algorithm (STORM) works best in those regions. This supports the suggestion to use cumulant imaging for judging whether localization algorithms are applicable and for combining eventually SOFI with STORM. This could be an important tool for users of a STORM microscope to avoid localization artifacts.

The reason for a lower rate ratio in the middle of the imaged region is probably the higher probe laser intensity resulting in short bright states before returning over the triplet state to the long-lived dark state. It indicates that the probe laser intensity was at the lower limit for proper STORM imaging.

5.6 Discussion

In order to ensure effective resolutions well below the diffraction limit, very high labeling densities are needed. According to the Nyquist-Shannon sampling theorem [112], the average distance between neighboring fluorescent molecules attached to a structure of interest must not exceed half of the desired resolution. For STORM, diffraction patterns of individual emitters have to appear isolated, which implies the necessity of very stable and long-lived dark states, respectively high rate ratios. This can be achieved using high irradiation intensities and special chemical buffers with thiol compounds and oxygen removal. As a consequence, the ap-

plicability on living organisms is limited [43]. In the case of SOFI, the requirements concerning blinking and labeling density are more relaxed. The basic prerequisite is to have stochastically and independently fluctuating light emitters with a temporally resolvable blinking, which may be achieved without or with less toxic imaging buffers and a variety of probes. Unlike localization microscopy, where one has to wait until each emitter appeared isolated at least once in the image sequence, the information of multiple overlapping emitters can be captured simultaneously and hence suggests a reduced total acquisition time. Furthermore, localization requires a relatively high pSNR of at least 20dB. As we have seen from the simulations, this limit is much lower for SOFI, which allows a significantly increased acquisition rate.

Concerning the possible effective resolution improvements, STORM usually outperforms SOFI provided that the requirements are met for a specific sample. Although by computing higher-order SOFI images a similar resolution enhancement should theoretically be possible, there are a number of factors limiting the maximum order. The presence of heterogeneities in blinking statistics and fluorescence intensities usually leads to discontinuities in the image structures when going beyond the 4th order, as we have seen in the experiments. While the information content is conserved even in higher-orders, visualizing nonlinear intensity distributions without compromising the apparent resolution is difficult. Additional limitations of the maximum order are the computational effort and the number of frames required, which both increase significantly with the SOFI order. Also, when using cross-cumulant combinations without repetitions, one should ensure that only a neighborhood within the PSF is considered, as seen in Fig. 5.12(b). Furthermore, if the noise contributions become stronger, Fourier reweighting starts to fail at higher orders [20]. To address these issues and to increase the final resolution, SOFI might be improved by integrating over several time lags and/or averaging over multiple cross-cumulant combinations to further reduce noise and equalize blinking heterogeneities. Also the visualization may be improved, e.g. by using colormaps that are specifically adapted to SOFI imaging.

Another important property of SOFI is its strong, inherent optical sectioning by suppressing weakly fluctuating out-of-focus signal. This may be suitable for bright-field illumination and 3D imaging over a large depth range. On the contrary, localization microscopy usually needs TIR illumination or an additional means of optical sectioning, such as spinning-disk confocal illumination, in order to avoid an increased overlapping of single emitters and to ensure a correct functioning of the algorithm. However, the localizations may then even be performed in 3D using a more accurate PSF model, and/or a modified optical system generating an engineered PSF that is more sensitive to changes in the axial position. This enables the reconstruction of a 3D rendering, out of a 2D data acquisition, whereas in SOFI one has to scan axially to render 3D data.

The estimation of the rate ratio shows promising results, at least if there is no bleaching. Even with an acquisition rate close to the blinking rate, rate ratios within two to four orders of magnitude are estimated accurately. The algorithm works more accurately for low concentrations or for sparsely labeled samples. The molecular brightness and the number of molecules detected

per pixel are extracted at the same time. Those values are less reliable, but retrieve nevertheless valuable supplementary information on the sample, even though with a rather qualitative character. Photobleaching is the most critical parameter since it falsifies the measurement. A bleaching event is interpreted by the algorithm as the switch from the on state to the off state. In addition, the bleaching is somewhat correlated between the molecules limiting also the resolution enhancement. The different time scale of the bleaching compared to the blinking is not distinguished by cumulants with zero time lag. The extension to non-zero time lags is conceivable, though.

5.7 Conclusion & Outlook

In this chapter, we compared two post-processing algorithms for super-resolution microscopy, STORM and SOFI. Both techniques can be readily applied to standard fluorescence microscopes. We showed that localization microscopy with photo-switchable probes requires highly stable dark states and thereby imposes significant constraints on the sample preparation for successful application in living cells. SOFI can relax those constraints and proved its potential as an attractive alternative to localization microscopy because it works consistently over a wide range of blinking statistics and tolerates much lower SNRs, which reveals its potential for high-speed super-resolution microscopy. Furthermore, the inherent optical sectioning property of SOFI enables 3D imaging without modifying the optical setup.

In extension to the super-resolution capability of SOFI, we showed by simulations and measurements that cumulant imaging can be used to determine the blinking statistics, molecular density and brightness. Hence, cumulant imaging offers the possibility of microenvironmental sensing of chemical agents changing the blinking characteristics. In addition to the rate ratio, molecular concentration and brightness, the characteristic blinking times could be extracted by using cumulants with non-zero time lags.

To estimate the effective resolution of STORM, it is necessary to identify the photo-switching kinetics and labeling densities. If the sample requirements are met according to the evaluation of the blink statistics by cumulant imaging, localization microscopy can be applied and delivers the highest resolution in state-of-the-art wide-field light microscopy.

Altogether, SOFI is an attractive and straightforward approach to fast 3D super-resolution imaging of biological samples. In addition, cumulant imaging offers a novel functional super-resolution imaging technique. It could be an interesting tool for STORM users to judge whether the localization algorithm is applicable or not, which helps to avoid localization artifacts.

6 Conclusion & Outlook

A novel functional super-resolution imaging technique has been conceived by merging concepts of state-of-the-art single molecule microscopy and spectroscopy. By approaching this goal, single molecule investigations have led to contributions in both domains: Fluorescence correlation spectroscopy (FCS) provided the means for a refined understanding of molecular diffusion in highly confined spaces and super-resolution microscopy was enhanced by advanced labeling techniques and a thorough analysis of single molecule blink statistics.

Using FCS, surface interactions of charged proteins at charged interfaces were studied in nanochannels providing a better understanding of surface effects and of the impact of pH and ionic concentration. The concept of the electrical double layer was employed to develop a model quantifying the influence of the ionic concentration on the molecular diffusion. This model was confirmed by the analysis of triplet state lifetime and population indicating surface interactions. The model explains that an almost free protein diffusion is possible at an optimal ionic concentration, below and above which surface interactions are predominant. At very low concentrations, proteins are excluded from the nanochannel.

Further studies on other proteins would increase the value of the developed model. The major challenge of the nanochannel diffusion investigations were the low SNR due to background from autofluorescence of the nanochannel and sticking molecules at the interfaces. This flaw could be addressed at least partially by a redesign of the nanochannel for the use with high NA objectives to get more fluorescence signal. Moreover, a balanced detection with two APDs would then yield a more accurate triplet state analysis. For all measurements, particular attention had to be paid to the temporal degradation of low ionic concentrations.

The outcome of the investigations in nanochannels paved the way to a biomedical application: Nicolas Durand founded Abionic, a startup with the goal to speed up the personalized allergy diagnostics. Besides the need of now only a small blood sample quantity, the nanochannel enhances the molecular identification of antibodies by the selective binding at the nanochannel surfaces. In addition, the reduced axial dimension rejects background and enables single

Chapter 6. Conclusion & Outlook

molecule sensitivity. This application is an example showing the impact of understanding the molecular diffusion in nanochannels.

New super-resolution microscopy concepts based on the localization of single photo-switchable or intrinsically blinking molecules have emerged after the introduction of STED in 1994 and have been a fundamental step forward in fluorescence microscopy. The underlying concept of those super-resolution methods is that the limited spatial transmission bandwidth of the optical system is extended by separate channels to transmit additional object information encoding super-resolution. This can be the time dimension as is the case for STED, structured illumination or localization microscopy.

A similarity of super-resolution techniques is also the increasing significance of the distance between fluorescent emitter and target molecule, when the distance approaches the effective resolution of the technique. We have addressed this issue by using SNAP-tag labeling and demonstrated its performance by combining it with STORM imaging achieving a localization precision down to ≈ 10 nm. This labeling technique with a short linker (≈ 2.5 nm) and small markers offers the advantage of a large choice of bright and stable organic dyes in contrast to weaker fluorescent proteins and can potentially be used to label living cells.

Despite the relatively large choice of switchable organic dyes, the photo-physical requirements of STORM are limiting elements for labeling and live cell imaging because often a toxic imaging buffer is needed. For a proper functioning of localization based methods, a careful match of the labeling density along with corresponding blinking statistics is crucial. Otherwise, localization microscopy may produce misleading artifacts that are difficult to identify in the final image. In physiological environment, the ideal STORM label should therefore provide low bleaching and highly stable long-lived dark states with intense photon bursts in the bright state to achieve a high localization precision (short fluorescence lifetime). Moreover, the minimally invasive label should be attached with a short linker to the target molecule as provided by the SNAP-tag labeling technique.

SOFI, as an alternative concept to localization microscopy, suffers less from those constraints, although it is based as well on “time-multiplexing” the spatial super-resolution information by fluorescence intermittency. SOFI needs reversibly blinking molecules, but is applicable on a much wider range of blink statistics and does not need any objective nor subjective threshold settings. If the blinking requirements cannot be satisfied, instead of introducing artifacts, the SOFI image will just not provide the expected resolution improvement. In contrast to localization based methods, SOFI supplies additionally an intrinsic axial optical sectioning and resolution improvement.

SOFI achieves a resolution improvement with a pSNR about 45-times lower than what is needed for localization microscopy. Hence, even the stochastic intensity fluctuations due to the triplet state should be exploitable. Assuming a constant triplet lifetime, the bright state ratio can be influenced and adjusted by the excitation intensity. Typically between 200 and 1000 photons are emitted per molecule and dark state cycle, about 1 – 10% of which are

detected. This should yield a pSNR high enough to improve the resolution with SOFI based on the triplet state induced intensity fluctuations. An insufficient time-resolution of the detector could be circumvented by pulsed excitation with a preceding laser pulse for triplet population build-up.

The nonlinear response to the sample brightness makes the representation and the interpretation of SOFI images unconventional and sometimes difficult. Among others, this can be addressed by cumulant imaging. In extension to super-resolution imaging and similar to FCS investigations, SOFI provides information about the molecular blinking, brightness and density. Cumulant imaging derived from SOFI can take advantage of the estimated parameter maps to correct for the nonlinear brightness response. In addition, if in a certain region the blink statistics are favorable for localization algorithms, they can be applied to yield the highest resolution in state-of-the-art wide-field light microscopy. Furthermore, the extraction of those molecular parameters by cumulant imaging opens the way towards *functional* super-resolution imaging. As observed in the STORM measurements, the oxygen concentration strongly influences the blink statistics. By analyzing the blink statistics using cumulant imaging, the oxygen consumption in mitochondria may be monitored with high resolution and contrast. To apply cumulant imaging efficiently to a biological sample, the bleaching should be minimized and/or the SOFI algorithm adapted, for example by taking the average cumulant images of multiple short sequences or using non-zero time lags.

Super-resolution based on cumulant analysis has the potential to go even a step further. A single photon emitted by a single molecule can only be detected on one pixel, but not on another neighboring pixel. Preliminary simulation results show, that the resulting spatial anti-correlations, or in general anti-cumulants, could be used to improve the resolution on a fundamental level. Since for this quantum SOFI only the inherent physical property of light is used, the requirements on the fluorescent molecule are minimal and the concept might even work for scattered light when using incoherent illumination at very low light intensity. The challenge of this method lies more on the side of the detector hardware.

In summary, this work contributed in two domains based on single molecule sensing. First, the characterization of protein diffusion in nanochannels has led to a biomedical application in allergy diagnostics. Second, super-resolution microscopy was refined by an advanced labeling technique and finally the thorough statistical analysis and interpretation of molecular blinking conclude with a novel functional super-resolution concept called cumulant microscopy.

A Cumulants and Higher Order Statistics

A.1 Definitions

Moments $\mu_n(X)$ give a description of a probability distribution of the random variable X with a probability density function $f(x)$. The moment of the order n is defined as

$$\mu_n(X) = \mathbb{E}\{X^n\} = \int_{-\infty}^{\infty} x^n f(x) dx, \quad (\text{A.1})$$

where

$$\mathbb{E}\{X\} = \int_{-\infty}^{\infty} x f(x) dx \quad (\text{A.2})$$

is the expectation value of the random variable X . The characteristic function of a random variable is defined as

$$\phi_X(t) = \mathbb{E}\{e^{itX}\} = 1 + \sum_{n=1}^{\infty} \mu_n(X) \frac{(it)^n}{n!} = \int_{-\infty}^{\infty} e^{itx} f_X(x) dx = \hat{f}_X(-t) \quad (\text{A.3})$$

and is related to the Fourier transform of the probability density function f_X . Due to linearity of the derivative, the moments $\mu_n(X)$ can be derived from the characteristic function $\phi_X(t)$ as

$$\mu_n(X) = (-i)^n \left. \frac{d\phi_X(t)}{dt} \right|_{t=0}. \quad (\text{A.4})$$

The moment of the sum of two random variables X and Y is in general not equal to the sum of the moments of X and of Y . This is deduced from

$$\phi_{X+Y}(t) = \mathbb{E}\{e^{it(X+Y)}\} \neq \phi_X(t) + \phi_Y(t) = \mathbb{E}\{e^{itX}\} + \mathbb{E}\{e^{itY}\} = \mathbb{E}\{e^{itX} + e^{itY}\} \quad (\text{A.5})$$

Appendix A. Cumulants and Higher Order Statistics

and the linearity of (A.3) and (A.4) with respect to X and Y .

The second characteristic function or cumulant generating function corresponds to the natural logarithm of the characteristic function:

$$\psi_X(t) = \ln(\phi_X(t)) = \ln\left(\mathbb{E}\{e^{itX}\}\right). \quad (\text{A.6})$$

For independent random variables X and Y , the cumulant generating function is additive:

$$\begin{aligned} \psi_{X+Y}(t) &= \ln\left(\mathbb{E}\{e^{it(X+Y)}\}\right) = \ln\left(\mathbb{E}\{e^{itX}\}\mathbb{E}\{e^{itY}\}\right) \\ &= \ln\left(\mathbb{E}\{e^{itX}\}\right) + \ln\left(\mathbb{E}\{e^{itY}\}\right) = \psi_X(t) + \psi_Y(t). \end{aligned} \quad (\text{A.7})$$

Similar to moments, cumulants $\kappa_n(X)$ are defined as

$$\kappa_n(X) = (-i)^n \left. \frac{d\psi_X(t)}{dt} \right|_{t=0}, \quad (\text{A.8})$$

which is equal to

$$\psi_X(t) = \sum_{n=1}^{\infty} \kappa_n(X) \frac{(it)^n}{n!}. \quad (\text{A.9})$$

As their name suggests, cumulants are additive due to the additivity of (A.7) and (A.8).

A.2 Properties of Cumulants

From the definitions above, some important properties are deduced (for proofs see [80, 90])

1. If β and λ are constants and $\{X_i\}$ random variables, then

$$\kappa(\beta + \lambda X_1, \dots, \beta + \lambda X_n) = \lambda^n \kappa(X_1, \dots, X_n) \quad \forall n > 1. \quad (\text{A.10})$$

2. If the random variables $\{X_i\}$ are independent of the random variables $\{Y_i\}$, then

$$\kappa(X_1 + Y_1, \dots, X_n + Y_n) = \kappa(X_1, \dots, X_n) + \kappa(Y_1, \dots, Y_n) \quad \forall n. \quad (\text{A.11})$$

3. If any subset of $\{X_1, \dots, X_n\}$ consists of independent random variables, then

$$\kappa(X_1, \dots, X_n) = 0 \quad \forall n > 1. \quad (\text{A.12})$$

A.3 Determination of Cumulants

Cumulants are closely related to moments, which are easier to compute. Cumulants are obtained by substituting (A.9) and (A.3) in (A.6). We find

$$\kappa_n = \mu_n - \sum_{m=1}^{n-1} \binom{n-1}{m-1} \kappa_m \mu_{n-m}. \quad (\text{A.13})$$

For zero-mean random variables, the cumulants of the first four orders are

$$\begin{aligned} \kappa_1 &= \mu_1 = 0 \\ \kappa_2 &= \mu_2 \\ \kappa_3 &= \mu_3 \\ \kappa_4 &= \mu_4 - 3\mu_2^2 \\ &\vdots \end{aligned}$$

These definitions can be generalized to multivariate distributions by substituting X and t by the vectors $\mathbf{X} = (X_1, \dots, X_n)$ and $\mathbf{t} = (t_1, \dots, t_n)$ and using the inner product instead. Multivariate cumulants can be calculated directly [80, 90] or recursively [116] from the corresponding and lower order moments. The direct calculation yields

$$\kappa(X_1, \dots, X_n) = \sum_{\Pi} (-1)^{|\Pi|-1} (|\Pi| - 1)! \prod_{B \in \Pi} \mathbb{E} \left\{ \prod_{i \in B} (X_i) \right\}, \quad (\text{A.14})$$

where Π runs through the list of all partitions of $\{1, \dots, n\}$, B runs through the list of all parts of the partition Π , and $|\Pi|$ is the number of parts in the partition. For zero-mean random variables, the cumulants of the first four orders are

$$\begin{aligned} \kappa(X_1) &= \mathbb{E}\{X_1\} = 0 \\ \kappa(X_1, X_2) &= \mathbb{E}\{X_1 X_2\} \\ \kappa(X_1, X_2, X_3) &= \mathbb{E}\{X_1 X_2 X_3\} \\ \kappa(X_1, X_2, X_3, X_4) &= \mathbb{E}\{X_1 X_2 X_3 X_4\} - \mathbb{E}\{X_1 X_2\} \mathbb{E}\{X_3 X_4\} \\ &\quad - \mathbb{E}\{X_1 X_3\} \mathbb{E}\{X_2 X_4\} - \mathbb{E}\{X_1 X_4\} \mathbb{E}\{X_2 X_3\}. \\ &\vdots \end{aligned} \quad (\text{A.15})$$

A.4 Bernoulli Distribution

The Bernoulli distribution $X \sim P(p)$ describes a process with two states 0 and 1 with the probability p to be in the state 1. The moments of a Bernoulli distribution are

$$\mu_n(X) = p \forall n. \tag{A.16}$$

The first four cumulants and the recursion formula are

$$\begin{aligned} \kappa_1(X) &= p \\ \kappa_2(X) &= p(1-p) \\ \kappa_3(X) &= p(1-p)(1-2p) \\ \kappa_4(X) &= p(1-p)(1-6p(1-p)) \\ &\vdots \\ \kappa_n(X) &= p(1-p) \frac{d\kappa_{n-1}(X)}{dp}, \end{aligned} \tag{A.17}$$

B Photo-Physical Properties of Alexa Fluor 633, Cy3 and Cy5

The fluorescent probes used for our measurements were Cy3, Cy5 and Alexa Fluor 633 from Molecular Probes. Their photo-physical properties are summarized in Table B.1.

Fluorophore	Abs./Em. ^a	η^b	q_f^c	ϵ^d	$\tau_{S_1}^e$	τ_t^f	k_{isc}^g	References
Cy5	652/672	0.18	0.58	2.5	1.0	2	0.9	MP, [93, 25]
Cy3	554/568	0.14	0.6	1.3	0.3	n. a.	n. a.	ISS, [93]
Alexa Fluor 633	632/647	n. a.	0.99	1.0	3.2	≈ 4.3	0.4	[53, 76]

^a Absorption / Emission maxima [nm]

^b Excitation efficiency with a Helium–Neon laser (at 633 nm) and an Argon laser (at 514 nm for Cy3)

^c Fluorescence quantum yield

^d Molar extinction coefficient ϵ for the wave length of the absorption maxima [$\times 10^5 \text{cm}^{-1} \text{M}^{-1}$]; related to the absorption cross section σ by $\epsilon = N_A \sigma \log_{10}(e)$, where $N_A = 6.022 \cdot 10^{23}$ is the Avogadro constant.

^e Lifetime of first excited singlet state S_1 [ns]

^f Lifetime of first excited triplet state T_1 [μs]

^g Intersystem crossing rate $k_{isc} = 1/\tau_{isc} (S_1 \rightarrow T_1)$ [μs]

MP: stands for Molecular Probes <http://www.invitrogen.com/> ISS: <http://www.iss.com/>

Table B.1: Photo-physical properties of Alexa Fluor 633, Cy3 and Cy5.

These values allow to determine the theoretical molecular emission rates R_f (Equation (2.4)):

$$R_f = \frac{q_f}{\tau_c} = \frac{q_f}{\frac{1}{\sigma I_{ex}} + \tau_{S_1} (1 + \tau_t k_{isc})}, \quad (\text{B.1})$$

where I_{ex} is the excitation intensity. In the case of the excitation of Cy5 by a Gaussian wide-field illumination on an area of $430 \mu\text{m}^2$ at 633 nm with 2.5 mW, we find a mean emission rate of $R_f = 290 \text{kHz}$.

The saturation intensity is

$$I_{sat} = \frac{hc/\lambda}{\sigma \tau_{S_1} (1 + \tau_t k_{isc})}, \quad (\text{B.2})$$

Appendix B. Photo-Physical Properties of Alexa Fluor 633, Cy3 and Cy5

where $h = 6.626 \cdot 10^{-34} \text{ m}^2 \text{ kg s}^{-1}$, $c = 3 \cdot 10^8 \text{ m s}^{-1}$ and λ are the Planck constant, the speed of light in free space and the excitation wavelength, respectively. For Cy5 and Alexa Fluor 633 we find $I_{sat}(\text{Cy5}) \approx 1 \text{ GW m}^{-1}$ and $I_{sat}(\text{Alexa 633}) \approx 0.2 \text{ GW m}^{-1}$, respectively, if excited at their absorption maxima. Considering the excitation at 633 nm, the saturation intensity of Alexa Fluor 633 is about 8 times lower than the one of Cy5.

Acknowledgements

The openminded and stimulating atmosphere is one of the strengths of the LOB, in which laboratory I was privileged to conduct my thesis. I highly appreciated this atmosphere all over the four years of collaboration and I think it is one of the key ingredients to success. For this quality I would like to thank my thesis director and professor of LOB, Theo Lasser, who is looking to the team like a father. His enthusiasm, not only to achieve good results, but also to forge his PhD students almost like his own children is admirable. At this point, I would like to express my gratitude to all LOB members, for their contribution to the inspiring and relaxed atmosphere, where fun is always part of it. Part of it were also non-scientific discussions having a beer with Arno Bouwens, Akihiro Sato and Sergiy Mayilo.

In particular I want to thank my office mates, Martin Viliger, Christophe Pache and Corinne Berclaz, with whom I could share many moments, pleasant and difficult ones. Thanks to Martin's squash balls and Christophe's Claudio game, we managed to overcome any situation. Especially with Christophe, we had many discussions about our common passion, mountaineering, in particular on Mondays and Fridays. I had the chance to spend some leisure time and found a good friend with him. Although rarely present, Corinne was involuntary in charge of the good habits in our office.

I am especially grateful to Stefan Geissbühler for the very motivating collaboration and the many fruitful scientific discussions. Last but not least, I highly appreciated his help during thesis writing. His positive conviction often helped me to overcome also more difficult periods. The lost glasses in the lake I could give him back are only a symbol for my gratitude. Stefan seems to share the positive attitude as well as design and computer skills with his brother Matthias Geissbühler. I admired Matthias' openmindedness, infinite patience, his almost permanent good mood and that he was always available for help.

Many thanks also to Antonio for the hands-on experience in mechanics. Together with Judith Chaubert and her successor Fabienne Ubezio, they organized many out of office events contributing to the good ambience in the lab. Special thanks also to Erica Martin-Williams for the patience to proofread many manuscripts.

I am very grateful also to Iwan Märki, Noelia Bocchio and Marcel Leutenegger, scientifically as well as personally. I honor the patient calm of Iwan as much as the southern power of Noelia.

Acknowledgements

Not only she brought in the missing knowledge in biochemistry, but she learned me many aspects by insisting on scientific and non-scientific qualities. The expertise in optics of Marcel and Iwan led to many pragmatic solution thanks to their permanent availability.

Many special thanks to my colleagues Nicolas Durand, Gražvydas Lukinavičius and Sambashiva Banala. The projects would not have been possible without their collaboration. In uncountable hours we experienced together the highs and lows of research. At this point, I would like to acknowledge also the master and semester students who contributed to this work with my supervision: Thomas Lanvin, Pascal Bérard and above all Raphaël Goetschmann for his patience and endurance for the finally successful FCS nanochannel measurements.

I am infinitely grateful to Jean-Michel Couture. He offered me the invaluable service of proofreading and reviewing the entire thesis work. Many thanks also to Akihiro Sato for his kind support.

I thank Prof. Christophe Moser, Dr. Nathalie Garin, Dr. Toralf Scharf, and Prof. Jörg Enderlein for accepting to be on my thesis committee, and for their comments and feedback.

The principle ingredient to persevere and finish my thesis is outside the lab. I would like to thank the IOA volley ball team and above all Daniel Salzmänn for giving me energy, motivation and good ideas to continue. Many thanks also to the members of the symphonic orchestra OSUL. This activity helped me not to stay too long in the lab and keeping a clear head.

Immense thanks to my room mate and friend Jonathan Grept, for his understanding and support. With him, I enjoyed many hours of hiking and beach volley ball giving me back the needed energy.

Many profound thanks to my family for supporting me and giving me the possibility to study and complete the PhD without expectations.

My deepest gratitude is dedicated to Elisabeth, for her infinite love and endurance to support me constantly.

Bibliography

- [1] F. Aguet, S. Geissbuehler, I. Maerki, T. Lasser, and M. Unser. Super-resolution orientation estimation and localization of fluorescent dipoles using 3-D steerable filters. *Opt Express*, 17(8):6829–6848, 2009.
- [2] F. Aguet, D. V. D. Ville, and M. Unser. A maximum-likelihood formalism for sub-resolution axial localization of fluorescent nanoparticles. *Opt Express*, 13(26):10503–10522, 2005.
- [3] D. Baddeley, M. B. Cannell, and C. Soeller. Visualization of localization microscopy data. *Microsc Microanal*, 16(1):64–72, 2010.
- [4] B. Bailey, D. L. Farkas, D. Taylor, and F. Lanni. Enhancement of axial resolution in fluorescence microscopy by standing-wave excitation. *Nature*, 366(6450):44–48, 1993.
- [5] L. S. Barak and W. W. Webb. Fluorescent low-density lipoprotein for observation of dynamics of individual receptor complexes on cultured human-fibroblasts. *J Cell Biol*, 90(3):595–604, 1981.
- [6] M. Bates, T. R. Blosser, and X. Zhuang. Short-range spectroscopic ruler based on a single-molecule optical switch. *Phys Rev Lett*, 94(10):108101, 2005.
- [7] M. Bates, B. Huang, G. T. Dempsey, and X. Zhuang. Multicolor super-resolution imaging with photo-switchable fluorescent probes. *Science*, 317(5845):1749–1753, 2007.
- [8] E. Betzig, G. H. Patterson, R. Sougrat, O. W. Lindwasser, S. Olenych, J. S. Bonifacino, M. W. Davidson, J. Lippincott-Schwartz, and H. F. Hess. Imaging intracellular fluorescent proteins at nanometer resolution. *Science*, 313(5793):1642–1645, 2006.
- [9] H. Blom, A. Chmyrov, K. Hassler, L. M. Davis, and J. Widengren. Triplet-state investigations of fluorescent dyes at dielectric interfaces using total internal reflection fluorescence correlation spectroscopy. *J Phys Chem A*, pages 1–13, 2009.
- [10] H. Blom, K. Hassler, A. Chmyrov, and J. Widengren. Electrostatic interactions of fluorescent molecules with dielectric interfaces studied by total internal reflection fluorescence correlation spectroscopy. *Int J Mol Sci*, 11(2):386–406, 2010.

Bibliography

- [11] H. Blom, L. Kastrup, and C. Eggeling. Fluorescence fluctuation spectroscopy in reduced detection volumes. *Curr Pharm Biotechno*, 7(1):51–66, 2006.
- [12] N. Bobroff. Position measurement with a resolution and noise-limited instrument. *Rev Sci Instrum*, 57(6):1152–1157, 1986.
- [13] M. Bohmer and J. Enderlein. Orientation imaging of single molecules by wide-field epifluorescence microscopy. *J Opt Soc Am B*, 20(3):554–559, 2003.
- [14] A. Chmyrov, T. Sanden, and J. Widengren. Iodide as a fluorescence quencher and promoter-mechanisms and possible implications. *J Phys Chem B*, 114(34):11282–11291, 2010.
- [15] N. R. Conley, J. S. Biteen, and W. E. Moerner. Cy3-Cy5 covalent heterodimers for single-molecule photoswitching. *J Phys Chem B*, 112(38):11878–11880, 2008.
- [16] H. I. C. Dalgarno, A. Putoud, R. Lambert, L. Paterson, D. C. Logan, D. P. Towers, R. J. Warburton, and A. H. Greenaway. Multiplane imaging and three dimensional nanoscale particle tracking in biological microscopy. *Opt Express*, 18(2):877–884, 2010.
- [17] C. Dellagiacoma, G. Lukinavicius, N. L. Bocchio, S. Banala, S. Geissbuehler, I. Maerki, K. Johnsson, and T. Lasser. Targeted photoswitchable probe for nanoscopy of biological structures. *ChemBioChem*, 11(10):1361–1363, 2010.
- [18] G. T. Dempsey, M. Bates, W. E. Kowtoniuk, D. R. Liu, R. Y. Tsien, and X. Zhuang. Photo-switching mechanism of cyanine dyes. *J Am Chem Soc*, 2009.
- [19] T. Dertinger, R. Colyer, G. Iyer, S. Weiss, and J. Enderlein. Fast, background-free, 3D super-resolution optical fluctuation imaging (SOFI). *P Natl Acad Sci Usa*, 106(52):22287–22292, 2009.
- [20] T. Dertinger, R. Colyer, R. Vogel, J. Enderlein, and S. Weiss. Achieving increased resolution and more pixels with Superresolution Optical Fluctuation Imaging (SOFI). *Opt Express*, 18(18):18875–18885, 2010.
- [21] T. Dertinger, M. Heilemann, R. Vogel, M. Sauer, and S. Weiss. Superresolution optical fluctuation imaging with organic dyes. *Angew Chem Int Edit*, 49(49):9441–9443, 2010.
- [22] T. Dertinger, V. Pacheco, I. von der Hocht, R. Hartmann, I. Gregor, and J. Enderlein. Two-focus fluorescence correlation spectroscopy: a new tool for accurate and absolute diffusion measurements. *ChemPhysChem*, 8(3):433–443, 2007.
- [23] N. F. Y. Durand. Biomolecular diffusion in nanofluidics. thesis, Ecole Polytechnique Fédérale de Lausanne (EPFL), Switzerland, 2010.
- [24] N. F. Y. Durand, C. Dellagiacoma, R. Goetschmann, A. Bertsch, I. Maerki, T. Lasser, and P. Renaud. Direct observation of transitions between surface-dominated and bulk diffusion regimes in nanochannels. *Anal Chem*, 81(13):5407–5412, 2009.

- [25] C. Eggeling, J. Widengren, L. Brand, J. Schaffer, S. Felekyan, and C. A. M. Seidel. Analysis of photobleaching in single-molecule multicolor excitation and forster resonance energy transfer measurement. *J Phys Chem A*, 110(9):2979–2995, 2006.
- [26] J. C. T. Eijkel and A. van den Berg. Nanofluidics: what is it and what can we expect from it? *Microfluid Nanofluid*, 1(3):249–267, 2005.
- [27] E. L. Elson and D. Magde. Fluorescence correlation spectroscopy. I. conceptual basis and theory. *Biopolymers*, 13(1):1–27, 1974.
- [28] J. Enderlein, I. Gregor, D. Patra, and J. Fitter. Art and artefacts of fluorescence correlation spectroscopy. *Curr Pharm Biotechno*, 5(2):155–161, 2004.
- [29] J. Foelling, M. Bossi, H. Bock, R. Medda, C. A. Wurm, B. Hein, S. Jakobs, C. Eggeling, and S. W. Hell. Fluorescence nanoscopy by ground-state depletion and single-molecule return. *Nat Meth*, page 12, 2008.
- [30] A. Gautier, A. Juillerat, C. Heinis, I. Corraejr, M. Kindermann, F. Beaufls, and K. Johnsson. An engineered protein tag for multiprotein labeling in living cells. *Chem Biol*, 15(2):128–136, 2008.
- [31] S. Geissbuehler, C. Dellagiacomma, and T. Lasser. Comparison between SOFI and STORM. *Biomed Opt Express*, 2(3):408–420, 2011.
- [32] A. Gennerich and D. Schild. Fluorescence correlation spectroscopy in small cytosolic compartments depends critically on the diffusion model used. *Biophysj*, 79(6):3294–3306, 2000.
- [33] R. N. Ghosh and W. W. Webb. Automated detection and tracking of individual and clustered cell-surface low-density-lipoprotein receptor molecules. *Biophysj*, 66(5):1301–1318, 1994.
- [34] T. J. Gould, M. S. Gunewardene, M. V. Gudheti, V. V. Verkhusha, S.-R. Yin, J. A. Gosse, and S. T. Hess. Nanoscale imaging of molecular positions and anisotropies. *Nat Meth*, 2008.
- [35] R. L. Graham, D. E. Knuth, and O. Patashnik. Concrete mathematics. Addison-Wesley, Reading, Massachusetts, first edition, 1988.
- [36] M. G. L. Gustafsson. Surpassing the lateral resolution limit by a factor of two using structured illumination microscopy. *J Microsc (Oxf)*, 198:82–87, 2000.
- [37] M. G. L. Gustafsson. Nonlinear structured-illumination microscopy: wide-field fluorescence imaging with theoretically unlimited resolution. *P Natl Acad Sci Usa*, 102(37):13081–13086, 2005.
- [38] J. Haseloff and K. Siemering. The uses of green fluorescent protein in plants. *Methods Biochem Anal*, 47:259–284, 2006.

Bibliography

- [39] K. Hassler, M. Leutenegger, P. Rigler, R. Rao, R. Rigler, M. Gosch, and T. Lasser. Total internal reflection fluorescence correlation spectroscopy (TIR-FCS) with low background and high count-rate per molecule. *Opt Express*, 13(19):7415–7423, 2005.
- [40] E. Haustein and P. Schwille. Fluorescence correlation spectroscopy: novel variations of an established technique. *Annu Rev Bioph Biom*, 36:151–169, 2007.
- [41] E. Haustein and P. Schwille. Trends in fluorescence imaging and related techniques to unravel biological information. *Hfsp J*, 1(3):169–180, 2007.
- [42] M. Heilemann, E. Margeat, R. Kasper, M. Sauer, and P. Tinnefeld. Carbocyanine dyes as efficient reversible single-molecule optical switch. *J Am Chem Soc*, 127(11):3801–3806, 2005.
- [43] M. Heilemann, S. van de Linde, A. Mukherjee, and M. Sauer. Super-resolution imaging with small organic fluorophores. *Angew Chem Int Edit*, 48(37):6903–6908, 2009.
- [44] M. Heilemann, S. van de Linde, M. Schiittpelz, R. Kasper, B. Seefeldt, A. Mukherjee, P. Tinnefeld, and M. Sauer. Subdiffraction-resolution fluorescence imaging with conventional fluorescent probes. *Angew Chem Int Edit*, 47(33):6172–6176, 2008.
- [45] B. Hein, K. I. Willig, C. A. Wurm, V. Westphal, S. Jakobs, and S. W. Hell. Stimulated emission depletion nanoscopy of living cells using SNAP-tag fusion proteins. *Biophysj*, 98(1):158–163, 2010.
- [46] R. Heintzmann, T. M. Jovin, and C. Cremer. Saturated patterned excitation microscopy — a concept for optical resolution improvement. *J Opt Soc Am A*, 19(8):1599–1609, 2002.
- [47] S. W. Hell. Far-field optical nanoscopy. *Science*, 316(5828):1153–1158, 2007.
- [48] S. W. Hell and M. Kroug. Ground-state-depletion fluorescence microscopy: a concept for breaking the diffraction resolution limit. *Appl Phys B*, 60(5):495–497, 1995.
- [49] S. W. Hell and J. Wichmann. Breaking the diffraction resolution limit by stimulated-emission: stimulated-emission-depletion fluorescence microscopy. *Opt Lett*, 19(11):780–782, 1994.
- [50] E. H. Hellen and D. Axelrod. Fluorescence emission at dielectric and metal-film interfaces. *J Opt Soc Am B*, 4(3):337–350, 1987.
- [51] R. Henriques, C. Griffiths, E. H. Rego, and M. M. Mhlanga. PALM and STORM: unlocking live-cell super-resolution. *Biopolymers*, 2011.
- [52] R. Henriques and M. M. Mhlanga. PALM and STORM: What hides beyond the Rayleigh limit? *Biotechnol J*, 4(6):846–857, 2009.
- [53] M. Herget, N. Kreissig, C. Kolbe, C. Schoelz, R. Tampe, and R. Abele. Purification and Reconstitution of the Antigen Transport Complex TAP: a prerequisite for determination of peptide stoichiometry and atp hydrolysis. *J Biol Chem*, 284(49):33740–33749, 2009.

- [54] S. T. Hess, T. P. K. Girirajan, and M. D. Mason. Ultra-high resolution imaging by fluorescence photoactivation localization microscopy. *Biophysj*, 91(11):4258–4272, 2006.
- [55] S. T. Hess and W. W. Webb. Focal volume optics and experimental artifacts in confocal fluorescence correlation spectroscopy. *Biophysj*, 83(4):2300–2317, 2002.
- [56] L. N. Hillesheim and J. D. Muller. The photon counting histogram in fluorescence fluctuation spectroscopy with non-ideal photodetectors. *Biophysj*, 85(3):1948–1958, 2003.
- [57] P. Hinterdorfer and A. V. Oijen. Handbook of single-molecule biophysics. Springer, New York, first edition, 2009.
- [58] M. Hobel and J. Ricka. Dead-time and afterpulsing correction in multiphoton timing with nonideal detectors. *Rev Sci Instrum*, 65(7):2326–2336, 1994.
- [59] J. W. Hong and S. R. Quake. Integrated nanoliter systems. *Nat Biotechnol*, 21(10):1179–1183, 2003.
- [60] M. Horton, F. Höfling, J. Rädler, and T. Franosch. Development of anomalous diffusion among crowding proteins. *Soft Matter*, 6(12):2648–2656, 2010.
- [61] B. Huang, M. Bates, and X. Zhuang. Super-resolution fluorescence microscopy. *Annu Rev Biochem*, 78:993–1016, 2009.
- [62] B. Huang, S. A. Jones, B. Brandenburg, and X. Zhuang. Whole-cell 3D STORM reveals interactions between cellular structures with nanometer-scale resolution. *Nat Meth*, 5(12):1047–1052, 2008.
- [63] B. Huang, W. Wang, M. Bates, and X. Zhuang. Three-dimensional super-resolution imaging by stochastic optical reconstruction microscopy. *Science*, 2008.
- [64] J. Huiskens, J. Swoger, F. D. Bene, J. Wittbrodt, and E. H. K. Stelzer. Optical sectioning deep inside live embryos by selective plane illumination microscopy. *Science*, 305(5686):1007–1009, 2004.
- [65] K. Johnsson. Laboratory of protein engineering. <http://lip.epfl.ch/>, August 2011.
- [66] N. Johnsson and K. Johnsson. Chemical tools for biomolecular imaging. *ACS Chem Biol*, 2(1):31–38, 2007.
- [67] S. Jones, S.-H. Shim, J. He, and X. Zhuang. Fast, three-dimensional super-resolution imaging of live cells. *Nat Meth*, 2011.
- [68] M. F. Juetten, T. J. Gould, M. D. Lessard, M. J. Mlodzianoski, B. S. Nagpure, B. T. Bennett, S. T. Hess, and J. Bewersdorf. Three-dimensional sub-100 nm resolution fluorescence microscopy of thick samples. *Nat Meth*, 5(6):527–529, 2008.

Bibliography

- [69] R. Jungmann, C. Steinhauer, M. Scheible, A. Kuzyk, P. Tinnefeld, and F. C. Simmel. Single-molecule kinetics and super-resolution microscopy by fluorescence imaging of transient binding on dna origami. *Nano Lett*, 10(11):4756–4761, 2010.
- [70] B. Kannan, J. Y. Har, P. Liu, I. Maruyama, J. L. Ding, and T. Wohland. Electron multiplying charge-coupled device camera based fluorescence correlation spectroscopy. *Anal Chem*, 78(10):3444–3451, 2006.
- [71] P. Kask, R. Gunther, and P. Axhausen. Statistical accuracy in fluorescence fluctuation experiments. *Eur Biophys J Biophys*, 25(3):163–169, 1997.
- [72] L. Kastrup, H. Blom, C. Eggeling, and S. W. Hell. Fluorescence fluctuation spectroscopy in subdiffraction focal volumes. *Phys Rev Lett*, 94(17):178104, 2005.
- [73] A. Keppler, C. Arrivoli, L. Sironi, and J. Ellenberg. Fluorophores for live cell imaging of AGT fusion proteins across the visible spectrum. *Biotech*, 41(2):167–175, 2006.
- [74] A. Keppler, S. Gendreizig, T. Gronemeyer, H. Pick, H. Vogel, and K. Johnsson. A general method for the covalent labeling of fusion proteins with small molecules in vivo. *Nat Biotechnol*, 21(1):86–89, 2003.
- [75] A. Keppler, H. Pick, C. Arrivoli, H. Vogel, and K. Johnsson. Labeling of fusion proteins with synthetic fluorophores in live cells. *P Natl Acad Sci Usa*, 101(27):9955–9959, 2004.
- [76] K. Kolmakov, V. N. Belov, J. Bierwagen, C. Ringemann, V. Müller, C. Eggeling, and S. W. Hell. Red-emitting rhodamine dyes for fluorescence microscopy and nanoscopy. *Chem Eur J*, 16(1):158–166, 2010.
- [77] D. E. Koppel. Statistical accuracy in fluorescence correlation spectroscopy. *Phys Rev A*, 10(6):1938–1945, 1974.
- [78] O. Krichevsky and G. Bonnet. Fluorescence correlation spectroscopy: the technique and its applications. *Rep Prog Phys*, 65(2):251–297, 2002.
- [79] M. Kuno, D. P. Fromm, H. F. Hamann, A. Gallagher, and D. J. Nesbitt. Nonexponential “blinking” kinetics of single CdSe quantum dots: A universal power law behavior. *J Chem Phys*, 112(7):3117–3120, 2000.
- [80] V. P. Leonov and A. N. Shiryaev. On a method of calculation of semi-invariants. *Theory Probab Appl*, 4:319, 1959.
- [81] M. Leutenegger, M. Gosch, A. Perentes, P. Hoffmann, O. J. F. Martin, and T. Lasser. Confining the sampling volume for fluorescence correlation spectroscopy using a sub-wavelength sized aperture. *Opt Express*, 14(2):956–969, 2006.
- [82] M. Leutenegger and T. Lasser. Detection efficiency in total internal reflection fluorescence microscopy. *Opt Express*, 16(12):8519–8531, 2008.

- [83] M. Leutenegger, R. Rao, R. A. Leitgeb, and T. Lasser. Fast focus field calculations. *Opt Express*, 14(23):11277–11291, 2006.
- [84] J. W. Lichtman and J. A. Conchello. Fluorescence microscopy. *Nat Meth*, 2(12):910–919, 2005.
- [85] A. Loman, T. Dertinger, F. Koberling, and J. Enderlein. Comparison of optical saturation effects in conventional and dual-focus fluorescence correlation spectroscopy. *Chem Phys Lett*, 459(1-6):18–21, 2008.
- [86] A. Loman, I. Gregor, C. Stutz, M. Mund, and J. Enderlein. Measuring rotational diffusion of macromolecules by fluorescence correlation spectroscopy. *Photochem Photobiol Sci*, 9(5):627–636, 2010.
- [87] S. J. Lord, H.-I. D. Lee, and W. E. Moerner. Single-molecule spectroscopy and imaging of biomolecules in living cells. *Anal Chem*, 82(6):2192–2203, 2010.
- [88] I. Maerki, N. L. Bocchio, S. Geissbuehler, F. Aguet, A. Bilenca, and T. Lasser. Three-dimensional nano-localization of single fluorescent emitters. *Opt Express*, 18(19):20263–20272, 2010.
- [89] D. Magde, E. L. Elson, and W. W. Webb. Thermodynamic fluctuations in a reacting system measurement by fluorescence correlation spectroscopy. *Phys Rev Lett*, 29(11):705–708, 1972.
- [90] J. M. Mendel. Tutorial on higher-order statistics (spectra) in signal processing and system theory: Theoretical results and some applications. *Proc IEEE*, 79(3):278–305, 1991.
- [91] J. Mertz. Radiative absorption, fluorescence, and scattering of a classical dipole near a lossless interface: a unified description. *J Opt Soc Am B*, 17(11):1906–1913, 2000.
- [92] X. Michalet, A. N. Kapanidis, T. Laurence, F. Pinaud, S. Doose, M. Pflughoeft, and S. Weiss. The power and prospects of fluorescence microscopies and spectroscopies. *Annu Rev Bioph Biom*, 32:161–182, 2003.
- [93] R. B. Mujumdar, L. A. Ernst, S. R. Mujumdar, C. J. Lewis, and A. S. Waggoner. Cyanine dye labeling reagents: sulfoindocyanine succinimidyl esters. *Bioconjugate Chem*, 4(2):105–111, 1993.
- [94] J. D. Muller. Cumulant analysis in fluorescence fluctuation spectroscopy. *Biophysj*, 86(6):3981–3992, 2004.
- [95] M. S. Munson, K. R. Hawkins, M. S. Hasenbank, and P. Yager. Diffusion based analysis in a sheath flow microchannel: the sheath flow T-sensor. *Lab Chip*, 5(8):856–862, 2005.
- [96] L. Novotny and B. Hecht. Principles of nano-optics. Cambridge University Press, Cambridge, first edition, 2006.

Bibliography

- [97] R. J. Ober, S. Ram, and E. S. Ward. Localization accuracy in single-molecule microscopy. *Biophysj*, 86(2):1185–1200, 2004.
- [98] H. M. O’Hare, K. Johnsson, and A. Gautier. Chemical probes shed light on protein function. *Curr Opin Struc Biol*, 17(4):488–494, 2007.
- [99] H. Ohshima. Theory of colloid and interfacial electric phenomena. Elsevier/Academic Press, London, first edition, 2006.
- [100] G. H. Patterson, M. W. Davidson, S. Manley, and J. Lippincott-Schwartz. Superresolution imaging using single-molecule localization. *Annu Rev Phys Chem*, 61:345–367, 2010.
- [101] L. Pauling. A theory of the structure and process of formation of antibodies. *J Am Chem Soc*, 62:2643–2657, 1940.
- [102] S. R. P. Pavani, M. A. Thompson, J. S. Biteen, S. J. Lord, N. Liu, R. J. Twieg, R. Piestun, and W. E. Moerner. Three-dimensional, single-molecule fluorescence imaging beyond the diffraction limit by using a double-helix point spread function. *P Natl Acad Sci Usa*, 106(9):2995–2999, 2009.
- [103] P. Renaud. Microsystems laboratory 4. <http://lmis4.epfl.ch/>, August 2011.
- [104] R. Rigler, U. Mets, J. Widengren, and P. Kask. Fluorescence correlation spectroscopy with high count rate and low-background: analysis of translational diffusion. *Eur Biophys J Biophys*, 22(3):169–175, 1993.
- [105] M. S. Robbins and B. J. Hadwen. The noise performance of electron multiplying charge-coupled devices. *IEEE T Nanotechnol*, 50(5):1227–1232, 2003.
- [106] M. J. Rust, M. Bates, and X. Zhuang. Sub-diffraction-limit imaging by stochastic optical reconstruction microscopy (STORM). *Nat Meth*, 3(10):793–796, 2006.
- [107] S. Rüttinger, P. Kapusta, M. Patting, M. Wahl, and R. Macdonald. On the resolution capabilities and limits of fluorescence lifetime correlation spectroscopy (FLCS) measurements. *J Fluoresc*, pages 1–10, 2009.
- [108] L. Sanguigno, I. D. Santo, E. Causa, and P. A. Netti. A closed form for fluorescence correlation spectroscopy experiments in submicrometer structures. *Anal Chem*, 82(23):9663–9670, 2010.
- [109] J. Sankaran, X. Shi, L. Y. Ho, E. H. K. Stelzer, and T. Wohland. ImFCS: a software for imaging fcs data analysis and visualization. *Opt Express*, 18(25):25468–25481, 2010.
- [110] M. J. Saxton. Anomalous diffusion due to obstacles: a monte-carlo study. *Biophysj*, 66(2):394–401, 1994.
- [111] P. Schwille, J. Korch, and W. W. Webb. Fluorescence correlation spectroscopy with single-molecule sensitivity on cell and model membranes. *Cytometry*, 36(3):176–182, 1999.

- [112] C. E. Shannon. Communication in the presence of noise. *Proc IEEE*, 86(2):447–457, 1998.
- [113] A. Sharonov and R. M. Hochstrasser. Wide-field subdiffraction imaging by accumulated binding of diffusing probes. *P Natl Acad Sci Usa*, 103(50):18911–18916, 2006.
- [114] H. Shroff, C. G. Galbraith, J. A. Galbraith, and E. Betzig. Live-cell photoactivated localization microscopy of nanoscale adhesion dynamics. *Nat Meth*, 5(5):417–423, 2008.
- [115] G. Shtengel, J. A. Galbraith, C. G. Galbraith, J. Lippincott-Schwartz, J. M. Gillette, S. Manley, R. Sougrat, C. M. Waterman, P. Kanchanawong, M. W. Davidson, R. D. Fetter, and H. F. Hess. Interferometric fluorescent super-resolution microscopy resolves 3D cellular ultrastructure. *P Natl Acad Sci Usa*, 106(9):3125–3130, 2009.
- [116] P. J. Smith. A recursive formulation of the old problem of obtaining moments from cumulants and vice-versa. *Am Stat*, 49(2):217–218, 1995.
- [117] F. D. Stefani, K. Vasilev, N. L. Bocchio, F. Gaul, A. Pomozi, and M. Kreiter. Photonic mode density effects on single-molecule fluorescence blinking. *New J Phys*, 9(21), 2007.
- [118] C. Steinhauer, C. Forthmann, J. Vogelsang, and P. Tinnefeld. Superresolution microscopy on the basis of engineered dark states. *J Am Chem Soc*, 130(50):16840–16841, 2008.
- [119] M. A. Thompson, M. D. Lew, M. Badieirostami, and W. E. Moerner. Localizing and tracking single nanoscale emitters in three dimensions with high spatiotemporal resolution using a double-helix point spread function. *Nano Lett*, 10(1):211–218, 2010.
- [120] R. E. Thompson, D. R. Larson, and W. W. Webb. Precise nanometer localization analysis for individual fluorescent probes. *Biophysj*, 82(5):2775–2783, 2002.
- [121] E. C. Titchmarsh. The zeros of certain integral functions. *P Lond Math Soc*, 25:283–302, 1926.
- [122] D. Toomre and J. Bewersdorf. A new wave of cellular imaging. *Annu Rev Cell Dev Bi*, 26:285–314, 2010.
- [123] B. Valeur. Molecular fluorescence: principles and applications. Wiley-VCH, Weinheim, Germany, first edition, 2001.
- [124] S. van de Linde, I. Krstić, T. Prisner, S. Doose, M. Heilemann, and M. Sauer. Photoinduced formation of reversible dye radicals and their impact on super-resolution imaging. *Photochem Photobiol Sci*, 2011.
- [125] S. van de Linde, M. Sauer, and M. Heilemann. Subdiffraction-resolution fluorescence imaging of proteins in the mitochondrial inner membrane with photoswitchable fluorophores. *J Struct Biol*, 164(3):250–254, 2008.

Bibliography

- [126] S. van de Linde, S. Wolter, M. Heilemann, and M. Sauer. The effect of photoswitching kinetics and labeling densities on super-resolution fluorescence imaging. *J Biotechnol*, 149(4):260–266, 2010.
- [127] A. Vaziri, J. Tang, H. Shroff, and C. V. Shank. Multilayer three-dimensional super resolution imaging of thick biological samples. *P Natl Acad Sci Usa*, 105(51):20221–20226, 2008.
- [128] J. Vogelsang, T. Cordes, C. Forthmann, C. Steinhauer, and P. Tinnefeld. Controlling the fluorescence of ordinary oxazine dyes for single-molecule switching and superresolution microscopy. *P Natl Acad Sci Usa*, 106(20):8107–8112, 2009.
- [129] J. Vogelsang, R. Kasper, C. Steinhauer, B. Person, M. Heilemann, M. Sauer, and P. Tinnefeld. A reducing and oxidizing system minimizes photobleaching and blinking of fluorescent dyes. *Angew Chem Int Edit*, 47(29):5465–5469, 2008.
- [130] J. Vogelsang, C. Steinhauer, C. Forthmann, I. H. Stein, B. Person-Skegro, T. Cordes, and P. Tinnefeld. Make them blink: probes for super-resolution microscopy. *ChemPhysChem*, 11(12):2475–2490, 2010.
- [131] M. Wachsmuth, W. Waldeck, and J. Langowski. Anomalous diffusion of fluorescent probes inside living cell nuclei investigated by spatially-resolved fluorescence correlation spectroscopy. *J Mol Biol*, 298(4):677–689, 2000.
- [132] K. Weber, P. Rathke, and M. Osborne. Cytoplasmic microtubular images in glutaraldehyde-fixed tissue culture cells by electron microscopy and by immunofluorescence microscopy. *P Natl Acad Sci Usa*, 75(4):1820–1824, 1978.
- [133] J. Widengren, U. Mets, and R. Rigler. Fluorescence correlation spectroscopy of triplet-states in solution: a theoretical and experimental-study. *J Phys Chem*, 99(36):13368–13379, 1995.
- [134] J. Widengren and P. Schwille. Characterization of photoinduced isomerization and back-isomerization of the cyanine dye Cy5 by fluorescence correlation spectroscopy. *J Phys Chem A*, 104(27):6416–6428, 2000.
- [135] B. Wu and J. D. Muller. Time-integrated fluorescence cumulant analysis in fluorescence fluctuation spectroscopy. *Biophysj*, 89(4):2721–2735, 2005.
- [136] X. S. Xie and J. K. Trautman. Optical studies of single molecules at room temperature. *Annu Rev Phys Chem*, 49:441–480, 1998.
- [137] B. Zhang, J. Zerubia, and J.-C. Olivo-Marin. Gaussian approximations of fluorescence microscope point-spread function models. *Appl Optics*, 46(10):1819–1829, 2007.
- [138] M. Zhao, L. Jin, B. Chen, Y. Ding, H. Ma, and D. Y. Chen. Afterpulsing and its correction in fluorescence correlation spectroscopy experiments. *Appl Optics*, 42(19):4031–4036, 2003.

Claudio Dellagiacomma

MSc



Avenue du 24 Janvier 2 bis
1020 Renens
+41 21 693 77 73 (office)
+41 79 760 44 50

30. 1. 1982
single, no children
Switzerland (Uster)
claudio.dellagiacomma@a3.epfl.ch

Education

- 2007 – present **PhD in Photonics**, *Laboratoire d'Optique Biomédicale, EPFL Lausanne.*
(Graduation end of July 2011)
- 2005 – 2007 **Master of Science in Microengineering**, *EPFL Lausanne*, Specialisation in Optics.
(with Award)
- 2002 – 2005 **Bachelor of Science in Microengineering**, *EPFL Lausanne.*
- 1995 – 2002 *Kantonsschule, Alpenquai Luzern*, Typus C (natural sciences), Graduation: Matura.

Experience

- 2010 **Civil service**, Spectrometer Design, PMOD/WRC, *Davos.*
- 2004 – 2009 **Teaching Assistant**, different Tutorials, *EPFL Lausanne.*
- Winter 2006/07 **Internship** in Dept. Electrical & Computer Engineering,
Duke University, North Carolina, USA, Prof. David Smith
- Aug. 2003 **Internship**, Pilatus Aircraft Ltd., Metal Fabrication Workshop.
- Sep. 2001 **Internship**, Henauer & Gugler *in Lausanne*, Civil Engineering Firm.

Languages

- German native.
- French fluent, *studies in Lausanne.*
- English fluent, *exchange student in Wisconsin, USA (Summer 2000) and Duke University, (Winter 2006/07).*
- Italian intermediate, *three years of coursework in high school.*

Computer Skills

- OS Linux, Unix, Windows, Mac
- Programming Languages C/C++, Assembler, Java, PHP, HTML, Perl, MySQL
- Scientific Comsol, HFSS, Matlab, ProEngineer, L^AT_EX

Interests and Hobbies

- 2004 – 2006 **Flying Robot Contest:** Smartrob, *Autonomous Systems Lab, EPFL*.
- 2002 – 2003 **Robot Contest:** Prism, Robopoly, *EPFL*.
- 2004 – 2008 **Training Course Leader:** Boy Scouts, *Kriens*.
- 2003 – 2006 **Treasurer:** Boy Scouts, *Kriens*.
- 1999 – 2002 **Scout Leader:** J&S Leadership Training Program.
- Aug. 2001 Study week « **Swiss Youth Research** », electronics and informatics.
- Sports Hiking, cross-country skiing, ski-hiking, cycling, volleyball.
- Music Violin, Member of Orchestre Symphonique et Universitaire de Lausanne (OSUL).
- Misc Member of the Astronomical Society of Lucerne (AGL).

Peer Reviewed Publications

- Plasmonics
1. A. Degiron, C. Dellagiacomma, J. G. Mcilhargey, G. Shvets, O. J. F. Martin, and D. R. Smith, "Simulations of hybrid long-range plasmon modes with application to 90 degrees bends." *Optics Letters*, **32**(16), 2354 – 2356, 2007.
 2. A. Degiron, S.-Y. Cho, C. Harrison, N. M. Jokerst, C. Dellagiacomma, O. J. F. Martin, and D. R. Smith. "Experimental comparison between conventional and hybrid long-range surface plasmon waveguide bends." *Physical Review A*, **77**(2), 021804, 2008.
 3. C. Dellagiacomma, A. Degiron, J. J. Mock, D. R. Smith, T. Lasser, and O. J. F. Martin. "Simulation of complex plasmonic circuits including bends." (in press)
- Biomedical Optics
4. N.F.Y. Durand, C. Dellagiacomma, R. Goetschmann, A. Bertsch, I. Märki, T. Lasser, P. Renaud. "Direct Observation of Transitions between Surface-Dominated and Bulk Diffusion Regimes in Nanochannels." *Analytical Chemistry*, **81**, 5407 – 5412, 2009.
 5. C. Dellagiacomma, N. Bocchio, G. Lukinavicius, S. Geissbühler, I. Märki, S. Banala, K. Johnsson, T. Lasser. "Targeted photoswitchable probe for nanoscopy of biological structures." *ChemBiochem*, **11**, 1361 – 1363, 2010.
 6. S. Geissbuehler, C. Dellagiacomma, T. Lasser. "Comparison between SOFI and STORM." *Biomedical Optics Express*, **2**(3), 408 – 420, 2011.

Patents

1. S. Geissbuehler, C. Dellagiacomma, M Leutenegger, M. Geissbuehler, T. Lasser. "Cumulant Microscopy." *European patent pending* EP 11169880.9.

Conference Contributions:

1. C. Dellagiacomma, N.F.Y. Durand, R. Goetschmann, A. Bertsch, I. Märki, T. Lasser, P. Renaud. "Diffusion of Single Molecules in Nanochannels." *ECBO Munich*, 2009. (Poster)
2. S. Geissbuehler, C. Dellagiacomma, T. Lasser. "A comparative study of SOFI and STORM." *Picoquant, Berlin*, 2010. (Poster)